On-line dosimetry of very high energy electrons at low to ultra-high dose rates based on fluorescence spectroscopy

A thesis presented in the fulfilment of the requirements for the degree of Doctor of Philosophy in Physics.

Jason Mill

Physics Department

University of Strathclyde, Glasgow

February 2026

This thesis is the result of the author's original research. It has been composed by the author and has not been previously submitted for examination which has led to the award of a degree.

Abstract

External beam radiotherapy (EBRT) is a method of cancer treatment which applies external sources of ionising radiation in radiotherapy. At ultra-high dose rates ($\geq$ 40 Gy/s) it has been shown to effectively target cancerous tissue, while sparing healthy tissue. This sparing phenomenon is known as the FLASH effect, and is a rapidly evolving field of study. Ionisation chambers – the gold standard for clinical dosimetry – experience significant uncertainties at FLASH dose rates. Alternative dosimetry methods are available, but most cannot determine doses in real-time.

This thesis investigates a novel on-line chemical dosimeter that utilises the reduction of resazurin, in aqueous solution, into highly fluorescent resorufin. The dose is determined by fluorescence spectroscopy using common and inexpensive equipment. The dosimeter has been rigorously tested to establish a comprehensive preparation and handling procedure. Its response to X-ray, γ-ray and very high energy electron (VHEE) irradiation has also been investigated at the Scottish Centre for the Application of Plasma-based Accelerators (SCAPA) at the University of Strathclyde, the Commissariat à l'Énergie Atomique et aux Énergies Alternatives (CEA), and the CERN Linear Electron Accelerator for Research (CLEAR) facility, respectively. The results demonstrate the real-time capabilities of the dosimeter at clinically relevant doses for EBRT using γ-rays and VHEEs.

A parallel study has been conducted at CLEAR to investigate the therapeutic benefits of a focused VHEE beam, which concentrates dose in a small volume, thus reducing the entrance and exit doses. In addition, a non-invasive imaging modality was tested. It is based on the detection of 511 keV photons emitted when electrons and positrons annihilate, and shows that detection rate is proportional to dose. This technique also has the potential to be used as an oxygen-sensitive imaging modality,

which could improve the understanding of the FLASH effect in tissue. These studies present new and promising on-line dosimetry methods suitable for FLASH therapy, which widens the therapeutic window for cancer patients.

Acknowledgements

The work in this thesis would not be possible without the support of several people, who I would like to briefly thank. First and foremost, my supervisors. Prof. Dino Jaroszynski for giving me this opportunity and providing constant support throughout, as well as helping me become a well-rounded scientist. Dr. Gérard Baldacchino for his patience and guidance on all the chemistry-related challenges I faced during my PhD, and for giving me some valuable experience within his research group at the CEA.

Dr. Antoine Maitrallain, for his support throughout my project and his helpful suggestions that widened my perspective on a plethora of subjects.

Dr. Mark Wiggins, Dr. Enrico Brunetti and the rest of the SCAPA team for their support in the lab, helping me with numerous practical, technical, computational and logistical challenges.

Dr. David O'Donnell for both helping me with my own research project and letting me be part of his research project, from which I learned so much.

The CLEAR team at CERN: Pierre Korysko, Wilfrid Farabolini, Laurence Wroe, Vilde Rieker, Alfred Olof Petersson and Roberto Corsini, for allowing me to perform my experiments at CERN, which provided essential data, often going above and beyond expectations to deliver excellent quality VHEE beams, and being very helpful when things went awry.

My fellow PhD students Barış, Willow, and Kiruththika for involving me in their work, showing me the ropes, and helping me to grow as a researcher.

My salami lids Rachel, Babs and Tony, for always being there for me.

And finally, Mum, Dad, Drew and Hamish, for being the best family I could ask for.

Chapter 0. Acknowledgements

This research was funded by the France-UK DSTL PhD scheme. I am very grateful for the support given by this scheme and its members, as well as the engaging and hugely informative annual conferences.

List of Figures

List of Figures

List of Tables

Contents

Contents

Chapter 1

Introduction

1.1 Cancer treatment - a brief history

Cancer is a disease which has been known about for thousands of years, with the oldest known mention of it dating back to 3000 BC, in the Edwin Smith Papyrus [1]. It was during the time of the ancient Greeks that we get the etymological origin of the word "cancer" itself, which is attributed to Hippocrates, who lived from 460 – 370 BC and is widely regarded as the "Father of Medicine", with the Hippocratic Oath still taken by doctors today. The ancient Greeks made attempts to understand the nature of cancer more thoroughly, with Hippocrates developing the humoral theory of cancer [2]. It was believed that the body consisted of four elements, or humours: blood, phlegm, yellow bile, and black bile, and a healthy human body had a balanced amount of all four. It was noticed that in cases of breast cancer there was an excess of black bile, which was thought to be its cause. This understanding of cancer continued for many centuries, and resulted in the practise of treatments which today would be considered very unscientific. These included leeches, theriac (a concoction that was used for a range of medical conditions well into the 19^{th} century), crawfish boiled in the milk of an ass, and the following of unusual diets. The fact that these prescribed methods didn't help ease the suffering of cancer patients at the time, highlights the vital importance of a comprehensive understanding and a robust scientific model.

It wasn't until the development of the microscope in the mid-17^{th} century [4] that

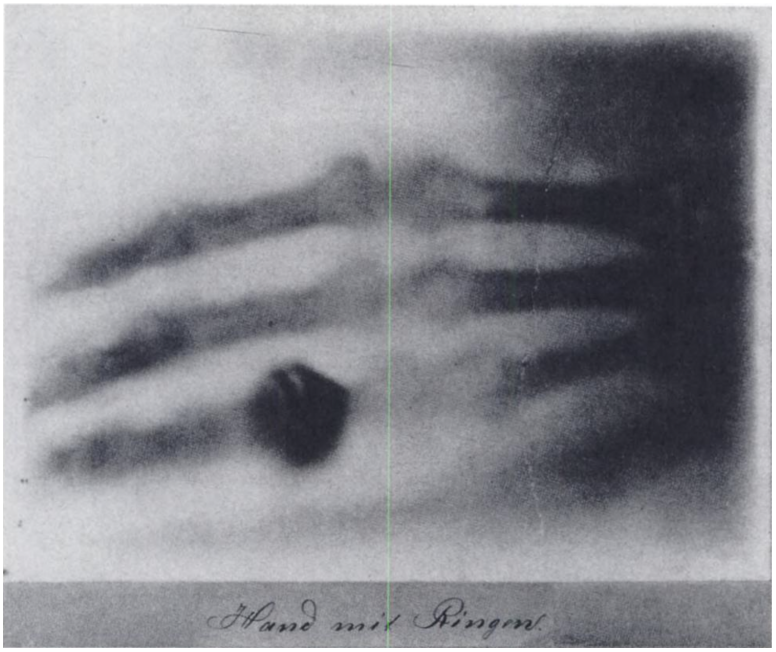

Figure 1.1: First X-ray image taken by Röntgen of his wife Anna Bertha Ludwig's hand wearing a ring [3].

a much better understanding of cancer on a cellular level was developed. Gradually, the medicines became more advanced, with the discovery of anaesthesia, antisepsis, and germ theory [5–7]. This allowed for cancer to be treated surgically with greater efficacy. However, it was the discovery of X-rays by Wilhelm Conrad Röntgen in 1895 [8] that opened the door to an entirely new method of cancer treatment: radiotherapy. It is said that less than three weeks after Röntgen's discovery (resulting in the now famous image shown in Figure 1.1), Emil Grubbe used X-rays to irradiate a female patient who had breast cancer. However, this claim is disputed. A few years later, in 1898, Pierre and Marie Curie discovered the radioactive element, radium [9], a source of ionising radiation suitable for radiotherapy. Within a short time, X-rays and radium were being used for the diagnosis and treatment of cancer. The dose delivered to a patient undergoing radiotherapy for the treatment of cancer is defined as the energy deposited per kilogram of tissue, and measured in gray (Gy), after Louis Harold Gray who defined the unit of absorbed dose. It was discovered in the 1920s that delivering doses of radiation over several days of treatment, resulted in less damage to healthy tissue [10], which is now known as fractionation. In 1928, the International Commission

on Radiological Protection (ICRP) was founded because of concerns in the medical community on the dangers of ionising radiation [11]. Over the course of the 20^{th} century many more scientific advances were made, including the invention of the nuclear reactor during Manhattan Project, and the introduction of medical linear accelerators in the 1950s [12]. At this time, proton therapy was investigated as a cancer treatment method [13], and electrons were used primarily to treat skin cancer because of their relatively low penetration depth [14]. Since then, a plethora of other particle beams have been investigated for radiotherapy purposes including neutrons, and helium, carbon, and neon ions.

1.2 Tissue response to ionising radiation

The damaging effects of ionising radiation on cells is typically separated into three stages:

- The physical stage: when atoms within tissue are excited, gaining discrete amounts of energy from the incident radiation, resulting in electrons moving to higher orbitals, or become ionised (losing or gaining electrons). This stage occurs in a time-frame of around $10^{-18} - 10^{-8}$ seconds, and is responsible for direct damage to DNA.

- The chemical stage: when energy is transferred from previously excited atoms to adjacent molecules, which results in the production of free radicals (molecules with unpaired electrons) and ejected electrons – sometimes referred to hydrated or aqueous electrons. This stage is responsible for indirect damage to DNA.

- The biological stage: when enzymatic repair mechanisms begin to repair damage from the physical and chemical stages. If the repair is not successful the cell dies within several weeks, or radiation-induced cancer appears (known as carcinogenesis) after a few years.

As radiation penetrates tissue, ionisation of atoms occur within the medium, as shown in Figure 1.2. The rate at which these events occur per unit distance is known

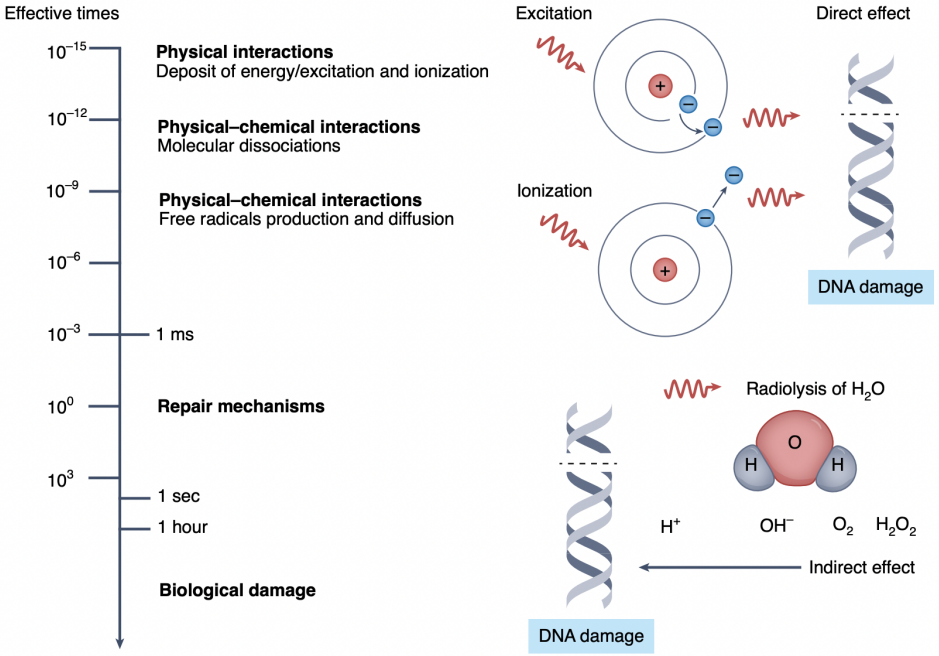

Figure 1.2: The mechanisms that occur in tissue after receiving doses of ionising radiation, and their approximate timescales [15].

as the linear energy transfer (LET). Low LET radiation such as X-rays, γ-rays and beta particles typically deposit a small amount of energy per unit distance travelled. Whereas particles such as protons, electrons, and alpha particles have both charge and mass, so deposit energy at a higher rate and thus have high LETs, which causes more biological effects than low LET radiation [16]. The main effect of particle interaction with tissue is, ultimately, damage to DNA strands. For low LET radiation, around 60% of DNA damage is caused by indirect effects – in other words, not by the incident radiation itself, but by the free radicals produced in the chemical stage [17].

DNA has a double-helical structure comprising two strands. A single-strand break (SSB) occurs when one of these breaks, which is the most common form of DNA damage. A double-strand break (DSB) occurs when both the strands are broken, which results in damage to the entire backbone of the DNA structure. DSBs are much more difficult for the body to repair, and can result in more severe biological damage.

The relative biological effectiveness (RBE) quantifies the effectiveness of a radiation modality. The term "relative" is used because it typically compares radiotherapy

modalities such as protons, ions and electrons with photon radiotherapy, and is given by the ratio of two doses,

$$RBE = \frac{D_{photon}}{D_{particle}}, \tag{1.1}$$

where D_{photon} is the dose from photon irradiation required for a specific biological effect, and $D_{particle}$ is the dose from a particle (proton, ion or electron) beam required for the same biological effect to occur [18]. A commonly used modality for D_{photon} is 250 $\mathrm{kV_p}$ X-rays, because it is widely used in radiobiological studies.

Figure 1.3 shows the relationship between RBE and LET for a range of biological effects, such as the aforementioned SSBs and DSBs, and also prematurely condensed chromosomes (PCC breaks), chromosomal aberrations, and cell death, or apoptosis [19]. Typically, cells undergo condensation – clumping together to form longer, more organised structures – during the mitosis phase of the cell cycle, but when the cell condenses outwith mitotic events, this is known as a prematurely condensed chromosome [20]. Chromosomal aberrations are numerical or structural disorders in a chromosome, and there is a positive correlation between the frequencies of these and the onset of cancer [21]. For low LET values, the density of ionisation events is low, with the distance between two events almost always greater than the minimum distance required for two chromosome breaks to interact and recombine ($\sim 0.2-0.5$ μm). Broken ends can either recombine with the same original chromosome, or with a different chromosome – this can result in structural defects. The RBE peaks for all biological effects when the optimal distance between ionisation events most efficiently produces chromosome break pairs. As the LET increases further, the RBE decreases, because the energy necessary for the given biological effect is exceeded, therefore the excess energy is wasted and the efficiency per unit dose decreases.

The effect of LET on RBE shown here highlights the complexity of biological systems and its sensitivity to delivered radiotherapy. It is over-simplistic to only consider dose delivered when comparing different beam modalities, particularly charged particles and photons.

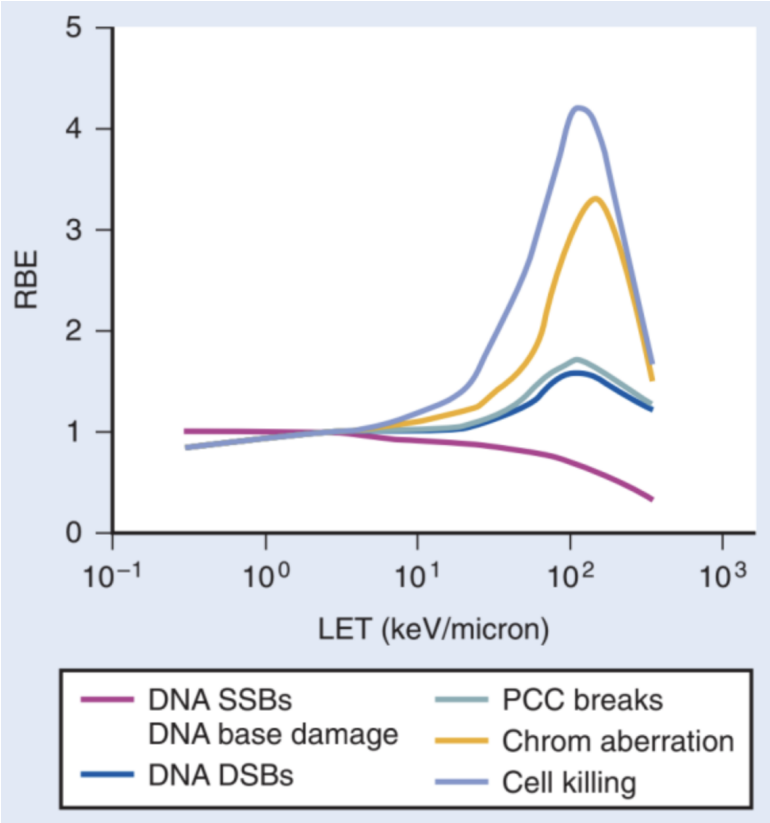

Figure 1.3: The effect of LET on RBE for single-strand breaks (SSBs), double-strand breaks (DSBs), prematurely condensed chromosomes (PCC breaks), chromosomal aberrations (chrom aberration), and cell killing [19].

1.3 Current state of radiotherapy

Radiotherapy is currently used for treating around half of all cancer patients [22]. X-ray photons are the most common type of radiation used. The biggest challenge of radiotherapy is to target and kill cancerous tissue, while protecting healthy tissue. Surrounding healthy tissue receiving a substantial dose of radiation can cause long-term damage to healthy cells. This is because radiation usually passes through healthy tissue and deposits energy as it propagates. Moreover, the incident radiation often travels beyond the tumour and delivers an exit dose to healthy tissue. Therefore, for tumours located deep within the body, or in close proximity to sensitive organs, such as the brain and spine, conventional radiotherapy can pose a significant risk of causing secondary cancers and damaging healthy organs. One method of sparing surrounding

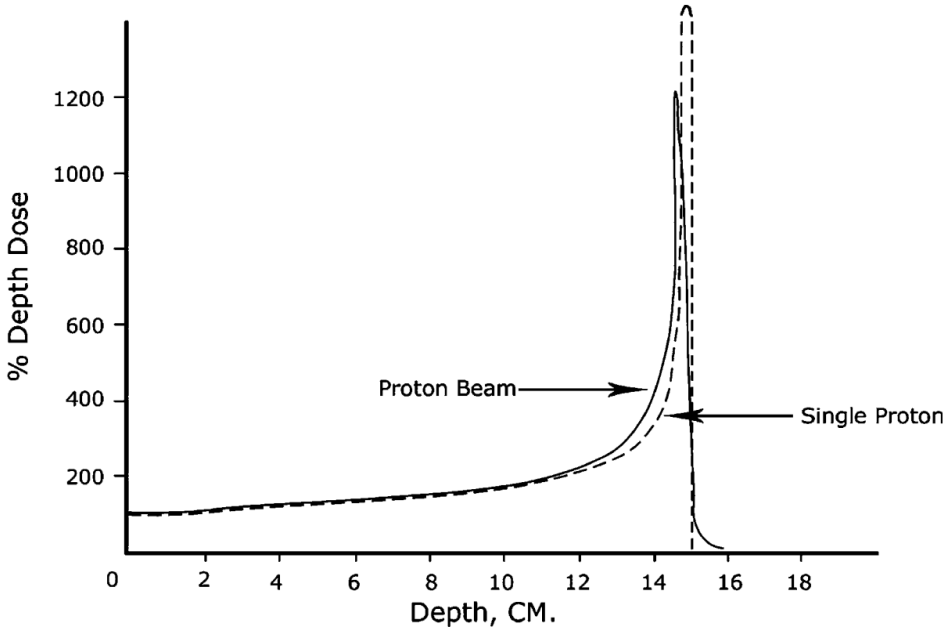

Figure 1.4: The normalised dose depth curve of a mono-energetic 140 MeV proton beam compared with a single proton in tissue. The characteristic Bragg peak ensures that lower dose is deposited in tissue surrounding the target, reducing its toxicity, which is a very useful property of proton beam radiotherapy [23].

healthy tissue is to use proton beam therapy (PBT). The high proton mass results in a high linear-energy-transfer (LET), which produces an exponentially increasing dose along the particle trajectory for some distance (dependent on the proton energy), before dropping dramatically in a very short distance. This results in a low entrance dose, while the majority of the particle energy is deposited in a characteristic Bragg peak deep into the target as shown in Figure 1.4. Despite these advantages PBT is not always an appropriate modality, and depends on the type of cancer. PBT also requires very large and expensive accelerators and gantries to deliver the radiation. It is the ultimate goal of radiotherapy to optimise radiation delivery while ensuring that maximum dose is delivered to the tumour, whilst minimising the harmful impact of the radiation on healthy tissue.

1.4 FLASH

Although the concept of using high dose rates was proposed as early as the 1970s [24–26], it didn't gain noticeable traction until very recently. In 2014, Favaudon et. al [27] demonstrated that by delivering the same total dose as conventional techniques (in this case 15 – 17 Gy) at ultra-high dose rates ($\geq$ 40 Gy/s), damage to healthy tissue can be reduced, whilst maintaining a similar tumour response. The technique is associated with this tissue-sparing effect. It is now commonly called the "FLASH effect", which has been demonstrated in numerous studies in recent years involving mice [28–30], cats and pigs [31], zebrafish [32], and even the first human patient [33]. The reduction in normal tissue toxicity implies that larger overall doses can be delivered, thus enabling better tumour control.

While much of the underlying biological mechanisms causing this phenomenon are generally not well understood, a 2019 study suggested that oxygen concentration in the tissue may have a significant role [32]. This study used mice to test the hypothesis that FLASH results in a reduced yield of reactive oxygen species (ROS). The oxygen concentration in the brains of the mice was increased by carbogen breathing before and after the delivery of a 10 Gy dose of whole brain irradiation. They were then given a range of cognitive function tasks, such as object recognition and it was found that the control group showed no change in discrimination index (DI), indicating that their performance on the cognitive tasks did not differ between the non-irradiated condition and conventional (CONV) radiotherapy. In this particular study, the mean FLASH dose rates were above 100 Gy/s and the CONV dose rates were $0.07 - 0.1$ Gy/s. However, the group receiving FLASH irradiation showed a significant drop in DI, which indicated that increasing the oxygen concentration reverses the positive FLASH effect. After one month, the mice were given object recognition tests and it was found that the FLASH group's results were statistically indistinguishable from the control group, whereas the CONV group experienced a reduction in cognitive function (see Figure 1.5).

In addition to oxygen depletion, another potential mechanism of the observed FLASH effect has been suggested and experimentally tested using ultra-high dose rates

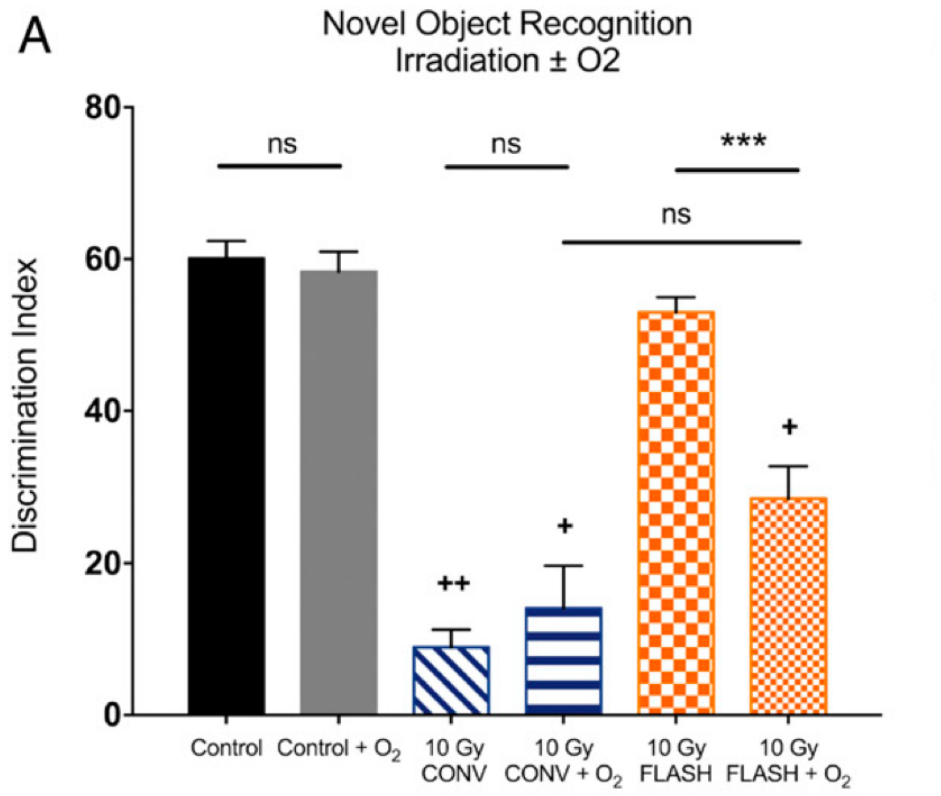

Figure 1.5: Findings from Montay-Gruel et, al [32] showing the beneficial effect of whole brain irradiation of mice at FLASH dose rates. Mice irradiated with FLASH were more able to recognise objects than mice irradiated at conventional dose rates, and the increased concentration of oxygen diminished the beneficial FLASH effect.

on circulating immune cells in the bloodstream [34]. Their hypothesis is that large doses delivered in a fraction of the time compared to conventional radiotherapy reduces the number of cells present in the irradiation volume during delivery, leading to a smaller number of cells being killed. Studies show that tumour control is influenced by the immune system [35–37], as is healthy tissue toxicity [38–40]. Therefore, if FLASH increases the survival rate of immune cells, similar tissue sparing effects to those seen in animal studies could result. A key finding was that at total doses of $\geq$ 30 Gy, conventional radiotherapy kills nearly 100% of circulating immune cells, whereas this decreases dramatically to nearly 5% for ultra-high FLASH dose rates. An important limitation of the study is that immune cells are present throughout the body, not just in the bloodstream, and these have not yet been investigated. The sparing effect may

be substantially greater in the blood than in the entire immune system, which implies that more work is required to verifying these findings.

1.5 The need for new dosimetry methods

The International Committee on Radiation Units and Measurements (ICRU) requires a dose accuracy with an error margin of no more than 7% [41]. While FLASH radiotherapy is a very promising concept for improving the efficacy of treatment, the delivery of doses at high dose rates are difficult to accurately monitor using existing dosimeters. The following section gives an overview of widely used dosimeters for doses applied at conventional dose rates. We also consider areas that should be improved to ensure FLASH-compatibility.

1.5.1 Ionisation chambers

Ionisation chambers, or ion chambers, are the most ubiquitous dosimeters used in clinics, and are considered the "gold standard" dosimetry method for radiotherapy [42]. Ion chambers detect ionising radiation using two charged plates that apply an electric field across a medium. A change in voltage caused by the incident radiation is measured. At ultra-high dose rates (UHDRs), ions are produced with an increased density leading to additional recombination in their tracks, which requires large correction factors [43–45]. As an example, the Advanced Markus chamber has a small volume and relatively high dose-per-pulse tolerance, compared with other models, which makes it suitable for UHDR studies [46].

Despite the large correction factors required, ion chambers continue to be used in many FLASH studies. However, currently no universally accepted model for this regime exists, and empirical models are generally used, but studies have been carried out on methods of reducing recombination effects at UHDRs. One study substantially improved the ion collection efficiency by reducing the distance between the electrodes, but this resulted in new sources of error. For example, day-to-day use of the modified chamber can introduce small fluctuations in its geometry, drastically affecting its

response to radiation [46].

Other studies have been undertaken, which include a conceptual design of a gas chamber that accurately measures doses up to 40 Gy in a few microseconds [47]. Prototypes of this design are being tested but several engineering challenges still remain. Namely, successfully withstanding the high pressures present in the chamber, and the high precision required in sealing the chamber and setting the pressure.

1.5.2 Radiochromic film

A widely-used, tissue equivalent dosimeter is radiochromic film (RCF). It provides high resolution dose distributions in two dimensions and is easy to use, making it accessible to a wide range of users. However, it cannot be used to measure dose in real time, and requires a post-irradiation wait time of 12-24 hours [42, 48, 49]. More information on how RCF works can be found in Chapter 3.3. RCF has been demonstrated to be independent of dose rate over a wide range of doses, but with uncertainties of about 5% for electrons at FLASH dose rates [50]. At conventional dose rates, protons and other high-LET radiation can cause an under-response in the film. Further studies are required to understand the effect of high-LET radiation at FLASH dose rates [51, 52].

1.5.3 Alanine

A chemical-based dosimeter, alanine undergoes internal changes on irradiation resulting in formation of stable radicals. Electron paramagnetic resonance is used to determine the concentrations of these radicals. Alanine can withstand extremely high doses, up to 100 kGy for photons and electrons [53]. It has been shown to be dose rate independent for FLASH dose rates, but only when the total dose delivered is below 5 kGy. Additionally, the signal-to-noise ratio decreases for low doses. Despite its apparent suitability for investigating FLASH, alanine requires highly specialised readout equipment, which is a time-consuming process. Additionally, due to the small size and shape of the alanine pellets, the user is unable to determine information on the radiation beam profile.

1.5.4 Calorimeters

Perhaps the most fundamental method of determining dose is calorimetry, which directly measures the increase in temperature of irradiated material, typically water or graphite [42]. If the mass and specific heat capacity of the material is known, it is possible to determine the energy deposited:

$$\Delta E = mC\Delta T, \tag{1.2}$$

where ΔE is the energy deposited, m and C are the mass and specific heat capacity of the material, respectively, and ΔT is the increase in temperature.

While it is a theoretically simple dosimetry method, in practice it is more complicated. The above equation is only valid under the assumption that all energy deposited is converted directly to heat. In reality, heat can be produced indirectly, known as heat defect [54]. Endothermic and exothermic processes can occur in the material, which increase and decrease the heat defect, respectively. This is caused by impurities; the uncertainties introduced by these chemical processes limit the versatility of water calorimeters. Therefore, graphite calorimeters are more commonly used. They give smaller measurement uncertainties for large increases in temperature per unit absorbed energy. However, they require correction factors to determine the delivered dose to water. Additionally, the temperature rise for 1 Gy of dose is extremely small – less than 1 mK for water. This requires very precise instruments to accurately measure temperatures with a resolution of μK, which is challenging at room temperature.

Nevertheless, the temperature increase measured by calorimeters is independent of the dose rate, making them a promising candidate for FLASH studies. However they require careful temperature control, and more studies are required to confirm their suitability as a dosimetry standard in the clinic [44].

A more comprehensive list of potential FLASH dosimeters can be found in [55], but it is clear there is a demand for FLASH-compatible dosimeters that are suitable for use

in clinics.

Several novel dosimetry methods have recently been proposed, including plastic scintillation detectors [56], which have linear responses to doses up to 32 kGy; radiation-induced acoustic imaging (RAI) [57], which may allow for 4D in-vivo dosimetry of FLASH in real time, up to 5 Gy; and diamond-based dosimeters, the physical properties of which can be modified to be FLASH compatible. They are favourable due to their near-tissue equivalence, high spatial resolution and ability to withstand large amounts of radiation [58].

1.6 Thesis objective

The aim of this PhD project is to determine whether or not resazurin is suitable for ultra-high dose rate dosimetry. It is a low-cost, non-toxic chemical, the fluorescence spectrum of which can be read out in real-time using standard instruments. We tested the dosimeter using several irradiation sources, and made advances towards optimising the preparation, handling and read-out methods, to demonstrate its feasibility as a dosimetry method for future FLASH studies.

Chapter 2

Background & Theory

2.1 Particle acceleration

As modern physics has progressed, interest has been increasingly drawn towards the very large, such as the universe, and the very small, such as fundamental particles constituting matter. Progress in probing these two areas is resulting in breakthroughs at both extremes [59, 60]. Particle accelerators are extremely useful for probing the very minute. Probe resolutions are required that are much smaller than the size of the object. Visible light probes, for example, have wavelengths ranging from $400 - 700$ nm, which isn't useful if we wish to investigate atomic structures on the scale of 10^{-10} m, or atomic nuclei, which are $\approx 10^{-15}$ m. Producing electromagnetic radiation – or particle probes – with much smaller wavelengths is challenging. One method of producing suitable ultra-short wavelength radiation is using bremsstrahlung, where a relativistic charged particle, such as an electron, is deflected by the fields of atomic nuclei causing deceleration that results in the emission of highly energetic photons with wavelengths sufficiently short for probing materials on an atomic scale. Probing dense materials is also possible using particles with a small de Broglie wavelength, $\lambda = h/p$, where h is Planck's constant and p is the particle momentum. From Planck [61], we have $E = hc/\lambda$, which shows that the energy, E, of a photon is inversely proportional to its wavelength, with c being the speed of light in a vacuum. Achieving such short wavelengths usually requires very high energy electrons that are typically accelerated

by strong electric fields. From Einstein's mass-energy equivalence, $E = mc^2$ [62], the energy required to produce a particle is directly proportional to its mass, m. Therefore, to study exotic, massive particles produced in collisions, a large amount of energy is required. Modern particle accelerators are capable of meeting these requirements.

Particle accelerators have played a fundamental role since the early 20th century in enabling the steady progression of modern physics. They have been constantly developed to meet the demand for increasingly energetic particles. One of the first particle accelerators was the Van de Graaff generator, first built in 1936, which can achieve energies of several MeV [63]. Since then, various types of particle accelerators, including linear accelerators (linacs), have been developed to produce high energy particles. They have provided physicists with valuable information on quarks, the fundamental particles that make up protons and neutrons [64]. However, one important use of them is in medical applications, such as producing X-ray, electron and proton beams for cancer treatment [65–67]. These accelerators use microwave or radio-frequency (RF) fields to create large potential differences in resonant cavities, which propel charged particles. The RF fields ensure that the particles are supplied continuous energy as they travel down a series of cavities, or waveguides, with a slow wave structure, leading to acceleration.

Most radiotherapy applications utilise accelerated electrons that are either directed to a tumour in a patient, for electron beam therapy, or onto a target such as tungsten, to produce X-ray and gamma photons by bremsstrahlung. For linear accelerators, the particle energy is proportional to the length of the accelerator. However, conventional RF accelerators are fundamentally limited to an electric field gradient less than 100 MV/m due to ionisation and breakdown of the accelerating cavity walls. Alternative accelerating media have been investigated, one of which is the wakefield accelerator, which utilises the ultra-high fields of charge separation in plasma that can greatly exceed 100s MV/m.

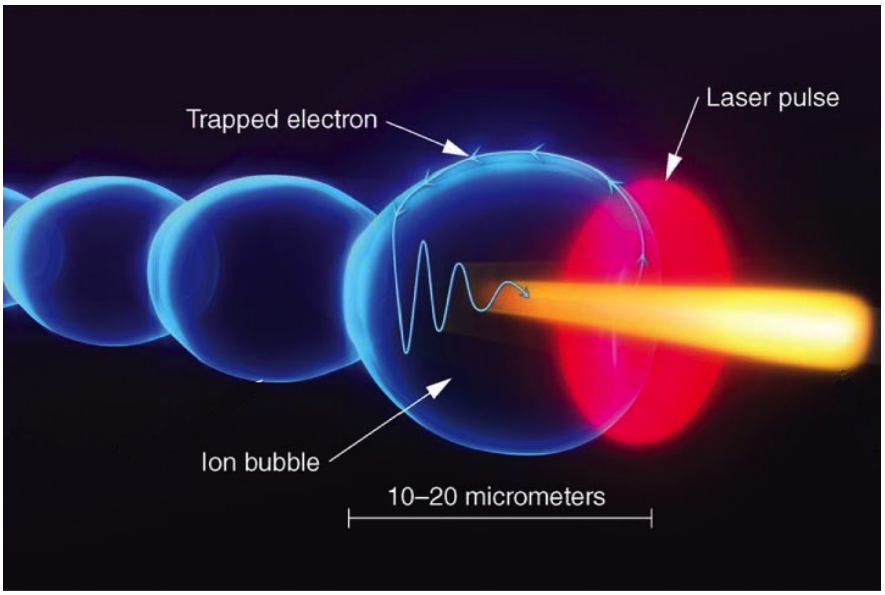

Figure 2.1: Visualisation of the laser wakefield acceleration mechanism. An intense short duration laser pulse transfers momentum to plasma electrons causing them to oscillate locally at the plasma frequency. Ions are relatively immobile because of their large mass and do not move significantly on the electron motion time scale. A small fraction of these displaced electrons can be trapped in the ion bubble, where they are accelerated along the laser axis close to the speed of light [68].

2.2 Laser wakefield accelerators

In 1979, Tajima & Dawson published their seminal paper [69] that proposed an electron accelerator capable of producing electric fields at least 100 times greater, and power densities 10^5 times greater than technologies of the time. They showed theoretically that a short duration laser pulse incident on under-dense plasma – where the oscillation frequency of the plasma is less than that of the laser field – causes an electrostatic wake in the plasma due to charge separation, similar to a wake behind a boat. Momentum from the incident laser field is transferred to plasma electrons by the ponderomotive force, which results in electrons being pushed out of the laser pulse path (see Figure 2.1). Plasma ions remain quasi-stationary due to their much greater mass than electrons. As the laser pulse propagates, electrons are pulled back towards the positively charged quasi-stationary ions, which causes them to oscillate at the plasma frequency. The combination of electrons oscillating at the plasma frequency and the perturbation occurring at a velocity close to that of light creates a plasma density wave, with an associated "relativistic" wakefield arising from the density perturbations. The electric

fields generated by these plasma waves are strong for a sufficiently powerful laser, which enables background electrons to be trapped behind the laser pulse and accelerate in the direction of laser propagation. This type of accelerator has come to be known as the laser wakefield accelerator (LWFA). In cold, non-relativistic plasma the highest electric field plasma can sustain is given by the wave-breaking amplitude limit [70],

$$E_0[\mathrm{v/m}] = cm_e\omega_p/e = 96\sqrt{n_e[\mathrm{cm}^{-3}]}, \tag{2.1}$$

where m_e is the mass of an electron, e is its charge, n_e is the electron number density and ω_p is the electron plasma frequency:

$$\omega_p = \sqrt{\frac{n_e e^2}{\varepsilon_0 m_e}}, \tag{2.2}$$

where $\varepsilon_0 = 8.85 \times 10^{-12}$ Fm^{-1} is the vacuum permittivity in farads per metre [71]. Plasma with electron density $n_e = 10^{18}$ cm^{-3} can produce a field $E_0 = 96$ GV/m, which is more than three orders of magnitude greater than that in an RF linear accelerator.

The wakefield is driven most effectively when the duration of the laser pulse, τ, is approximately equal to the plasma wavelength, $\lambda_p = 2\pi c/\omega_p$. For densities usually used in LWFAs, this corresponds to an extremely short laser pulse duration, $\tau \lesssim 100$ fs. At the time of Tajima & Dawson's work [69], the technology necessary to deliver such a short intense laser pulse did not exist. It wasn't until decades later that significant advances were made in developing compact terawatt lasers [72–75], to experimentally realise the LWFA [76–78]. For several years, electron bunches produced in these experiments had energy spreads of $\Delta E/E = 100\%$, which are not useful for applications requiring mono-energetic electron bunches such as those in medicine or material science. It wasn't until a decade later that several research groups demonstrated acceleration of electron bunches with low divergence and small energy spread ($< 3\%$) [79–81]. Some of these results [79] were achieved as part of the ALPHA-X project led by Strathclyde. They were achieved by varying the plasma density while keeping the laser parameters constant. Plasma was created by ionising helium atoms in a supersonic gas-jet and the electron density was varied by changing the backing pressure of the gas-jet noz-

zle. It was found that when the plasma density was low, no energetic electrons were observed, whereas when the density was increased, electrons with energies up to 100 MeV were produced. However, for higher plasma densities lower energies were produced with a larger energy spread. When the laser pulse length exceeds the relativistic plasma wavelength a Maxwellian energy distribution was observed. This was the first time it was shown that with very carefully selected parameters – namely the pulse length, laser spot size, plasma electron density and interaction length – one can obtain a quasi-monoenergetic energy spectrum, which was a significant step in the further understanding and development of LWFAs.

Since 2004 the capabilities of LWFAs have steadily improved simultaneously with advances in table-top laser technology, with electron energies regularly exceeding 1 GeV [82–88]. In the next section an overview of the underlying theory behind these types of particle accelerators is provided.

2.3 Plasma theory

2.3.1 Plasma

Plasma is often referred to as the "fourth state of matter". It comprises a gas of free electrons and ions where their dynamics are mainly governed by long-range electromagnetic forces, rather than nearest-neighbour interactions as for solids, liquids and gases. An ideal plasma has the same number of electrons as ions, making it a quasi-neutral medium.

The characteristic distance beyond which net charge neutrality of plasma can be assumed is known as the Debye shielding length

$$\lambda_D = \sqrt{\frac{\varepsilon_0 k_B T_e}{n_e e^2}}, \tag{2.3}$$

where ε_0 is the vacuum permittivity, k_B is Boltzmann's constant, T_e the electron temperature, n_e the electron number density [m^{-3}] and e the electron charge. In other words, if a test charge particle were to be placed in plasma, the Debye length is the distance over which its electric field has an effect. Beyond this length the plasma re-

mains neutral. For plasma collective effects to dominate, its volume should be greater than the Debye sphere (of radius λ_D), and many particles should be present within this sphere [89]. When an electron is displaced by a very small distance, ($<< \lambda_D$), it experiences a restoring Coulomb force from the stationary ions, which pulls it back to its initial position, gaining kinetic energy in the process. This additional energy results in harmonic or anharmonic motion of the electrons, which in turn leads to oscillations in the number density. The frequency at which the electrons oscillate harmonically is the plasma frequency, given by Equation 2.2. From this, one can also derive the plasma wavelength, $\lambda_p = 2\pi c/\omega_p$. This can also be applied to the background ions, but since they are much more massive than the electrons, they oscillate at a much lower frequency and are considered stationary on the timescale of a plasma oscillation period.

An important equation for determining the propagation of transverse electromagnetic waves in un-magnetised plasma is the dispersion relation, which is given by

$$\omega^2 = \omega_p^2 + c^2k^2, \tag{2.4}$$

where ω is the angular frequency of the incident electromagnetic wave, and k is its wave number. This relation has significant implications for the propagation of EM waves through plasma. The refractive index, μ, of a plasma is given by

$$\mu = \frac{ck}{\omega},$$

$$\implies \mu = \sqrt{1 - \frac{\omega_p}{\omega}}. \tag{2.5}$$

Therefore, if the frequency of incident electromagnetic wave is less than the plasma frequency ($\omega < \omega_p$), the refractive index of plasma is imaginary and the radiation cannot propagate. Whereas, for frequencies greater than that of the plasma ($\omega > \omega_p$), the refractive index is real, propagation occurs, and the plasma is referred to as "underdense". If the incident electromagnetic wave has a frequency equal to that of the plasma ($\omega = \omega_p$), which corresponds to the critical density of the plasma. Substituting

ω_p for ω in Equation 2.2 yields

$$n_c = \frac{\varepsilon_0 \omega^2 m_e}{e^2}, \tag{2.6}$$

where n_c is the critical density of the plasma. Therefore, for a laser wavelength $\lambda_0 = 800$ nm [90], the critical density of plasma will be $n_c \approx 1.75 \times 10^{21}$ cm^{-3}. Plasma used in laser wakefield accelerators typically have densities in the range 10^{17} – 10^{19} cm^{-3} [91], therefore in all cases considered the plasma is underdense.

2.3.2 Laser-plasma interactions

How the incident laser pulse interacts with the plasma as it propagates is important in plasma-based accelerators. The theory presented in this section is based on Esaray et al. [92].

A laser pulse propagating through a medium can be described in terms of its electric field (**E**) component and its magnetic field (**B**) component. When considering laser-plasma interactions these components are usually derived from the vector potential **A** and scalar potential ϕ,

$$\mathbf{E} = -\frac{\partial \mathbf{A}}{\partial t} - \nabla\phi, \tag{2.7}$$

$$\mathbf{B} = \nabla \times \mathbf{A}, \tag{2.8}$$

and the normalised vector potential is defined as

$$\mathbf{a} = \frac{e\mathbf{A}}{m_e c^2}. \tag{2.9}$$

The laser strength parameter, a_0, is defined as the peak amplitude of the normalised vector potential,

$$a_0 = \frac{eE_0}{m_e c \omega}, \tag{2.10}$$

where E_0 is the peak amplitude of the electric field component of the laser field. The laser strength parameter is related to the peak laser intensity, I_0, by the relation

$$a_0 = 8.5 \times 10^{-10} \lambda[\mu\text{m}](I_0[\text{W/cm}^2])^{1/2}, \tag{2.11}$$

where it is assumed the laser beam is linearly polarised and has a Gaussian profile. The value a_0 defines a boundary between the linear and non-linear (relativistic) regimes of electron oscillatory, or "quiver", motion within the plasma. If $a_0 < 1$, the electrons are considered to be weakly relativistic, and if $a_0 \geq 1$ the electrons have relativistic quiver motion and the interactions with the plasma are non-linear.

Physically, $a = p/m_e c$ is the transverse momentum, p, of the electrons in the plasma normalised to $m_e c$. The Lorentz factor is defined as

$$\gamma = \frac{1}{\sqrt{1 - \frac{v^2}{c^2}}} = \sqrt{1 + \frac{p^2}{m_e^2 c^2}}, \tag{2.12}$$

and using the value of a is

$$\gamma = \sqrt{1 + a^2}. \tag{2.13}$$

This equation is also valid for weakly relativistic electrons, where $\gamma \approx 1$.

2.3.3 Ponderomotive force

As a laser pulse propagates through plasma, electrons are displaced from regions of high field intensity by the ponderomotive force [89, 92]

$$\mathbf{F}_p = \frac{-e^2}{4m_e\omega^2}\nabla\mathbf{E}^2 = -m_e c\nabla\left(\frac{a^2}{2}\right). \tag{2.14}$$

This is for the electric component of the laser field $\mathbf{E}(\mathbf{r}, t) = \mathbf{E}(\mathbf{r})\cos wt$, while the $\mathbf{v} \times \mathbf{B}$ component of the Lorentz force is neglected (i.e. the electron quiver momentum is the dominant motion). From this equation the ponderomotive force doesn't depend on the charge of the particle in the laser field, however it is inversely proportional to particle mass. This is why electrons are displaced whereas more massive ions remain quasi-stationary. The equation shows that the ponderomotive force is proportional to λ^2, which implies that it becomes much more significant when the wavelength of the incident laser pulse is increased.

2.3.4 Plasma wave dynamics

As outlined in Section 2.2, when an intense, short-duration laser pulse propagates through plasma, the ponderomotive force (see Equation 2.14) displaces plasma electrons from their initial positions, while positive ions remain quasi-stationary. This charge separation produces a space-charge field that results in a restoring Coulomb force which pulls displaced electrons back towards the positively charged ions, where they overshoot, resulting in harmonic or anharmonic motion and density modulations in the plasma. The charge separation results in an extremely high electric field that can be strong enough (depending on the laser intensity and the electron density, n_e) to trap electrons behind the laser pulse, and accelerate them to MeV-range energies in mm-scale distances. The trapped electrons are either background electrons from within the plasma, or can be externally injected using a linear accelerator – however this is very uncommon. Electrons gain energy from this structure analogous to a surfer gaining momentum from a large wave, or a wake behind a boat. The surfer gains momentum from the wave using the force of gravity as its source of energy. Electrons travel faster than the laser pulse group velocity and gain momentum and energy from the plasma wake, achieving a maximum energy gain at the trough of the wave, beyond which it enters a decelerating region of the wave.

The behaviour of the induced plasma waves is determined by the laser strength parameter, a_0. If $a_0 << 1$ the waves will exhibit linear excitation, and the resulting electric field will not be sufficient to trap background electrons; they must therefore be injected via other methods, such as using additional laser pulses [81, 93, 94], ionisation injection [95–97], and applying an external magnetic field [98–100]. If $a_0 \geq 1$ then the electron motion is relativistic and the resulting wakefield will be anharmonic, and self-injection will occur by wave-breaking. This regime is also sometimes known as the bubble regime.

Linear regime

In uniform and collision-less plasma, electrons are displaced from their equilibrium point, while ions remain quasi-stationary. Charge separation causes a space-charge

Coulomb restoring force, which causes electrons to oscillate around their equilibrium point at a frequency $\omega_p = \sqrt{n_e e^2/\varepsilon_0 m_e}$. This results in a change in density, which can be described via the relation [101],

$$\delta n = \delta n_e \sin(k_p z - \omega_p t), \tag{2.15}$$

where k_p is the wave number of the relativistic plasma wave. This density change leads to a perturbation in the electric field described by the Poisson equation, $\nabla \delta \mathbf{E} = -\delta n e/\varepsilon_0$. Integrating Equation 2.15 with respect to z, one obtains the expression,

$$\delta \mathbf{E}(z,t) = \frac{\delta n_e e}{\varepsilon_0 k_p} \cos(k_p z - \omega_p t)\mathbf{e}_z. \tag{2.16}$$

The phase velocity, v_p of the plasma wave is slightly higher than the speed of light, therefore we can use the approximation, $v_p = \omega_p/k_p \simeq c$. Using this, with the expressions $n_e = \varepsilon_0 \omega_p^2 m_e/e^2$ and $E_0 = m_e c \omega_p/e$, the electric field perturbation can be described by

$$\delta \mathbf{E}(z,t) = E_0 \frac{\delta n_e}{n_e} \cos(k_p z - \omega_p t)\mathbf{e}_z. \tag{2.17}$$

Note the similarities of this relation and the equation for density perturbation (2.15). The only differences are a change in amplitude by a factor of E_0/n_e, and a change in phase of the electric field by $-\pi/2$ (or, in terms of the plasma wavelength, -$\lambda_p/4$). The amplitude of the plasma wave is greatest when the laser pulse length is comparable to the plasma wavelength, i.e. $c\tau \simeq \lambda_p$ [102]. The electric field component in Equation 2.17 is in the direction of laser propagation, but transverse field components, E_r and B_θ exist, which need to be considered. When $a^2 << 1$, $E_r \sim E_z \sim a^2$ and $B_\theta \sim a^4$ [92]. In this regime, there is a region of the wakefield with length $\lambda_p/4$ where a relativistic electron experiences a longitudinal acceleration simultaneously with a radial focusing force [103].

Nonlinear and Bubble regime

When the laser strength parameter, $a \geq 1$, the plasma wake becomes nonlinear as electrons undergo relativistic motion. This causes the wavefronts to become curved as the density wave becomes anharmonic. Regions of extremely high electron density are created, increasing the electric field gradient beyond the value of E_0, and giving the longitudinal electric field profile a "sawtooth" shape. Additionally, in the nonlinear regime, the amplitude and period of the wave increase. The wavelength of a nonlinear plasma wave is then given by

$$\lambda_{Np} = \begin{cases} \lambda_p[1 + 3(E_{max}/E_0)^2]/16, & E_{max}/E_0 \ll 1 \\ \lambda_p(2/\pi)(E_{max}/E_0 + E_0/E_{max}) & E_{max}/E_0 \gg 1 \end{cases}, \tag{2.18}$$

where E_{max} is the peak electric field amplitude of the plasma wave. Furthermore, it can be shown using nonlinear, one-dimensional cold fluid equations [104] that the maximum amplitude of a plasma wave in this regime is

$$E_{WB} = \sqrt{2(\gamma_p - 1)}E_0, \tag{2.19}$$

where $\gamma_p = \sqrt{1 - v_p^2/c^2}$ is the Lorentz factor associated with the plasma wave phase velocity, which is approximately equal to the group velocity of the laser. Therefore, it can be approximated as

$$\gamma_p \simeq \frac{\omega}{\omega_p}, \tag{2.20}$$

in the low intensity one-dimensional limit.

2.3.5 Electron trapping and injection

For plasma electrons to be accelerated to the desired energies, they must first have a sufficient velocity to exceed the phase velocity of the plasma wake. With sufficient energy, the electric fields present in the linear and nonlinear regimes can exceed their respective limits, E_0 and E_{WB}. When this occurs, electrons pushed in opposite directions by the ponderomotive force can oscillate with their paths crossing to form a

sheath around a near-spherical volume of evacuated electrons, this is commonly referred to as the "bubble" regime. The sheath creates a region of high electron density at the point where they cross at the back of the bubble. Electrons trapped in front of this intersection within the bubble experience rapid acceleration in the direction of laser propagation. Electrons at the back of the bubble with a velocity larger than the bubble phase velocity are rapidly accelerated. The highest energy electron beams are produced in the bubble regime. Injection occurs by self-trapping when background electrons are trapped without the assistance of any external forces. This is achieved by increasing the intensity of the laser pulse or the plasma electron density, which enables background electrons to reach velocities exceeding that of the bubble and enter the evacuated region of large accelerating gradient, by a form of wave-breaking. The properties of the resultant electron beam, such as energy spread can be very large for self-injection ($\sim$ 10%), which requires tuning of laser and plasma parameters to be just above the threshold for injection. A method was developed to determine where the trapping occurs in the interaction [105]. Up to 10^9 electrons can be subject to a sudden change in velocity in a very small volume ($\ll \lambda_p^3$), which can lead to emission of broadband radiation, which can be detected in the transverse direction, to give an indication of the acceleration length and laser pulse evolution time.

One approach to control injection is to use a second laser pulse to produce a slow beat wave that applies its own ponderomotive force to cause plasma electrons to be injected into the bubble. The pump pulse can be propagating perpendicular to the injection pulse, it can be collinear, or the two pulses can counter propagating. These methods have been shown to improve beam characteristics on several occasions, e.g. for an injection pulse propagating perpendicular to the pump pulse [106], which resulted in 25 MeV electron bunches with few femtoseconds duration and an energy spread of a few percent. A similar energy spread was achieved in another study using counter-propagating beams [107], but at lower energies (10 MeV). A similar approach has been shown to reduce the divergence of 250 MeV bunches that have an energy spread below 10% [81]. However, none of these succeeded in reducing the bunch energy spread significantly. Another technique using plasma density gradients to control injection

reduced the energy spread by up to 100 fold [108], but from a large initial momentum spread due to phase space rotation of the distribution. Reducing the plasma density has enabled high energy, sub-femtosecond electron bunches to be produced [109], and associated injection mechanisms have been accurately modelled [110]. Ionisation injection [95, 97, 111, 112] uses high-Z gas doped with a low-Z gas to enable ionisation of inner electrons at higher intensities of the laser pulse. Inner electrons are injected when the bubble cavity is already formed, thus increasing their likelihood of injection and acceleration.

2.4 Fricke dosimetry

In 1927, Hugo Fricke and his colleagues attempted to understand the internal mechanisms of aqueous solutions irradiated by X-rays. They discovered that haemoglobin – containing four ferrous (Fe^{+2}) atoms per molecule – changed into methaemoglobin containing iron in the ferric (Fe^{+3}) state, on irradiation [113]. They studied a simpler, ferrous sulfate solution and found that the initial concentration of ferrous ions had no effect on the reaction. This meant that the primary effect of the incident X-rays was on the water [114], and it was found that the percentage of ferrous ions that transformed into the ferric state was linearly related to the dose delivered. Its performance as a dosimeter was validated against an ionisation chamber and was found to be within 1% of agreement.

The radiolytic yield of the ferric ions, $G(Fe^{3+})$, is given by

$$G(Fe^{3+}) = 3G(H) + 2G(H_2O_2) + G(OH), \tag{2.21}$$

where $G(H)$, $G(H_2O_2)$ and $G(OH)$ are the radiolytic yields of hydrogen, hydrogen peroxide and hydroxyl radicals, respectively. Fricke solutions are aerated and therefore contain dissolved oxygen (O_2) which reacts with H radicals to form a hydroperoxyl radical, HO_2, which oxidises ferrous ions

$$Fe^{2+} + HO_2 \longrightarrow Fe^{3+} + HO_2^-, \tag{2.22}$$

which forms hydrogen peroxide

$$HO_2^- + H^+ \longrightarrow H_2O_2. \tag{2.23}$$

The hydrogen peroxide molecule then oxidises a ferrous ion

$$Fe^{2+} + H_2O_2 \longrightarrow Fe^{3+} + OH + OH^-, \tag{2.24}$$

while another ferrous ion is oxidised

$$Fe^{2+} + OH \longrightarrow Fe^{3+} + OH^-. \tag{2.25}$$

Therefore, three ferric ions are produced for every hydrogen atom, two for every hydrogen peroxide molecule, and one for every hydroxyl radical, giving the radiolytic yield in Equation 2.21. This linear combination of yields results in an abundance of highly reactive free radicals, thus making the Fricke dosimeter very sensitive. Further details on the mechanisms of Fricke dosimetry can be found in Shortt [115].

The Fricke solution is analysed with a UV-VIS spectrophotometer before and after irradiation to determine the change in optical density at 304 nm, the absorption wavelength of ferric ions. The dose can then be calculated

$$D_F = \frac{\Delta OD}{G(Fe^{3+})L\rho\varepsilon}, \tag{2.26}$$

where ΔOD is the change in optical density at 304 nm after irradiation, $G(Fe^{3+})$ is the radiolytic yield of ferric ions ($1.555 \pm 0.0176 \times 10^{-6}$ mol J^{-1}), L is the path length, ρ is the density of the Fricke solution, and ε is the molar linear absorption coefficient of ferric ions at 304 nm (2174 M^{-1} cm^{-1}). Further details can be found in deAlmeida et al. [116].

2.5 Resazurin assay

Resazurin is a blue-coloured dye originally used to determine the bacterial content of milk in 1929 [117], but is now commonly used for studying the response of cells to radiation [118–120]. It has more recently been used as a method of studying free radical production in irradiated water [121]. Resazurin solutions have similar mechanisms to Fricke solutions. Resazurin solution undergoes irradiation-induced chemical reactions, where blue, weakly-fluorescent resazurin (RNO, $C_{12}H_7NO_4$) reduces to pink, highly-fluorescent resorufin (RN, $C_{12}H_7NO_3$). Aqueous, or hydrated, electrons in the solution are scavenged by RNO in an intermediary reaction

$$RNO + e^-_{aq} \longrightarrow RN^{\cdot}O^-, \tag{2.27}$$

with a reduction rate constant, $k_1 = 4.3 \times 10^{10}$ $M^{-1}s^{-1}$ and a second reaction then occurs to produce the fluorescent RN

$$2RN^{\cdot}O^- + 2H^+ \longrightarrow RN + RNO + H_2O. \tag{2.28}$$

This reaction has a reduction rate constant, $2k_2 = 5 \times 10^7$ $M^{-1}s^{-1}$. The reduction rate constants, k_1 and k_2 (taken from Balcerzyk & Baldacchino [121]) are constants used to determine the rate of reaction Equations 2.27 and 2.28. The rate of reaction, r, is directly proportional to the concentration of the relevant reactants:

$$r = k \prod_{n=1}^{n} (C_n)^{a_n}, \tag{2.29}$$

where C and a are the concentration and reaction order of some reactant, n, respectively [122]. In other words, if the concentration of reactants in a solution increases, so too will the rate at which the reactions occur.

The two reaction rate constants above are very different for both stages of the reduction process, with k_2 being approximately 1,000 smaller than k_1. Therefore, the key reaction where resorufin is produced, occurs 1,000 slower than the initial scavenging of hydrated electrons (because concentrations of resazurin are identical), leaving a much

larger period of time where the $RN^{\cdot}O^{-}$ and $2H^{+}$ are sensitive to other reactions with radicals such as OH or hydrated electrons. The quantity of RN produced is proportional to the number of hydrated electrons scavenged, and the number of hydrated electrons produced is proportional to the energy deposited in the solution. The radiolytic yield, G, of RN is given by

$$2 \times G(RN) = -2 \times G(RNO) = G(e^{-}_{aq}), \tag{2.30}$$

as it requires one molecule of RN, and two hydrated electrons (from Equations 2.27 & 2.28).

We propose that the resazurin assay and its subsequent reduction into resorufin could be used as a method for determining the dose deposited in the solution.

Resorufin has a central emission wavelength of 585 nm, and an excitation wavelength of 530 nm. Following the reduction reaction, an excitation light source induces fluorescence in the solution. In our studies a continuous-wave LED source is used.

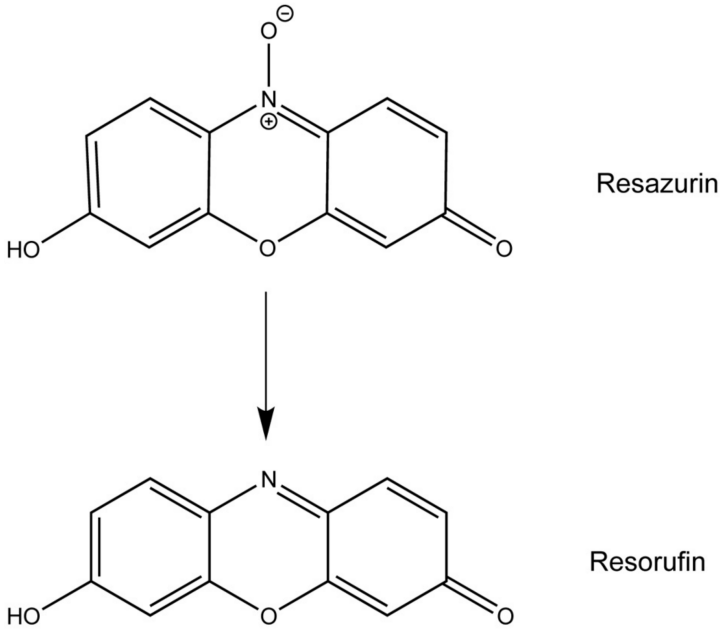

Figure 2.2: The reduction of resazurin to the highly fluorescent resorufin [123]. This process is irreversible so the increase in fluorescence caused by the increase in resorufin concentration is a reliable metric for the energy deposited in the solution.

The intensity of the emitted fluorescence is proportional to the amount of resorufin produced during irradiation. By calibrating the resulting fluorescence intensity to the dose delivered, it is possible to determine the dose delivered from the measured increase in fluorescence intensity. This provides a real-time dosimetry method, using common scientific equipment.

2.6 Electron beam irradiation in this work

Laser wakefield accelerated electrons were not used for the experiments described in this thesis, although it was the original intention. Unfortunately, the COVID-19 pandemic prevented experimental work for a considerable time, which caused a backlog of users at Strathclyde's SCAPA facility.

The calibration of the chemical dosimeter and the Fricke solution were undertaken using X-rays, as the dosimeter response is well established for Fricke, which resulted in an accurate calibration.

Experiments at the Commissariat à l'Énergie Atomique et aux Énergies Alternatives (CEA), described in Chapter 4, were carried out using γ-irradiation. The UHI100 laser driven electron beamline was not ready for use with our chemical dosimeter during the placement at CEA. Tests of the dosimeter with different irradiation modalities helped understand its versatility and its limitations.

Three experimental runs have been undertaken at CERN's CLEAR facility linear accelerator. CLEAR is an extremely reliable RF accelerator, capable of producing very high energy electrons at ultra-high repetition rates, similar to those which can be achieved with a plasma-based accelerator. The main difference is that an LWFA can produce electron bunches in the fs range, whereas the CLEAR linac produces electron bunches in the ps range. However, many of the beam parameters are comparable with LWFA-generated electron beams, therefore findings from the data presented here can be easily applied to electrons produced by LWFAs.

Chapter 3

Preliminary Dosimetry Study at CLEAR

This chapter explains the experimental procedure for testing the novel chemical dosimeter using very high energy electrons (VHEEs) from CERN's CLEAR facility.

3.1 The CLEAR beamline

The CERN Linear Electron Accelerator for Research (CLEAR) is a facility that has been in operation since 2017, featuring a 20-metre linac capable of accelerating electron microbunches to energies of 220 MeV, with charges of up to 1.5 nC. These microbunches can be repeated up to 150 times in 100 ns to produce macrobunches of up to 75 nC, and these can be delivered at a maximum repetition rate of 10 Hz [124]. A schematic of the beamline and all of its components is shown in Figure 3.1. The beam size can be varied by adjusting the parameters of the three magnet triplet quadrupoles, and the beam charge and current are monitored using an integrating current transformer (ICT 915) at the end of the line. The beam is diverted to a scintillating crystal screen (BTV 930) using the final dipole magnet (BHB 900), where the electron energy can be determined based on the angle of deflection, while a second screen (BTV 910) is used to monitor the beam profile.

Before all runs, the beam was aligned to a 9 mm diameter aperture in the side

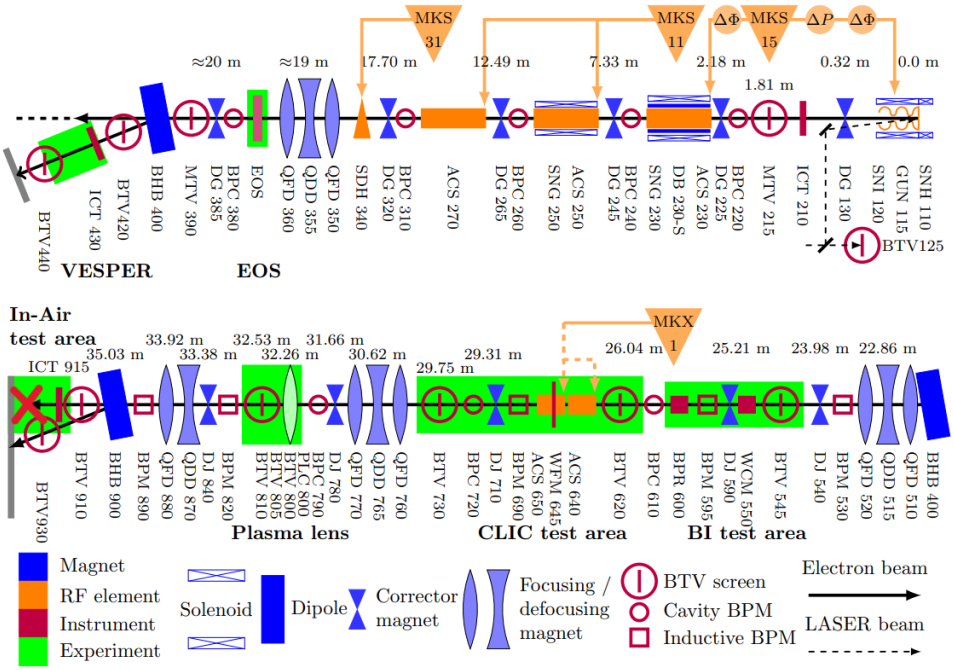

Figure 3.1: Technical drawing of the CLEAR linear accelerator beamline [124]. The beam travels from right to left along the upper section first, then the lower section. The experiments took place in air at the end of the beamline, immediately after ICT 915 (denoted with a red X).

of our cuvette holder, and the beam size and energy spectrum measured. The beam size was varied throughout the experiment, while the energy was kept approximately constant, with an average value of 193 MeV. Two different beam sizes were investigated: a "small" beam of size $\sigma_x = \sigma_y = 1$ mm, and a "large" beam size of $\sigma_x = \sigma_y = 1.5$ mm. The parameter σ is a good approximation of the RMS radius of the beam. More specifically it is the standard deviation of a Gaussian distribution, which is described by

$$f(x) = \frac{1}{\sqrt{2\pi\sigma^2}} \exp\left[-\frac{(x-\mu)^2}{2\sigma^2}\right], \tag{3.1}$$

where μ is the central position of the distribution, which in the case of beam analysis is always zero. This distribution is shown in Figure 3.2, along with various multiples of σ and the full-width at half-maximum (FWHM). Electron bunch spatial profiles are typically approximated using Gaussian profiles.

In addition to beam size, two dose rates were used: an ultra-high dose rate (UHDR) of 10^9 Gy/s, and a conventional dose rate (CONV) of < 0.1 Gy/s. All four combinations

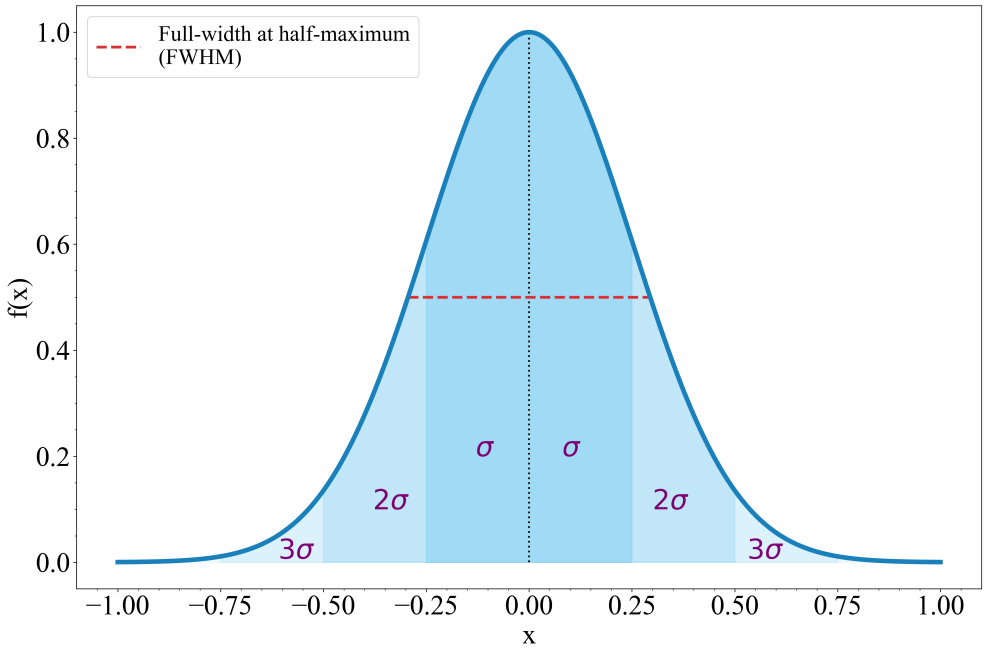

Figure 3.2: Example of a Gaussian distribution, used to approximate the VHEE beam profile. Around 68.2% of electrons will be found in the region between $-\sigma$ and σ, 95.4% in the region between -2σ and 2σ, and 99.5% of electrons are found between -3σ and 3σ. The red line is the full-width at half-maximum (FWHM), approximately 2.355σ. Both FWHM and σ are commonly used when discussing particle beam geometry.

of these parameters were investigated to observe their effect on the dosimeter response.

3.2 Methods

3.2.1 Dosimeter set-up

The beamline at CLEAR is as described in the previous section with the dosimeter apparatus placed 20.5 cm from the integrating current transformer (ICT 915). Figure 3.3 shows the experimental set-up. A fixed Thorlabs cuvette holder (CVH100) made of aluminium is used to house the cuvettes during irradiation. Four holes in the sides of the holder allow the electron beam to enter and exit the cuvette, and the excitation LED beam (central wavelength of 530 nm) to be focused into the centre of the solution, perpendicular to the beam. The emitted fluorescence (585 nm) passes through a plano-convex lens (focal length, $f = 20$ mm) housed inside an attached fibre adapter, and is focused onto an optical fibre directly opposite the LED. It is then transported to the

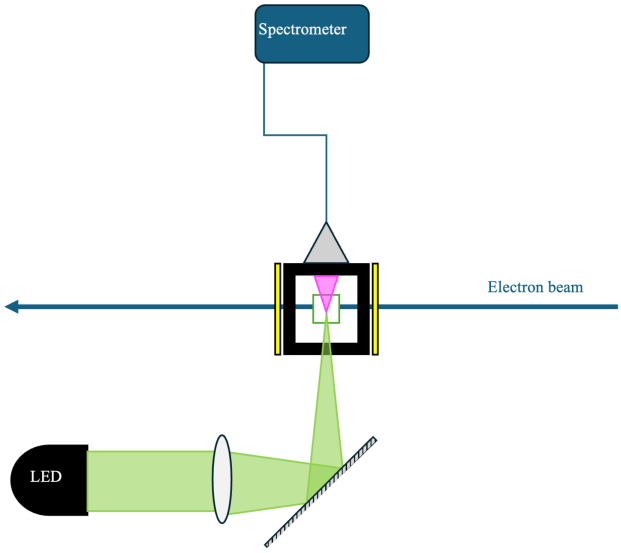

Figure 3.3: Drawing of the dosimeter set-up. The excitation LED beam in green is focused onto the solution in the cuvette after irradiation, which then emits pink fluorescence. After passing through a fibre adapter containing a 0.5-inch diameter plano-convex lens, the fluorescent light is focused onto an optical fibre and transported to the spectrometer. There is one Gafchromic film piece either side of the cuvette holder, measuring the dose immediately before and after the sample.

spectrometer to be analysed. Unwanted excess LED light is filtered using a long pass filter, with a cut-off wavelength of 550 nm.

3.2.2 Resazurin solution preparation

The dosimeter solution is prepared by adding 5 mg of Sigma-Aldrich resazurin sodium salt to 1 L of a buffered water solution [125] to achieve a concentration of 19.9 μM. 0.584 mL of ethanol (concentration, 10^{-3} M) is added to help scavenge OH radicals which could recombine with hydrated electrons, necessary for the reduction of resazurin into resorufin (see Chapter 2.5). Finally, the solution is stirred for at least 10 minutes. When combined, the solution is stored in the fridge where it can be nominally kept for several weeks. However, the experiment lasted one week.

When required for irradiation, the solution is added to PMMA cuvettes, which had been rinsed out with ultra-pure water. The solution was de-aerated with a neutral gas prior to irradiation (nitrogen was used in this experiment with $>$ 99% purity). For each cuvette containing solution, the lid is removed from the cuvette and nitrogen bubbled through the solution using a clean hypodermic needle for 2 minutes per cuvette, after

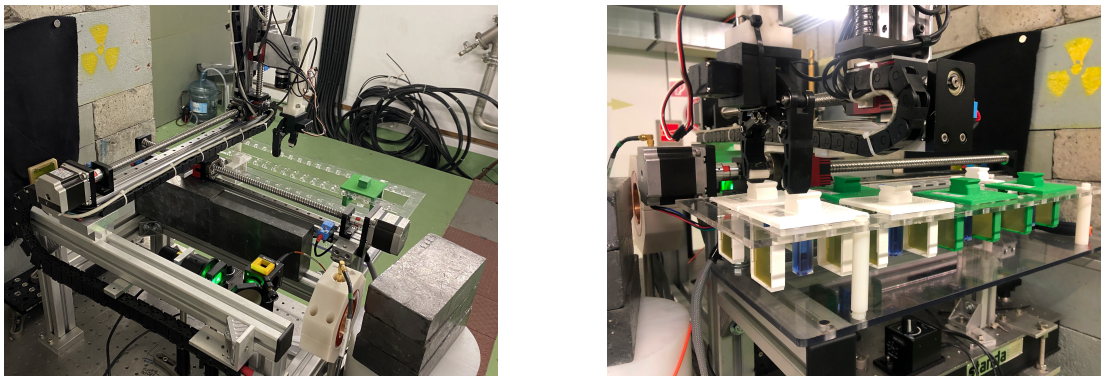

(a) (b)

Figure 3.4: Target area of the experiment showing (a) the dosimeter set-up as shown in Figure 3.3 (b) the samples and Gafchromic film stored to the side of the dosimeter set-up.

which the rubber lid is re-attached, making the cuvette ready for irradiation.

3.2.3 Irradiation of samples

The samples are held in custom-made 3D-printed plastic holders placed at the side of the target area (as shown in Figure 3.4), away from radiation. When the beam has been aligned and the desired parameters obtained, the first cuvette is placed in the cuvette holder using a robotic arm. CLEAR's robotic arm enabled up to six samples to be irradiated in a single run, without the need for re-entry to the beam tunnel.

Gafchromic film (see Chapter 3.3) was placed both upstream and downstream of each cuvette. This allowed the cumulative dose to be measured when the cuvette was irradiated multiple times, up to the desired dose. For doses up to 50 Gy, EBT3 film [126] was used, and for higher doses, HD-V2 film [127] was used.

During irradiation, the excitation LED was turned off to avoid potential overheating – the signal fluctuations associated with this are investigated in Chapter 4.3.6. After each pulse was delivered it was remotely turned on to enable the fluorescence spectrum to be measured. This was performed as quickly as possible after irradiation, which was approximately 10 seconds for every sample.

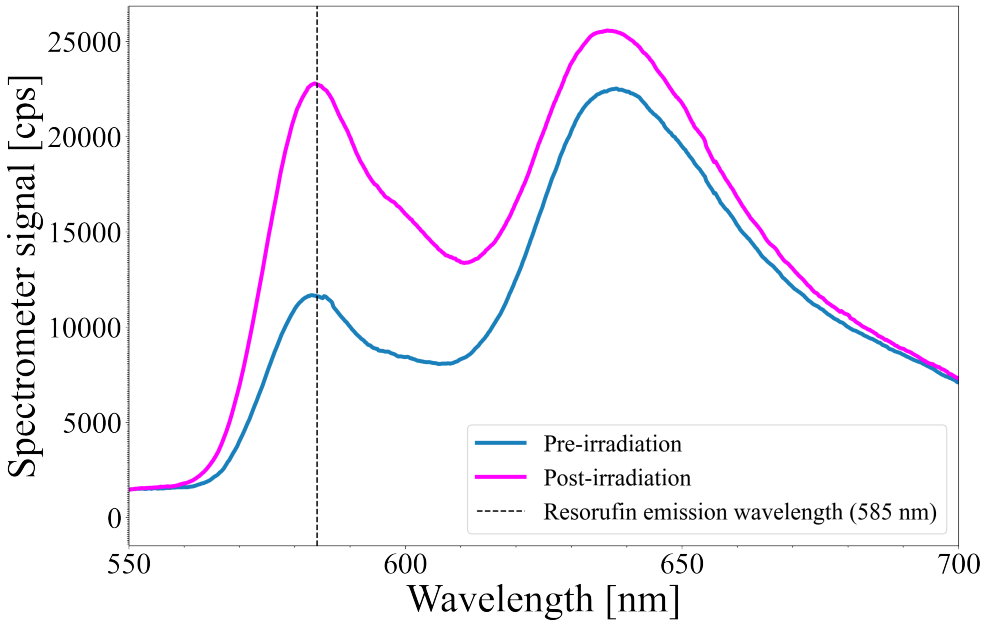

Figure 3.5: Example spectrum of raw spectrometer signal before and after the solution received around 460 Gy from VHEEs. The increase in signal at 585 nm enables the dose delivered to be quantified. The second peak emitted around 640 nm is from resazurin itself.

3.2.4 Spectral measurements and analysis

Upon excitation by the LED, fluorescent photons of 585 nm are emitted in all directions. A 550 nm long-pass filter is placed directly opposite the incident LED, between the cuvette and the collection lens. This reduces the LED intensity and allows the fluorescent photons to be transmitted. The transmitted photons then pass through a 0.5" diameter, 20 mm focal length plano-convex lens, housed in a Thorlabs fibre adapter, which focuses the light onto a 5 metre-long optical fibre connected to a Flame UV-vis mini spectrometer (model: FLAME-T-XR1-ES). This is connected to an external computer running Ocean Optics spectroscopy software, OceanView (product version: 2.0.8). The integration time is adjusted for each reading to maximise the signal. The signal difference is corrected in the analysis stage by converting counts to counts-per-second. The spectrum is saved multiple times for each sample, after each irradiation, until the desired total dose is reached.

Figure 3.5 shows two raw spectra of the solution, before and after irradiation with 200 MeV electrons from the CLEAR linac, delivering around 460 Gy. The fluorescence

increase at 585 nm is used as a dose-determining metric. The second peak at around 640 nm is emission from resazurin in the sample, which is weakly fluorescent. As explained in Chapter 2.5, resazurin is converted directly into resorufin at the expense of two hydrated electrons. Because of this, it is expected that the 640 nm peak will decrease at the same rate as the 585 nm peak increases, but this isn't necessarily the case. Not only does the detected fluorescence at 585 nm increase, but the curve widens and the spectrometer measures the overlap of the two spectral peaks. This results in an increase in both, but a relatively smaller increase at 640 nm.

All the spectra for a sample are saved as .txt files, which are processed using a Python script that plots a double Gaussian fit to the fluorescence peaks at 585 nm (the emission wavelength of resorufin) and 640 nm. The mean value of the resorufin peak $\pm$ 5 nm for all spectra are stored in an array, and plotted against the estimated dose (the actual dose is only plotted when the Gafchromic film had been scanned around 24 hours later). This was carried out for all samples and the various beam parameters were compared. Each set of irradiations comprised three samples for statistical purposes, where the mean of the three spectra is used for plotting and the variations between the three were used to quantify errors.

3.3 Dose determination using Gafchromic film

It is not only crucial to know the absorbed dose to a patient, but it is also important to know the spatial distribution of the absorbed dose. The dose response of a dosimeter, i.e. the measurable quantity which changes as dose is delivered, needs to be linear within a range of doses. As different modalities and treatment plans can deliver radiation at a variety of dose rates, the dosimeter also needs to be independent of dose rate – this allows for dosimetric studies in the FLASH regime (see Chapter 1.4). Other important qualities of a desirable dosimeter are its spatial resolution, readout time, accuracy and precision [128]. Such a dosimeter that meets all these criteria for all applications does not yet exist, therefore one must select a dosimeter that is best suited for the use.

One dosimeter widely used because of its high spatial resolution and low energy dependence is radiochromic film, specifically Gafchromic^{TM} film. To calibrate our re-

sazurin dosimeter, the film is used to measure the delivered dose, which can then be compared with the change in 585 nm fluorescence signal. After multiple runs, providing sufficient certainty, a direct relationship between the measured fluorescence signal and the delivered dose can be determined. This relation can then be used in future experiments, allowing for real-time dosimetry. Several models of the films exist, and have various structures and dynamic ranges. EBT3 is one commonly used version of the film, which has a dose range of 0.1 – 20 Gy. For our CLEAR study, we were interested in doses outwith the range of EBT3, so EBT-XD and HD-V2 film were used. These have dynamic dose ranges of 0.1 – 60 Gy and 10 – 1000 Gy, respectively.

3.3.1 Gafchromic film dosimetry

EBT-XD film is composed of a 25 μm active layer sandwiched between two layers of polyester, each 125 μm thick, and can be irradiated from both directions. HD-V2 film on the other hand comprises an 8 μm active layer with a 97 μm polyester substrate on one side, so must be irradiated and scanned through the same side every time.

When ionising radiation is incident, it causes the dye within the active layer to darken – the darker the dye becomes, the higher the dose deposited. After irradiation, the user must wait 24 hours before the film can be scanned in a flatbed scanner and undergo analysis. Over the first 24 hours post-irradiation, the net optical density, ($netOD$) values can vary by a few percent depending on the dose delivered. The darkening of the film and its time-dependence post-irradiation are shown in Figure 3.6. For accurate dosimetry it is therefore important to wait until the $netOD$ has stabilised. $NetOD$ is a measure of the darkening of the film, and is defined as follows.

Starting with the Beer-Lambert law [131],

$$A = log_{10}(I_0/I), \tag{3.2}$$

where A is the absorbance of a material, I_0 is the intensity of the incoming radiation and I is the intensity of the outgoing radiation. We can replace A with $netOD$, and

change the intensity values for pixel values

$$netOD = \log_{10}(PV_{before}/PV_{after}). \tag{3.3}$$

PV_{before} and PV_{after} are the pixel values of the irradiated region of the scanned film before and after irradiation, respectively. For peak dose, the minimum pixel values are used and for average dose, the mean pixel value in the region is used.

3.3.2 Film preparation and handling

The film segments used for the experiment were prepared in an Epilog Laser Fusion Maker, which has a CO_2 laser capable of accurately cutting them to size and labelling them. Each piece was 35 mm x 40 mm and placed immediately upstream and downstream of the cuvette, held by 3D-printed holders designed at CLEAR. The film was always handled with nitrile gloves to avoid any natural skin oils affecting the readings. They were kept in the dark until required, then removed from their holders and placed back in the dark as soon as possible post-irradiation, for 24 hours, before being scanned.

3.3.3 Readout method and dose calculation

For each type of film used, a calibration process was performed by CLEAR to gain accurate knowledge of the doses. The films were previously calibrated using the Oriatron

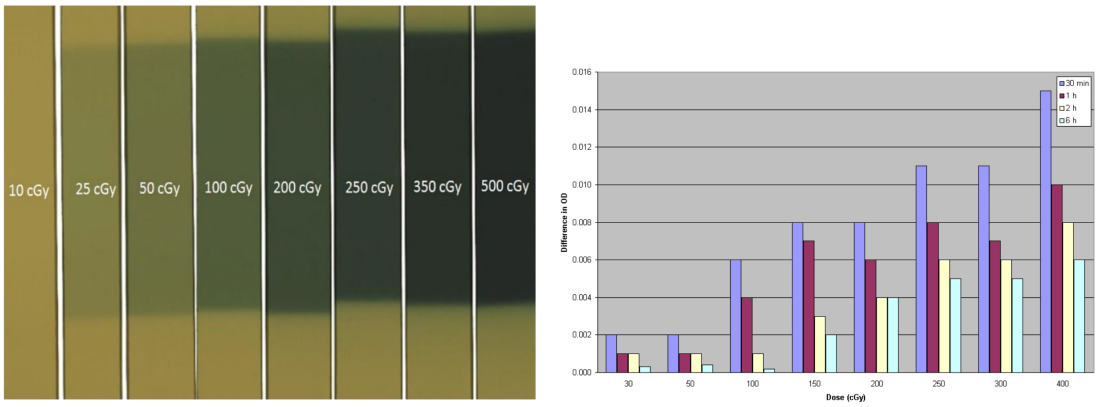

Figure 3.6: Gafchromic EBT3 film showing darkening for a range of doses up to 500 cGy [129], and the time dependence of the *netOD* value post-irradiation for a range of doses [130].

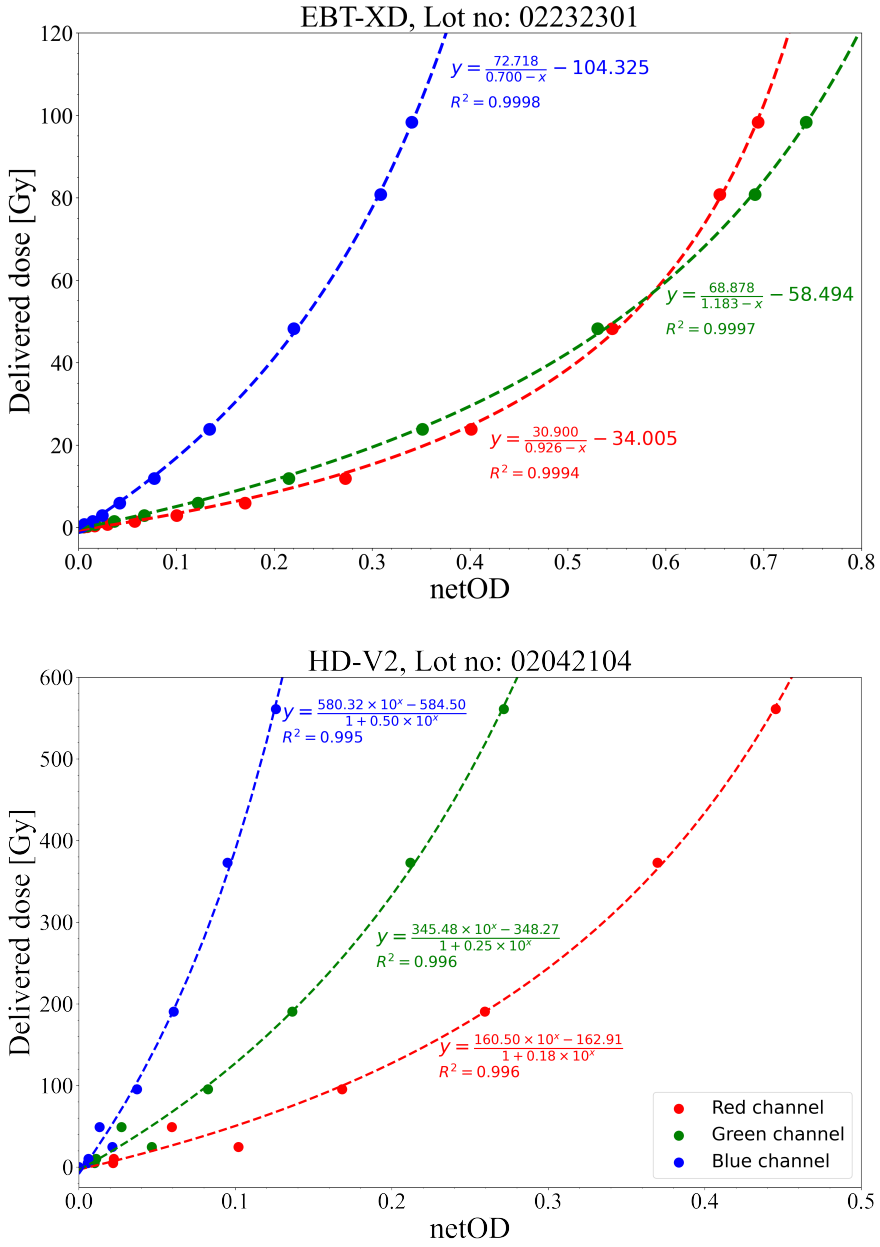

Figure 3.7: Calibration curves for EBT-XD (top) and HD-V2 (bottom) Gafchromic films, the equations of which were used in our experiment for dose calculation. The red channel, with the greatest sensitivity in both films, was used.

eRT6 linac at the Lausanne University Hospital in Switzerland [132]. They were irradiated with 6 MeV electrons and the dose was calibrated using an Advanced Markus ionisation chamber, then the $netOD$ values for the various doses were measured and plotted. Over a range of values spanning beyond the dynamic dose range, a dose calibration curve could be obtained. EBT-XD film was irradiated with doses between 0.1 and 102.4 Gy, and HD-V2 was irradiated with doses between 5.1 Gy and 561.1 Gy. These calibration curves are presented in Figure 3.7, where they clearly show the increased sensitivity of the red channel in both sets of film. It is for this reason that the red channel has been used for dose determination for the entire experiment. The manufacturers of the films, Ashland, recommend fits that are easy to invert, and behave rationally, requiring fewer calibration points [127, 133]. These fits are shown in Figure 3.7.

The R^2 method was used for determining characterise the goodness of fit [134]. Each experimentally obtained data point is displaced from the theoretical fit on the plot at the same point in the x-axis. In other words, its y-value, y, will differ slightly from the predicted y-value, $\hat{y}$. For each point, this distance – or variation – is squared, then they are all summed. This is known as the sum squared regression (SSR). Another value needed is the total sum of squares (TSS), which is the mean of all the predicted y-values ($\bar{y}$), subtracted from each measured y-value, then all summed and squared. The R^2 value is then given by

$$R^2 = 1 - \frac{SSR}{SST} = 1 - \frac{\sum (y_i - \hat{y}_i)^2}{\sum (y_i - \bar{y})^2}. \tag{3.4}$$

All curves in Figure 3.7 have R^2 values greater than 0.99.

3.4 Experimental results

A total of six experimental runs were performed over three days, with six samples irradiated per run. Each run used either ultra-high (UHDR, 10^9 Gy/s) or conventional (CONV, < 0.1 Gy/s) dose rates, with a small beam ($\sigma_{x,y} = 1.1$ mm) or a large beam ($\sigma_{x,y} = 1.5$ mm). In runs 1 – 5, three samples were irradiated with ten shots of 2 Gy,

and three samples with ten shots of 4 Gy. In the final run each sample was irradiated by a single shot of increasing dose from 50 - 500 Gy. Each run is outlined below.

- Run 1: UHDR, small beam
- Run 2: UHDR, small beam (a direct repeat of Run 1)
- Run 3: CONV, small beam
- Run 4: UHDR, large beam
- Run 5: CONV, large beam
- Run 6: UHDR, small beam, high doses

The increase in the 585 nm fluorescence intensity for runs 1 – 5 are shown in Figure 3.8. During run 1, beam optimisation was still in progress, and the data was not usable so it was repeated in the following run. From this data alone, one can already notice a clear inconsistency with data obtained from a "small" electron beam size. A larger beam size reduces the sample-to-sample variation and indicates a sensitivity to the geometry of the beam. The data from run 6, where much higher doses were delivered (up to around 500 Gy), are shown in Figure 3.9. These samples show a general linear trend, which is in much closer agreement with other samples for small electron beam sizes. This suggests the sensitivity arising from the dosimeter/beam geometry diminishes at higher doses.

3.4.1 Varying the dose rate

Conventional dose rates are usually of the order of a few mGy per second, whereas FLASH effects are demonstrated for dose rates greater than 40 Gy/s – around 100 times greater. For the tissue-sparing effect of FLASH to be applied in the clinic, accurate dosimeters are needed. These dosimeters must be dose-rate independent if they are to be used for FLASH studies.

The CLEAR beamline, as described in Chapter 3.1, can deliver up to 150 electron bunches in a single macropulse train, which are delivered at a maximum repetition rate

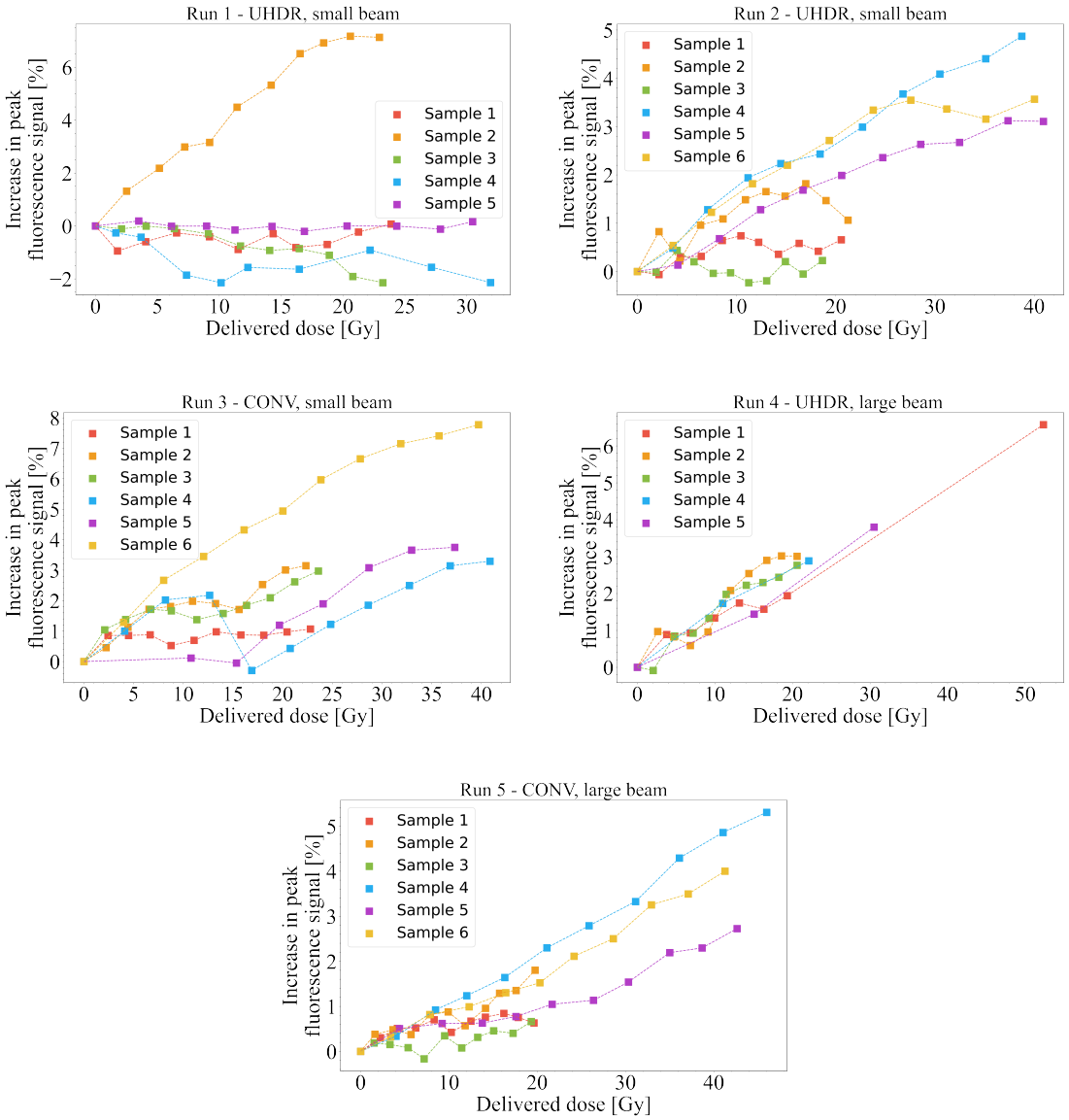

Figure 3.8: Data for all samples in runs 1 – 5 of the first CLEAR experiment. Run 1 had to be repeated due to the beam being optimised during the run. Samples were irradiated ten times with either 2 Gy or 4 Gy (estimated) per shot. The peak value of the resorufin fluorescence (585 nm) is used here to quantify the change in the solution. The delivered dose is determined using Gafchromic EBT-XD film.

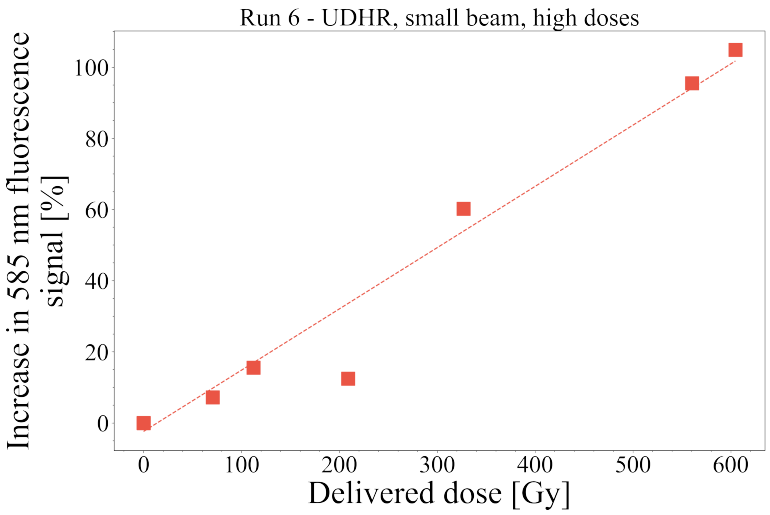

Figure 3.9: Data for the final run of the first CLEAR experiment. Samples were irradiated with single shots of increasing dose, from around 50 Gy up to around 500 Gy, while measuring the peak of the resorufin fluorescence peak (585 nm). The delivered dose is determined using Gafchromic HD-V2 film.

of 10 Hz. Each macropulse can contain as much as 75 nC of charge and can be delivered in 0.1 ps – 100 ns. This is how an ultra-high dose rate (UHDR) of greater than 40 Gy/s can be achieved. By changing the parameters of the beam delivered, the dose can be spread out over several trains to deliver an equivalent charge (and therefore, dose) in a longer time. This is how we achieved conventional (CONV) dose rates in our experiment, which were around 0.25 Gy/s.

We studied the impact of two dose rates on the dosimeter response as measured using our spectrometer, for both our small beam and large beam. Here, σ is the standard deviation of the particles within the beam, such that the full-width at half-maximum size of the Gaussian beam, $FWHM = 2\sqrt{2\ln 2}\sigma$ (see Chapter 3.1). A conventional dose rate of around 0.25 Gy/s was achieved by delivering 10 pulse trains of around 120 pC at a repetition rate of 0.833 Hz, the minimum frequency of the linac. The UHDR was considerably higher, and was of the order of 10^9 Gy/s, delivering the entire desired dose in a single electron bunch of length < 100 ns. The dosimeter was tested up to a dose of 70 Gy, and the results are shown in Figure 3.10.

Figure 3.10 shows the difference in response of the dosimeter for conventional dose rates and for ultra-high doses rates. There is no strong evidence from the data that these measurements are dose-rate independent. It appears that for a small beam there

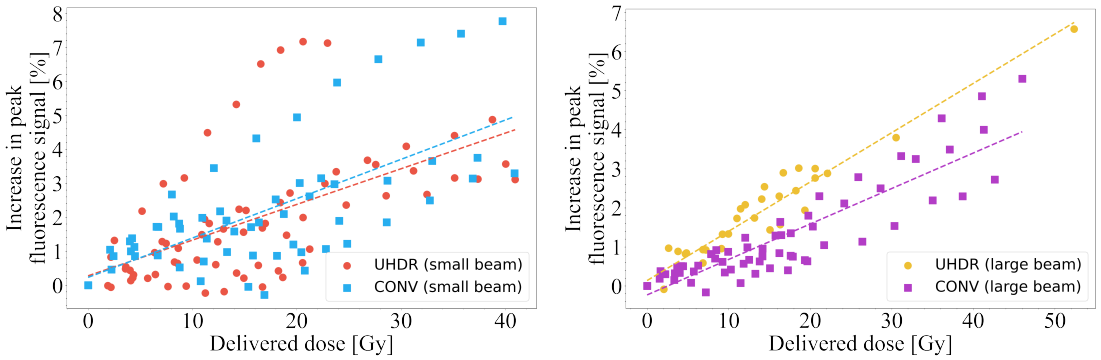

(a) CONV vs UHDR for a small beam

(b) CONV vs. UHDR for a large beam

Figure 3.10: The increase in 585 nm fluorescent signal at conventional dose rate (CONV) and ultra-high dose rates (UHDR). The two dose rates were compared using (a) a small beam of $\sigma = 1.1$ mm in both x and y, and (b) a large beam of $\sigma = 1.5$ mm in x and y.

is larger variability, therefore it cannot be confirmed with certainty. However, the two plots follow very similar, linear trends for both dose rates. The plateaus seen around 20 Gy in both plots are likely due to the bubbling method which was found to be quite inefficient during later studies (see Chapter 4.3.1). These particular samples may have had a greater amount of oxygen still present in the solution, reducing the scavenging capacity.

Delivering the dose with a larger beam produced a much more consistent fluorescence response as the dose increased, compared with the smaller beam. Together, this data suggests that although dose rate independent, our chemical dosimeter is very sensitive to beam and irradiation geometry, such as the beam size, and possibly even the beam position in the cuvette.

3.4.2 Varying the beam size

During the experiment, two beam sizes were used. These were measured using CLEAR's dedicated yttrium aluminium garnet (YAG) scintillating screen. The smallest beam size achieved for the desired doses was a circular beam with a σ of 1.1 mm along both the x and y-axes, which is the "small" beam referred to here. We then expanded the beam to explore the effect of beam size on the response of the dosimeter for the same dose delivery. This is referred to as the "large" beam, which had a σ of 1.5 mm in both x and y. As can be seen in Figure 3.11, changing the size of the beam had a

noticeable effect on the dosimeter response, both for UHDR and CONV. For both dose rates, an increased beam size resulted in a smaller increase in fluorescence for the same dose. This suggests that the geometry of the system is very important for achieving consistent results. It is believed that this could be due to the fact that the solutions were not stirred prior to spectral measurements, and different beam sizes would affect the concentration of fluorescent resorufin in the volume excited by the LED.

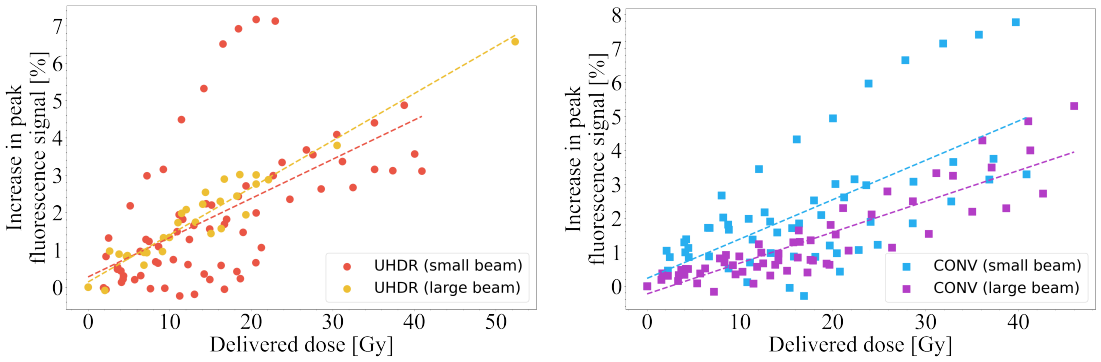

(a) Small vs. large for a UHDR beam

(b) Small vs. large for a CONV beam

Figure 3.11: The increase in 585 nm fluorescent signal for small beams ($\sigma = 1.1$ mm in both x and y) and large beams ($\sigma = 1.5$ mm in both x and y) at the two dose rates: (a) UHDR, and (b) CONV.

3.4.3 The beam position with respect to the cuvette

Using the Gafchromic film placed upstream and downstream of the cuvette, the mean position of the beam over the entire irradiation of each sample could be estimated. The films were scanned, and the position of the peak dose value was taken as the mean central position of all the beams delivered. As the films were well aligned with the cuvette, we could then plot these positions with respect to the centre of the cuvette, as shown in Figure 3.12. The shaded green area of the plot is the approximate volume illuminated by the focused excitation LED and the dotted circles represent the diameters of the delivered electron beams (determined by the σ values as measured on the Gafchromic film scans). As the films were irradiated multiple times, slight variations in the beam position result in the σ values being slightly larger than for a single shot. Therefore, in reality, the beam diameters are likely to be slightly smaller than those plotted. It becomes clear that the position of the beam, if the solution is unstirred, could also have

an impact on the reliability of the measured spectrum.

The diffusion rate of resorufin in the solution is constant for all the solutions, and generally diffusion is a very slow process, taking around 1.59×10^5 seconds to diffuse a radial distance of 1 cm (see Appendix A.2 for details). The chemical mechanisms involved are complex, but by stirring the solution during measurements it would be expected that the signal would become much more stable and reliable. This would eliminate uncertainties arising from the limited volume illuminated by the LED.

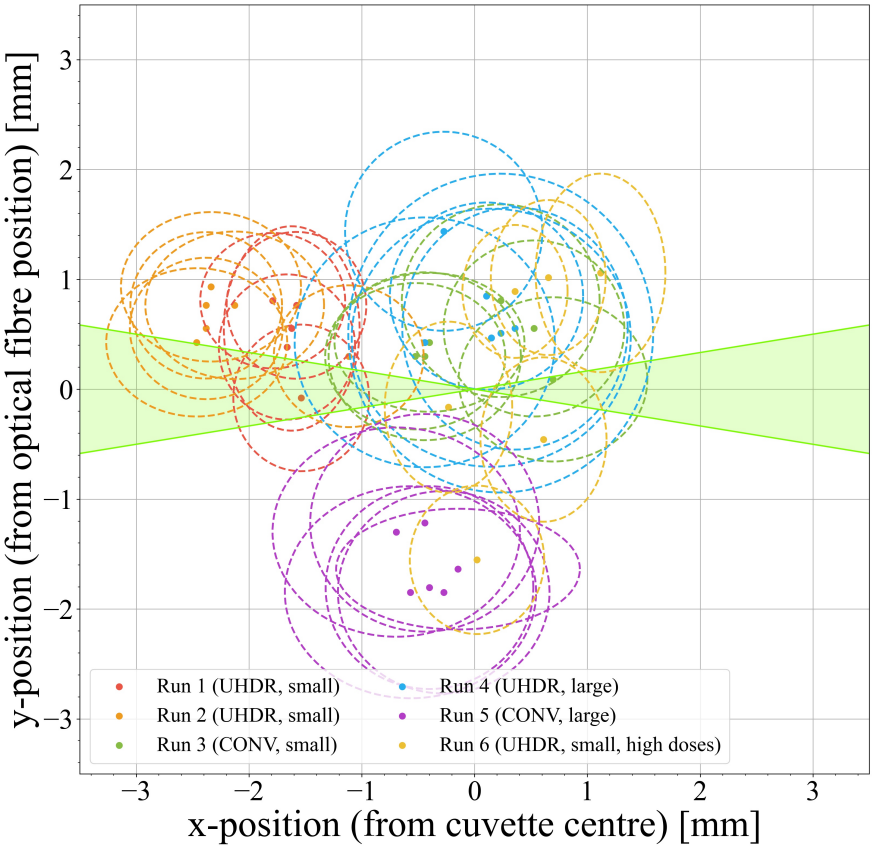

Figure 3.12: Mean position of the beam for each sample throughout the runs, with respect to the focal point of the LED in the solution. The dotted circles represent the σ values obtained from Gafchromic film scans, and the green area is the region of the focused excitation LED beam.

3.5 Discussion and next steps

From the data obtained during this run at CLEAR, we have demonstrated a working chemical dosimeter, where the emitted fluorescence increases with dose and is approx-

imately linearly. We believe it can be used as a dosimeter for doses up to 500 Gy, and likely higher still, as the signal showed no sign of saturating. However, due to potential misalignment of the electron beam with the LED excitation volume, an uncertainty still exists. While doses up to 500 Gy aren't generally useful in a clinical sense, it does suggest that it can be used for multiple smaller clinical dose deliveries, without needing to be replaced. The data suggests that the fluorescence response is independent of dose rate, but is sensitive to various external factors. These include the size and position of the incident electron beam. The preparation and handling procedure of the solution could also be of importance, and it is essential that a thorough protocol is developed to ensure accurate and repeatable results in the future. By stirring the solution, much more consistent results are likely to be obtained because the beam position loses its significance and the resorufin produced will be distributed homogenously throughout the cuvette. Electron beams used in clinical applications are much more divergent than those produced by the CLEAR accelerator. This would result in a larger beam than those used in this study, which would reduce the impact of the beam geometry discussed here. Additionally, there will be further beam divergence caused by the tissue medium. This effect and how to overcome it with a focused VHEE beam, is investigated further in Chapter 6. A spread out beam was not tested in these experiments as it would reduce the dose rate and the dose, and testing the dosimeter at UHDR with high doses was the primary goal.

Chapter 4

Resazurin Chemical Dosimeter: Establishing a Methodology

The main objectives of this chapter are to formulate a procedure for using resazurin solution to produce accurate and repeatable dosimetry measurements. In addition, we aim to develop an understanding of the underlying chemical processes, and consider how they might affect the response of the dosimeter. This allows to lay the ground work for future studies, ultimately ensuring optimal reliability. The work presented here was started at SCAPA with X-ray irradiation, and continued shortly afterwards at the CEA with gamma irradiation.

4.1 Dose calibration for X-ray irradiation

To know the doses being delivered in the chemical dosimeter, the X-ray source calibration was undertaken using another, well established dosimetry method. For this, the Fricke dosimetry method was used, as this also relies on chemical reactions to determine dose, which was an analogous method, compared with radiochromic film. However, radiochromic film was still used in parallel for completeness. Briefly, Fricke dosimetry is based on oxidation of Fe^{2+} into Fe^{3+} in acidic solution. The main constituents are ultra-pure water, sulfuric acid, sodium chloride and ferrous sulfate. The quantities of these were taken from deAlmeida et al. [116], resulting in a solution density of $\rho = 1.023$

g cm^{-3}. The path length, l, for our experiments was 1 cm. See Chapter 2.4 for further information on Fricke dosimetry.

Gafchromic EBT3 film dosimetry

In addition to Fricke dosimetry, the X-ray source was calibrated using EBT3 Gafchromic film. The scanner used was different to that used for the CLEAR experiments, resulting in a different calibration curves for this experiment. The scanning procedure is described below.

An Epson 10000XL Pro Scanner was used in these studies. After performing 10 scans of an empty scanner bed to warm the scanner up, the irradiated films were scanned in the centre of the scanner bed in landscape orientation (the shortest side perpendicular to the scanning motion) to maximise the light captured by the system. Of the three colour channels (red, green and blue), the red channel is the most sensitive at doses below 150 Gy [135], therefore this channel was used for the dosimetry studies.

To convert $netOD$ to dose, a calibration curve from previous studies with 160 kV X-rays was used [136], and the following conversion formula was used to determine the dose delivered,

$$D_{RCF} = 0.11 + 7.04(netOD) + 12.82(netOD)^2 + 27.84(netOD)^3. \tag{4.1}$$

The ImageJ software was used to process each film sheet which was scanned three times. They were concatenated and the average pixel values were calculated. The region of interest was then selected to be an area at the centre of the film, equivalent to the area of the face of the solution in the cuvette (2.5 cm $\times$ 1 cm). The minimum pixel value within this region was taken to be the PV_{after} as defined in Equation 3.3. One pixel equals 0.25×0.25 mm^2. PV_{before} was determined using an identical method with an un-irradiated sheet of film.

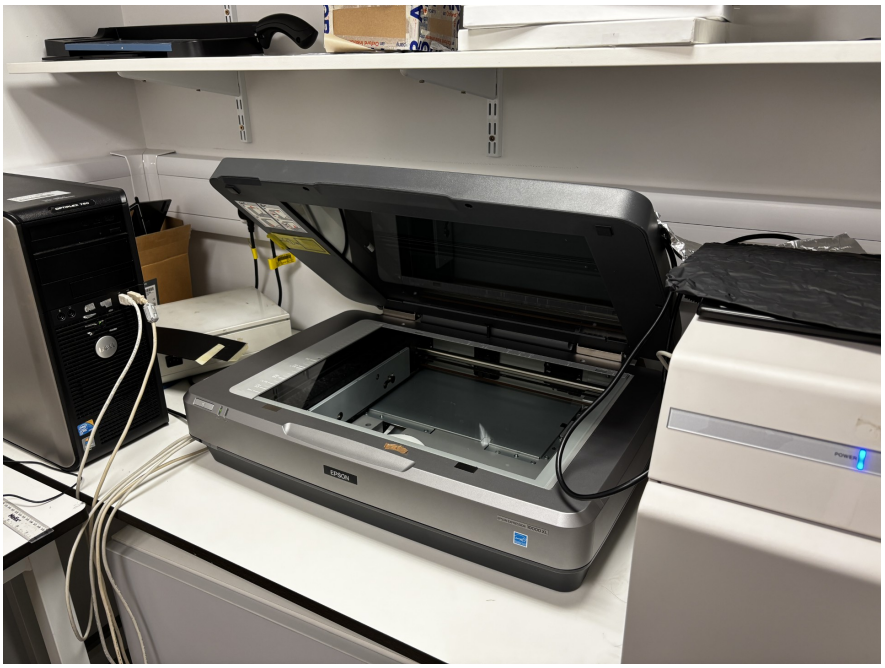

Figure 4.1: Epson 10000XL Pro flatbed scanner used for radiochromic film scans at SCAPA. After ten warm-up scans, film sheets were placed at the centre in landscape orientation, scanned three times and averaged to determine the dose.

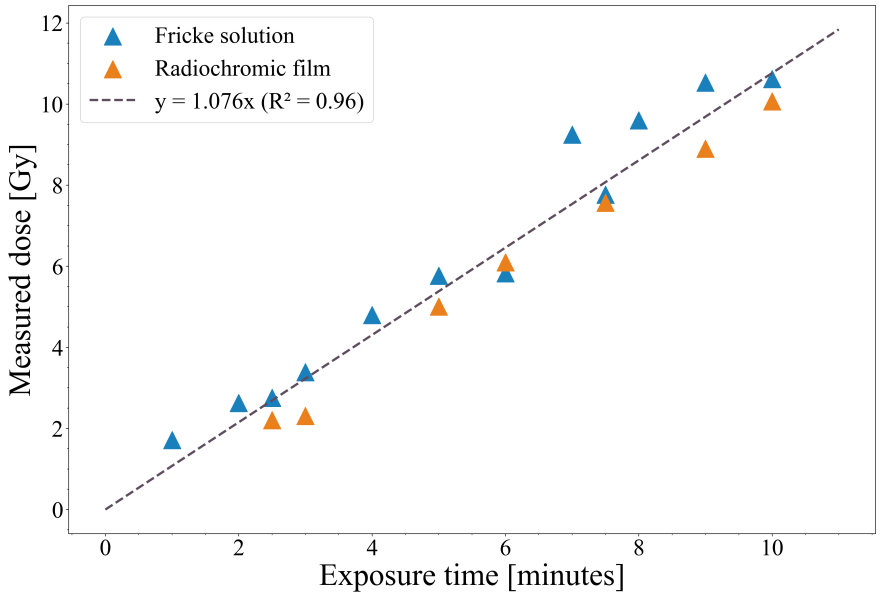

Figure 4.2: Dose calibration curve for X-ray irradiations at SCAPA, measured with Gafchromic film and Fricke solution, which were irradiated over a range of times, for fixed beam parameters: voltage, V = 160 kV; current, I = 1.5 mA; source-to-sample distance, SSD = 10 cm. The source, with these settings, has a constant dose rate of 1.076 Gy/min.

Results of dose calibration

Fricke solution and EBT3 films were irradiated for a range of exposure times up to 10 minutes, all with consistent X-ray beam parameters: voltage, V = 160 kV; current, I = 1.5 mA; source-to-sample distance, SSD = 10 cm. Using the methods previously described, and Equations 2.26 and 4.1, the corresponding doses were determined. Figure 4.2 shows the dose delivered by the X-ray source, which increases linearly with exposure time, and has a constant dose rate of 1.076 Gy/min. The fit was plotted using the curve_fit function from Python's SciPy library, and had an R^2 value of 0.96. This enabled the doses delivered to our samples of resazurin solution to be determined with confidence. Identical cuvettes were used for the Fricke and the resazurin solutions, and the same volume of each solution was irradiated. Furthermore, the beam size at the cuvette position was much larger than the cuvette itself. This eliminated any dose uncertainties which would arise from slight changes in solution volume.

4.2 General preparation and handling

The method of preparation began with the creation of a stock of buffered water, made by dissolving 603.383 mg of sodium phosphate dibasic heptahydrate and 1.069 g of sodium phosphate monobasic monohydrate into 1 L of ultra-pure water. Resazurin powder from Sigma-Aldrich is added to the buffered water, with a concentration of 10^{-6} M. Finally, a small amount (0.584 mL) of ethanol is added to scavenge the hydroxyl radicals that could recombine with the hydrated electrons instead of the resazurin. The solution is then stirred for at least an hour, and can then be stored in the fridge, where it will keep for several months. As it is sensitive to light it must be kept shielded from ambient light.

4.2.1 De-aeration time

When distributed into cuvettes for irradiation, the samples must be de-aerated by purging with an inert gas such as nitrogen or argon for several minutes. This reduces the amount of air in solution and thus the likelihood of the free electrons recombining

during irradiation. Nitrogen (N_2) was used for all experiments at SCAPA, and it was carried out by removing the lids of the cuvettes containing the solution, and bubbling through a hypodermic needle for the desired length of time, after which the lid was placed back on, ready for irradiation.

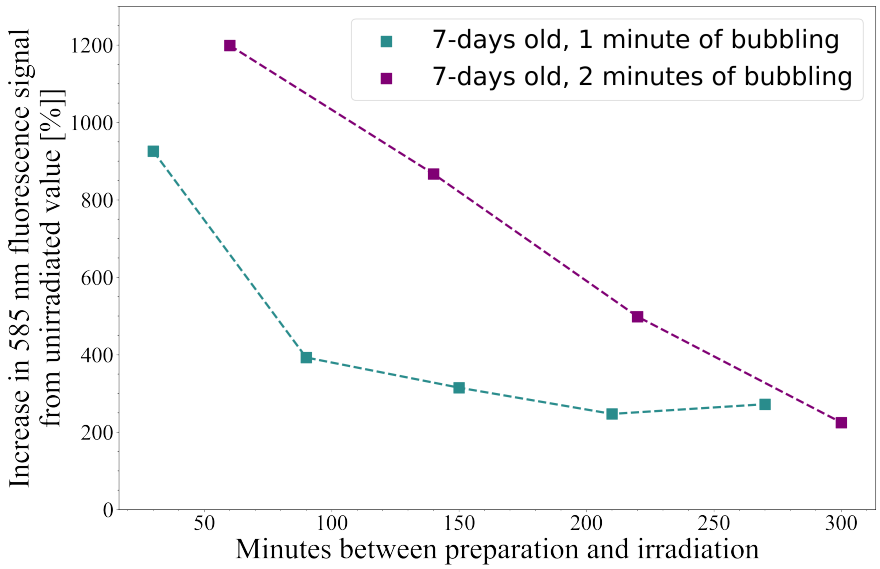

Figure 4.3: The increase in 585 nm fluorescence signal for 7-day old solution, which has been bubbled for either 1 or 2 minutes, then irradiated for 5 minutes by an X-ray source (corresponding to a dose of 5.38 Gy).

It was found that the length of time spent bubbling had a significant effect on the amount of fluorescence produced for a given dose. Figure 4.3 shows this, and highlights the fact that waiting longer between bubbling and irradiating significantly reduces the fluorescence signal strength for the same dose. This suggests that samples which are irradiated at the same time would be the ideal procedure.

Figure 4.4, shows several samples of solution made on the same day, irradiated with the same dose (5.38 Gy), for different N_2-bubbling times. The pattern with de-aeration time is also seen here.

4.2.2 Age of the solution

Another factor that affects the solution's response to dose, is its age. This was touched upon in the previous section, as the fluorescence intensity for a given dose decreased

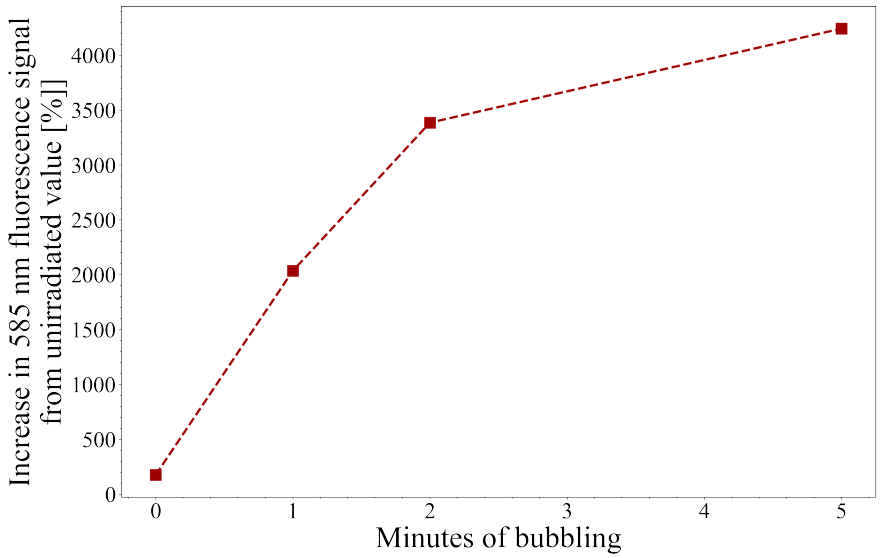

Figure 4.4: Increase in 585 nm fluorescence signal for a < 1 day old solution with different samples for different bubbling times. This suggests that N_2-bubbling for longer can drastically affect the measured fluorescence for a given dose. All solutions received the same dose of 5.38 Gy.

as the time between bubbling and irradiation lengthened. But the overall age of the solution (i.e. time since it was initially prepared) could also affect the resulting fluorescence intensity. This was tested by irradiating samples with the same X-ray tube parameters on two different days.

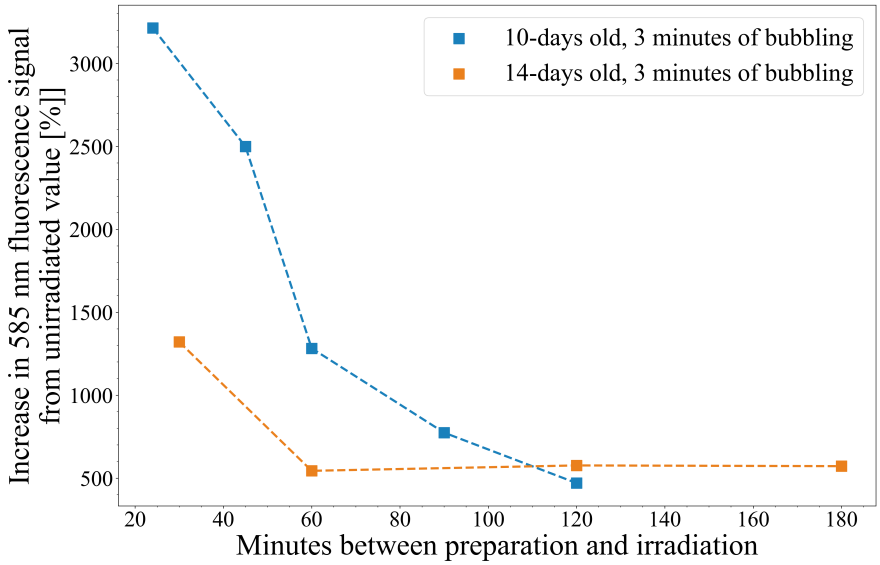

Figure 4.5: The increase in 585 nm fluorescence signal for a 10-day-old solution vs a 14-day-old solution, each receiving 5.38 Gy dose of X-rays at SCAPA

Figure 4.5 shows that the first 1-2 hours after N_2-bubbling can give a significantly different increase in fluorescence for a 10 day-old solution compared with a 14-day-old solution irradiated with the same dose. This suggests that using a fresh solution would yield the optimum signal-to-noise ratio.

The figures presented here highlight the time-sensitive nature of the resazurin solution, which must be taken into consideration if being used for accurate dosimetry.

4.3 Irradiation with gamma rays

I was fortunate to spend 5 months at the CEA Paris-Saclay in France, as part of my PhD, working with the Laboratory of Interactions, Dynamics, and Lasers (LIDYL) group. This enabled close collaboration with chemists who could contribute to improving the methodology of the chemical dosimeter. It also provided an opportunity to test the dosimeter with a gamma source to compare its response with that of electrons. Irradiation with laser-wakefield accelerated electrons was also planned at the CEA, but was not achievable in the time available.

However, several steps of the preparation method were tested, and their effect on the final change in resorufin fluorescence studied. These included the bubbling time, the initial concentration of resazurin and the age of the resazurin solution. Additionally, two spectroscopy methods were compared: (i) a compact set-up that used a 530 nm excitation LED, with fluorescence collected at right angles to the beam irradiation direction by an optical fibre that is connected to a Flame UV-vis mini spectrometer; and (ii) a tabletop Fluorolog FL3-22 spectrometer, belonging to the LIDYL group at the CEA. These two set-ups are shown in Figures 4.6 and 4.7, respectively, where it is clear that the first set-up (i, Figure 4.6) is much simpler, yet yields similar results (see Chapter 4.3.5).

To complement the fluorescence spectrum measurements, absorbance of the solutions after irradiation was measured and compared with the delivered dose. A Shimadzu UV-2600 spectrophotometer was used for these measurements. A baseline measurement was undertaken using a sample of ultra-pure water, then clean cuvettes were filled with solution and measured across the wavelength range 350 - 800 nm. A second cuvette

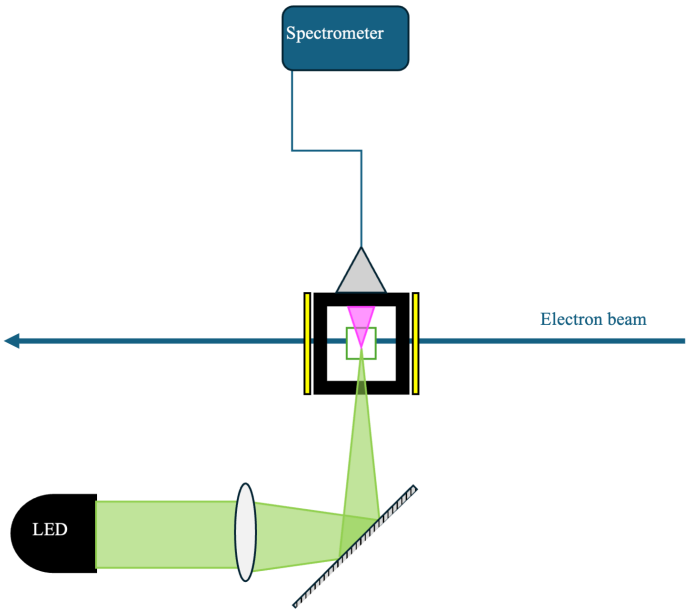

Figure 4.6: Schematic of the compact dosimeter set-up for fluorescence spectroscopy at CEA, based on a Flame UV-vis mini spectrometer (model: FLAME-T-XR1-ES). The excitation light is shown in green and the emitted fluorescence in pink.

of buffered water solution was used as the reference and remained in position during all sample measurements. As absorption is a fundamental property of a solution, these measurements enhanced the confidence in the fluorescence data, which is much more sensitive, and enabled a deeper understanding of the solution's absorption and fluorescence spectra.

4.3.1 Experimental method

A stock of phosphate buffer was prepared using ultra-pure water, sodium phosphate monobasic and sodium phosphate dibasic, with a pH of 6.8. Then, 0.9563 mL of tert-butyl alcohol (concentration, 10^{-3} M) was added, and the solution mixed until no solids remained. 5 mg of Sigma-Aldrich resazurin sodium salt (229.191 g/mol) was added to give a concentration of 19.9 μM, and the solution was then stirred again for at least one hour. 10 mL of solution was transferred to glass vials, sealed with rubber stoppers and the solutions bubbled with argon before irradiation. Bubbling with inert gas, such as argon, removes oxygen from the solution, which would otherwise recombine with hydrated electrons produced during the radiolysis process. Similarly, tert-butyl

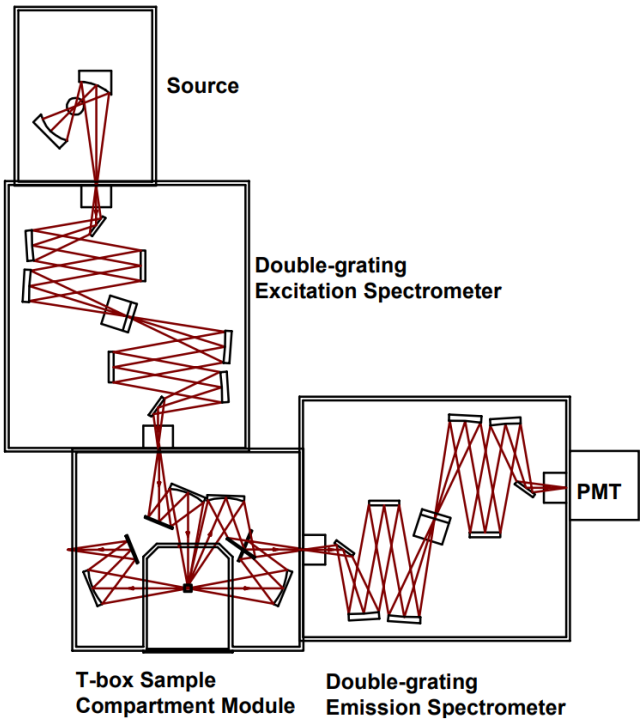

Figure 4.7: Schematic of the Fluorolog®-3 Model FL3-22 spectrometer used for fluorescence spectroscopy at the CEA. The cuvette of solution is placed in the T-box Sample Compartment Module for analysis.

is added to scavenge OH radicals, which would otherwise recombine with hydrated electrons produced during irradiation. Together, these increase the scavenging potential of the resazurin, which combines with hydrated electrons to form resorufin. The rubber stoppers allowed for a more efficient bubbling method, as shown in Figure 4.8, and this was found to greatly improve the results. Furthermore, argon was used during the CEA experiments rather than nitrogen. While both gases are inert and appropriate for the de-aeration of the solution, argon is more dense than nitrogen. Argon is therefore less likely to disperse after purging. When the purpose of the purging is to prevent air from re-entering the solution, this is a very desirable quality.

Gamma irradiation was performed with a Gammacell 1000 unit (Best Theratronics, Ottawa, Canada) (see Figures 4.9 and 4.10), which houses a 21.3 TBq caesium-137 source, and emits γ-rays of energy 662 keV [137] at a constant dose rate of 6 cGy/s [138]. The glass vials used were necessary due to the dimensions of the sample holder in

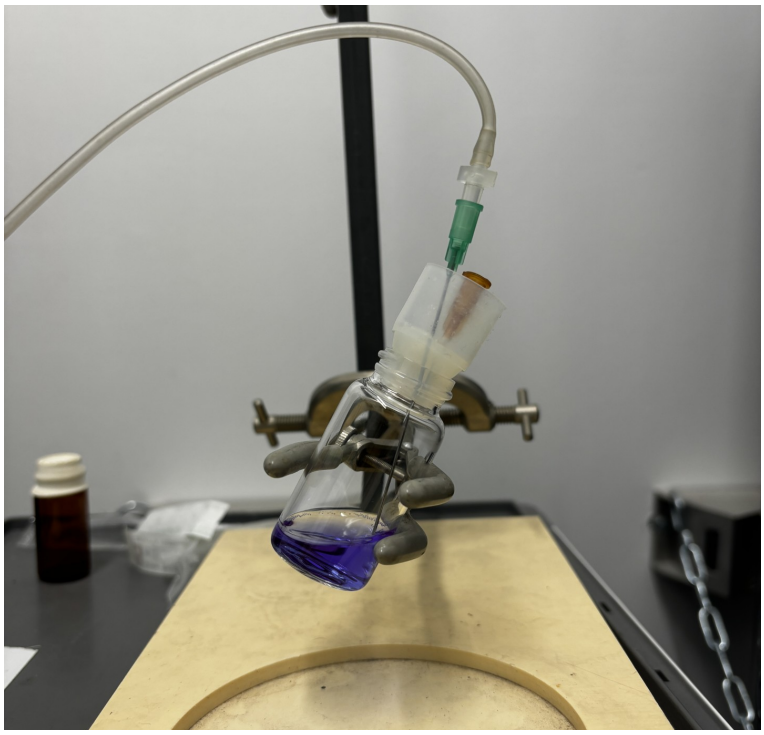

Figure 4.8: Bubbling procedure for the resazurin solution. The rubber seal ensures the container is airtight, a hypodermic needle bubbles the solution with argon, while another allows the argon to escape.

the Gammacell target area. Each sample was then transferred to quartz cuvettes for spectral measurements post-irradiation.

After irradiation was complete, the solutions were transferred into quartz cuvettes that had been cleaned with ultra-pure water, then rinsed with a small amount of the irradiated solution. The absorbance and fluorescence spectra were measured and relevant data extracted and plotted against dose delivered.

4.3.2 Varying the bubbling time

Figure 4.8 shows the bubbling procedure used for all irradiated samples at CEA. Unlike the procedure at SCAPA and CLEAR, the solution is in a sealed container. One hypodermic needle bubbles the solution with the inert gas (argon) while another allows the argon to escape. This reduces the likelihood of air re-entering the solution, thus improving the efficacy of the de-aeration process.

The time spent bubbling the solution was varied from 2 minutes to 15 minutes,

Figure 4.9: Best Theratronics Gammacell 1000 used for gamma irradiation at the CEA. A 21.3 TBq caesium-137 source irradiates solutions with 662 keV γ-rays at a constant dose rate of 6 cGy/s. The machine control panel displays the maximum and minium dose values for each irradiation.

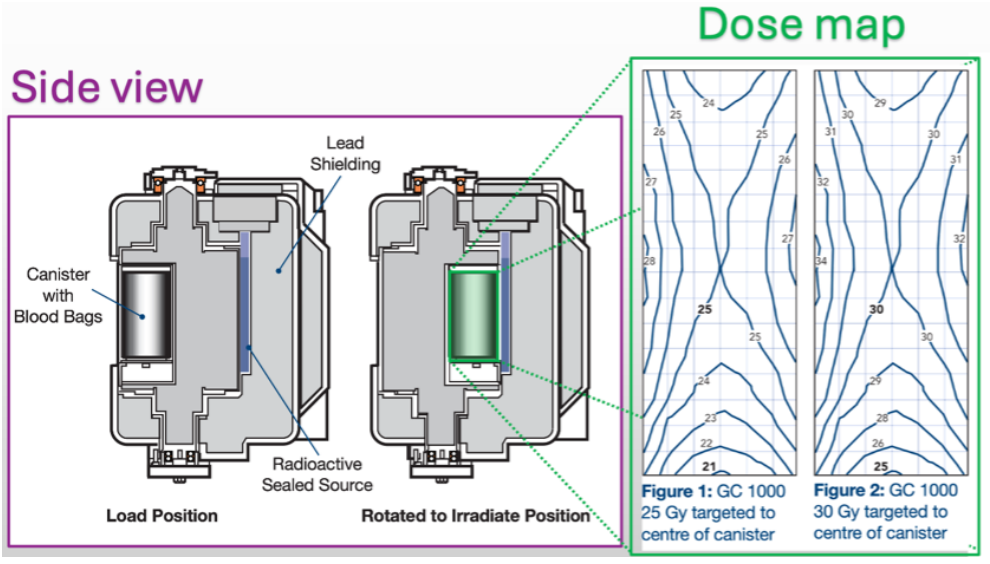

Figure 4.10: Side view and dose map of the Gammacell target area, showing the high dose uniformity of the source [138].

then all samples were irradiated with the same dose (16.45 Gy) of gamma rays. Figure 4.11 shows the increased change in 585 nm fluorescence signal for a longer bubbling time - which agrees with the X-ray irradiation data in Chapter 4.2.1. The previous study with X-rays showed that the change in signal appeared to plateau after around 5 minutes of bubbling, whereas in this study no plateau is evident even after 15 minutes. The reason for this is that for the X-ray study, only 2.5 mL of solution was bubbled, whereas here 10 mL of solution was de-aerated. This increased volume suggests that it may take longer for the solution to reach an optimal level of de-aeration. The vials were also sealed, which resulted in a much slower re-aeration rate, enabling a much higher level of de-aeration. However, bubbling longer than 15 minutes to reach this level would lead to extremely time-consuming experiments. The bubbling time used for the remainder of the γ-ray studies was 5 minutes.

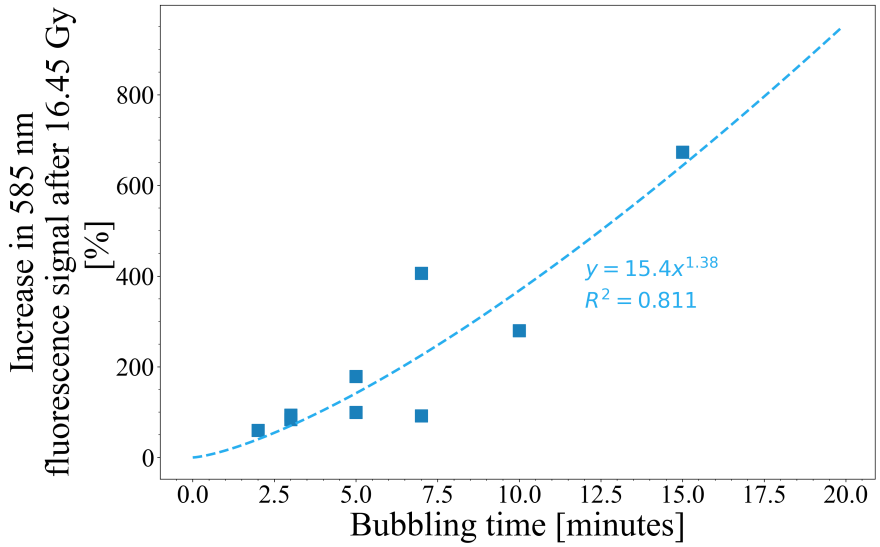

Figure 4.11: The effect of increasing the argon bubbling time of resazurin samples compared with the increase in 585 nm fluorescence, for 16.45 Gy of gamma radiation. The resazurin concentration is 19.9 μM and the pH is 6.8

4.3.3 Age of the solution

Similar to the data obtained with X-rays at SCAPA, the data collected at the CEA shows that irradiating a fresher solution gives a much larger increase in 585 nm fluorescence signal for a given dose. It should be noted that due to the two different beam

modalities, the two different bubbling procedures and the two different volumes of solution, they cannot be directly compared quantitatively. Two solutions were irradiated: one prepared 2 days before irradiation, and another that prepared on the same day as irradiation. Figure 4.12 shows that the fresh solution produces a larger signal increase for a given dose. For a dose of 18.35 Gy, there is an increase of 95% for the fresh solution versus 29% for the 2 day-old-solution – a factor of 3.3 difference. Similarly for a dose of 36.7 Gy, there is an increase of 678% for the fresh solution versus 307% for the 2 day-old solution – a factor of 2.2 difference. This suggests that the difference in response diminishes at higher doses, but in the clinically relevant range of up to around 40 Gy, it is significant.

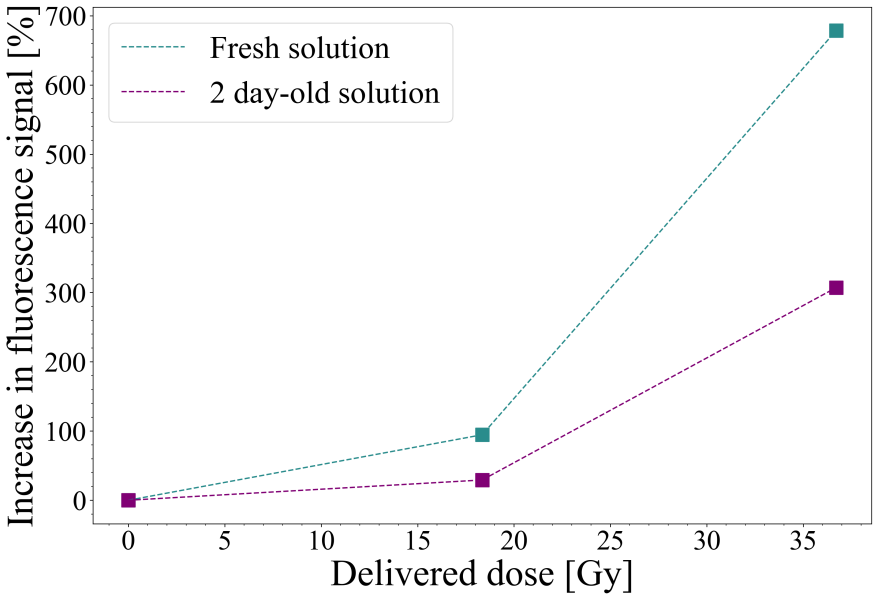

Figure 4.12: Increase in 585 nm fluorescence signal for a 2-day-old solution compared with a solution made on the same day as irradiation with the gamma source at the CEA. Both were irradiated twice, and the zero value is the fluorescence of a non-irradiated sample.

4.3.4 Varying the resazurin concentration

For a chemical dosimeter such as that discussed here, it is vital that the procedure and chemical make-up of the solution is identical and replicable with every use. To explore the significance of this, two solutions of different initial resazurin concentrations were irradiated with several doses. One solution had a concentration of 19.9 μM (the con-

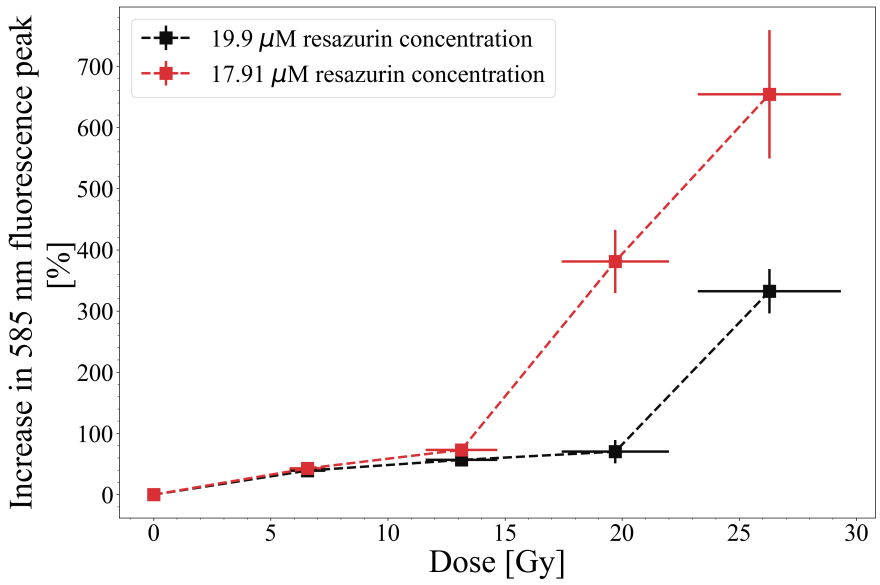

Figure 4.13: Samples with different initial concentrations of resazurin irradiated with doses from 6 Gy to 26 Gy. Half the samples had a concentration of 19.9μM (the concentration used throughout all previous studies) and the other half a concentration of 17.91μM - a decrease of 10%

centration used in all other experiments) and the other solution had a concentration of 17.91 μM - a decrease of 10%. Figure 4.13 shows the difference in detected fluorescence between the two. As the results show, having a lower concentration of resazurin can result in an increased fluorescent signal amplitude of over 100% at 26 Gy, highlighting the importance of the consistency of the chemical make-up of the solution. The two solutions were treated in exactly the same way, which includes identical de-aeration times. As outlined in Chapter 2.5, the resazurin scavenges hydrated electrons, which can also be scavenged by residual oxygen in the solution after de-aeration. The solubility of dissolved O_2 at 25°C and at atmospheric pressure is around 1.22 mM [139], around 60 times larger than the concentration of resazurin. Therefore, the solution is very sensitive to the amount of dissolved oxygen present in the system. It is unlikely that such an increase in fluorescence is due solely to this. However, a contributing factor could be the absorbance of emitted 585 nm photons by the solution itself, as shown in Figure 4.14. The solution with a lower concentration of resazurin has a lower initial absorbance, and the ratio between the two solutions increases slightly as the dose increases, where the absorbance changes from 1.08 to 1.2. This factor, combined

with the high sensitivity of the solution to oxygen content, could be the origin of the difference in the observed fluorescence spectra.

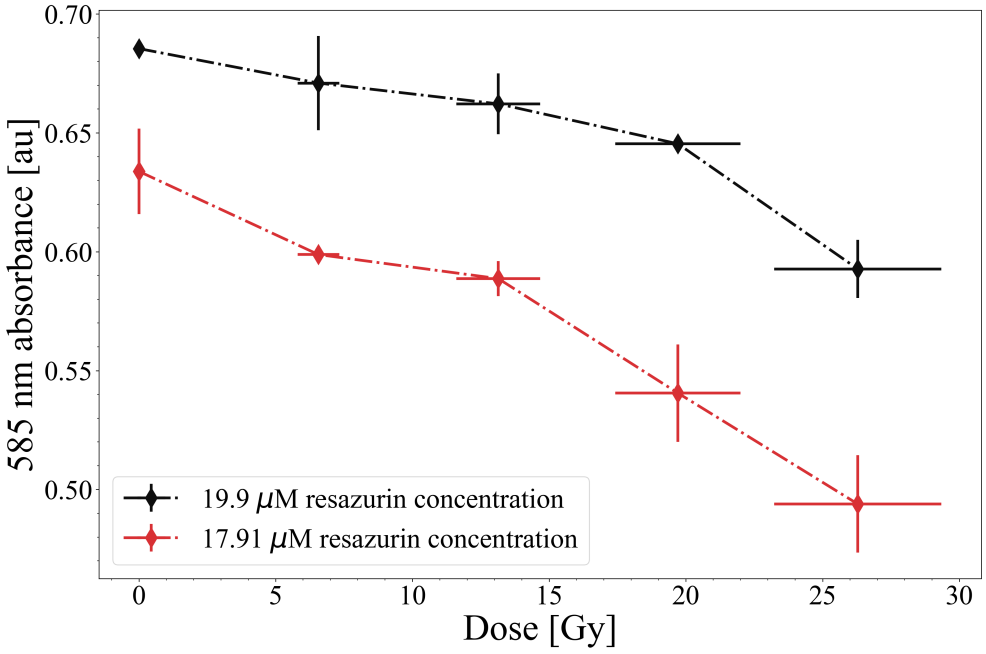

Figure 4.14: Absorbance of emitted 585 nm fluorescence of the solution with increasing dose. The decrease in concentration of resazurin leads to lower absorption of the emitted 585 nm photons, and therefore increased detected fluorescence.

4.3.5 Comparison of spectrometry methods

Our set-up is compact, portable, and inexpensive, due to the affordable mini spectrometer, optical fibres and basic optical equipment. It was, therefore, important to establish how the spectrometer compared with a larger spectrometer, such as the Fluorolog. Samples of resazurin solution were irradiated with gamma rays, as before, for a range of doses, and the spectra measured using both spectrometers. Figure 4.15 shows a comparison of the two, with the increase in 585 nm fluorescence signal plotted against dose. Table 4.1 compares different parameters of each method.

Our LED-based set-up is considerably more compact, inexpensive and faster, yet yields similar results to the Fluorolog system, with the difference in signal levels decreasing as the dose increases. This is most likely due to the increased signal-to-noise ratio (SNR) at higher doses for both methods. A maximum difference of 18.2% be-

	Fluorolog®-3 FL3-22	FLAME-T-XR1-ES
Integration time range	1 ms – 160 s	3.8 ms – 10 s
Integration time used here [ms]	500	340
Spectral range measured [nm]	535 – 700	200 – 1025
Optical resolution [nm]	0.2	1.7
Excitation source	450 W Xe lamp	1 W 530 nm LED
Grating blaze wavelength [nm]	330 & 500	250
Grating groove density [mm^{-1}]	1200	500
Slit width [nm]	3 (excitation & emission)	25 μm

Table 4.1: Parameter comparisons for the tabletop Fluorolog spectrometer used at the CEA and our compact LED-based spectrometer set-up.

tween the two was measured at a dose of 3.3 Gy. They both follow identical curves, which suggests they respond similarly, and the simpler and faster spectrometry set-up is sufficiently reliable.

4.3.6 Testing the robustness of the set-up

Having confidence in the compact spectrometer, it was also important to confirm that the entire spectrometry method was reliable. This was tested by adjusting various parts of the set-up and observing the effect they had on the LED signal of the compact spectrometer.

The first characteristic tested was the stability of the LED. It is important to know how the fluorescence spectrum varies in the time when the LED is on.

Figure 4.16 shows that on three of the four days of testing, the LED takes $\approx$ 45 minutes to reach a stable intensity level. It is therefore prudent to wait at least 45 minutes for the LED to warm up to reach a stable level before acquiring fluorescence spectra. While the value at time = 0 is only around 4% smaller than the stable level, this can become more significant when combined with additional sources of error.

In the preliminary CLEAR experimental run (see Chapter 3) the LED was kept off in between measurements to avoid overheating, and only switched on during measurements. The data here demonstrates that this may have introduced errors, and that leaving the LED on would likely lead to more consistent measurements. This will be employed in future studies.

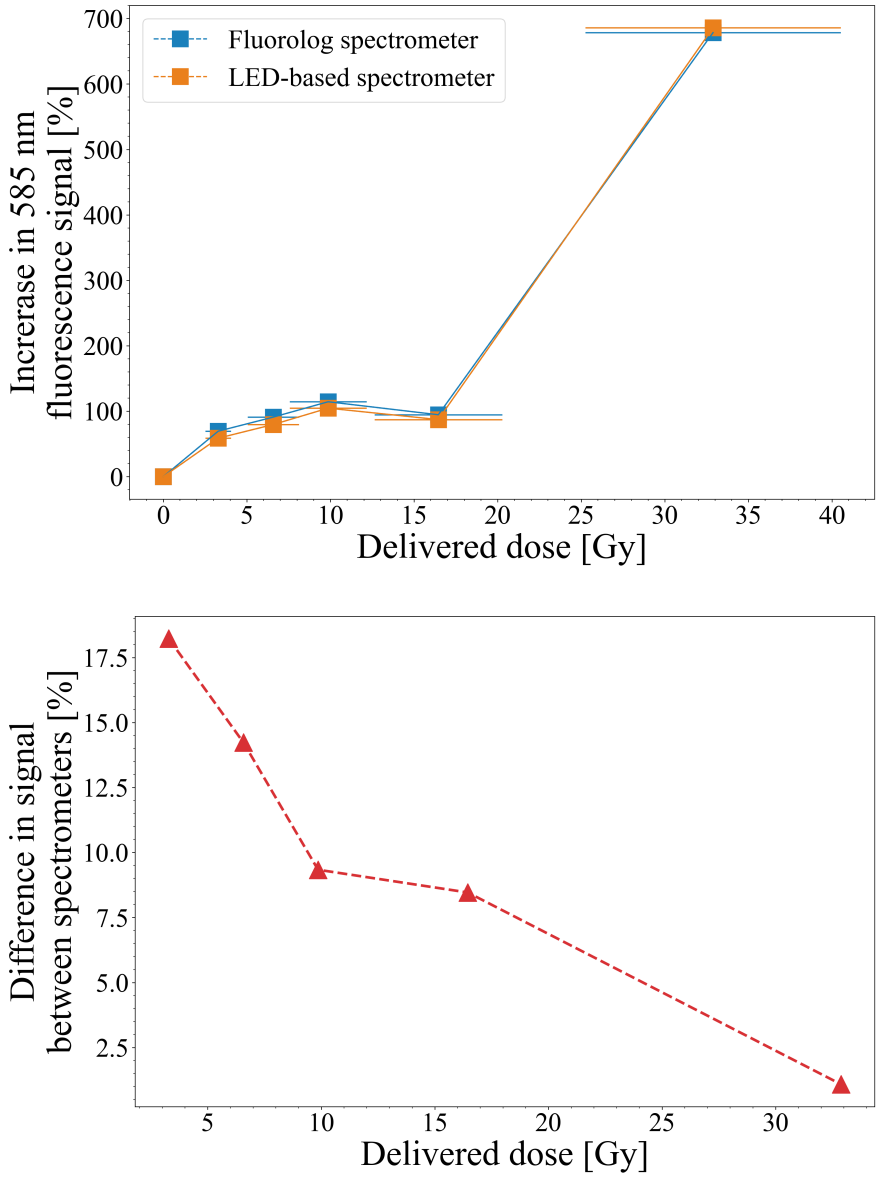

Figure 4.15: Comparison of the table-top Fluorolog spectrometer and the Flame UV-Vis mini spectrometer showing (top) the increase in 585 nm fluorescence signal, and (bottom) the absolute difference between the two methods up to ≈ 30 Gy.

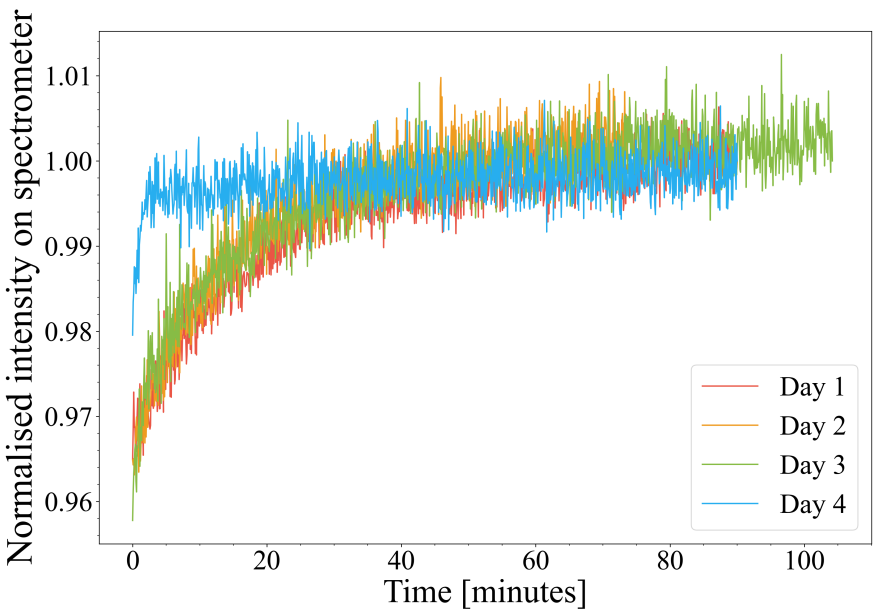

Figure 4.16: The intensity of the central wavelength of the LED (535 nm) measured by the Flame UV-vis spectrometer as a function of time, from being switched on. This was measured over 4 separate days, and signals were normalised to the final measured intensity of each set of data.

Additional aspects of the experimental procedure investigated were the physical set-up of the dosimeter, and its associated components. For example, it was found that removing the collimating lens, which was placed immediately after the LED and before the optical fibre that transports the excitation light to the cuvette holder, can increase the amount of light at the cuvette position by as much as 66%, as shown in Figure 4.17a. While this could improve the precision in detecting the change in fluorescence measured, it would not make a difference to the accuracy of the measurements, or contribute to any significant sources of error. Sufficient emitted fluorescent light will enter the spectrometer regardless. The user will, however, have to consider any potential systematic errors, such as an offset in the spectral measurements, and random errors related to the fluctuations in the spectra. These can be mitigated by performing calibrations with spectral lamps, and taking multiple readings, respectively.

The optical fibre that transports the emitted fluorescence to the spectrometer for analysis can have an impact on the signal strength. The fibre was handled and bent slightly while measurements were taken, and the resulting fluctuations in the measured signal are shown in Figure 4.17b, which show that the transmitted 585 nm light intensity

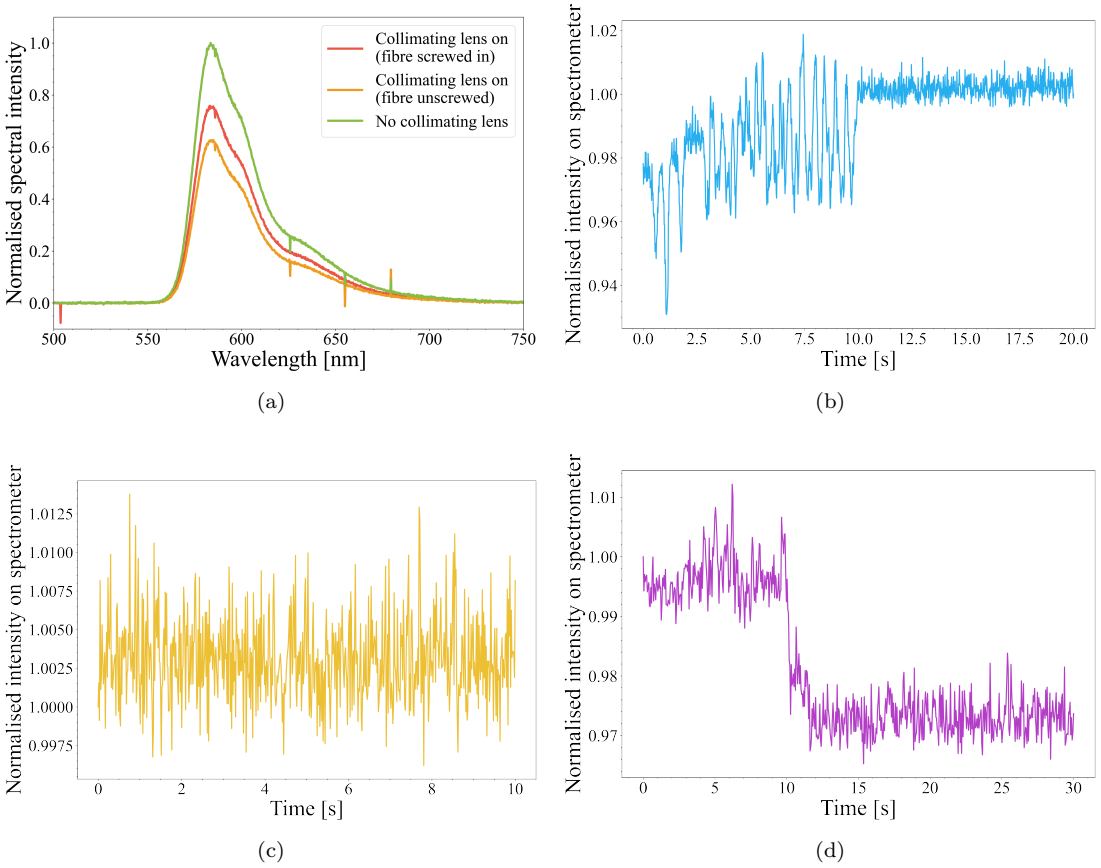

Figure 4.17: Testing sensitivity of the LED-based spectrometer to (a) removing the collimating lens between the LED source and the optical fibre transporting it to the cuvette holder, (b) movement and bending of the optical fibre between the cuvette and the spectrometer, (c) moving the filter holder between the cuvette and optical fibre, and (d) having the filter fall out of position within its holder. All spectral intensity values measured in (b-d) are at the resorufin emission wavelength of 585 nm.

was reduced by as much as 6%.

Figure 4.17c shows that moving the 550 nm long-pass filter holder does not change the transmitted signal strength significantly. However, from Figure 4.17d, the signal can be seen to drop by around 3% if the filter comes loose, and no longer sits normal to the incident light. In CLEAR experiments (and in experiments where the dosimeter is at the end of a beamline) the set-up is not readily accessible due to the radiation safety restrictions. It is therefore important to ensure that the components of the set-up are correctly placed and will remain stable.

As previously discussed, while individual signal reductions are quite small, and could be considered negligible, together they can contribute to reductions in signal strength by as much as 12.5%. This can be even more significant if the set-up isn't optimised and the light reaching the cuvette is diminished, as shown in Figure 4.17a. This has potential to reduce the transmitted light intensity by almost 50%. Consistency is essential for these sensitive chemical dosimeters and it is therefore important to be aware of all sources of error, and to optimise the measurements and keep them consistent.

4.3.7 Dose response of the fluorescence dosimeter

Resazurin dosimeter solution was irradiated at the CEA with a range of doses, multiple times, to establish a dose calibration curve, similar to those used for Gafchromic film (see Figures 3.7), which could, potentially, be used in future studies. One simply measures the increase in the resorufin fluorescence and converts this to a dose in real time. Before producing this plot, however, it is necessary to investigate the response of the fluorescence dosimeter as a function of dose delivered, to better understand the mechanisms at play.

In Figures 4.18 - 4.20, the change in the 585 nm fluorescence intensity is plotted against the dose delivered by the gamma source. It is clear from the results that there are three distinct segments of the curve.

The first segment, for lower doses, up to ≈ 12.5 Gy, where the fluorescence increases with dose non-linearly and follows a power law: $y = 23.34x^{0.57}$, with an R^2 value of 0.892.

Beyond 12.5 Gy, the fluorescence increase follows a linear curve: $29.97x - 340.62$, with $R^2 = 0.96$, up to around 65 Gy.

Beyond this dose value, the fluorescence decays logarithmically with dose: $5936 - 1056\ln(x)$, with $R^2 = 0.92$, eventually reaching a point where no fluorescence is emitted.

The reason for these three response regions can be explained. For example, in the first, low dose region, the fluorescence likely increases at a slower rate due to the presence of contaminating reducing agents, such as oxygen, in the solution. These decrease the electron scavenging potential of the resazurin, thus decreasing the amount of fluorescent resorufin produced. This description is analogous to the explanation why Fricke solution is often given a pre-irradiation value of 10 Gy prior to being used as a dosimeter [140, 141], after which it responds linearly to dose, similar to the resazurin dosimeter. A notable difference is that Fricke solution has a non-linear response below 1 Gy, whereas the resazurin solution response is non-linear below around 12.5 Gy - suggesting a larger effect arising from contaminants. This is also why the Fricke solution used to calibrate the X-ray source in Chapter 4.1 was not pre-irradiated, as the dose range we were interested in was much higher than 1 Gy, therefore the effect from contaminants was considered negligible.

The second, linear section between 12.5 Gy and 65 Gy, is the simplest to explain: it is due to the reduction of resazurin into the fluorescent chemical resorufin, the magnitude of which is proportional to the dose delivered.

The final portion of the curve, where the emitted fluorescence begins to decay, is due to the resorufin being reduced further to hydroresorufin ($C_{12}H_8NO_3$), a colourless, non-fluorescent molecule [142, 143]. Usarski et. al [143] used resazurin for cell proliferation studies, and found that reducing the cell incubation time would avoid the occurrence of this additional reduction reaction. For the resazurin dosimeter, the delivered dose is analogous to the incubation time, therefore keeping the dose below the threshold measured here ($\approx$ 65 Gy to the entire solution) would be essential for having reliable readings. One could also adjust the resazurin concentration, but this would then affect the reduction reaction rate, which is proportional to concentration given by Equation 2.29, and also increase the optical absorption of the sample, leading to less accurate

measurements.

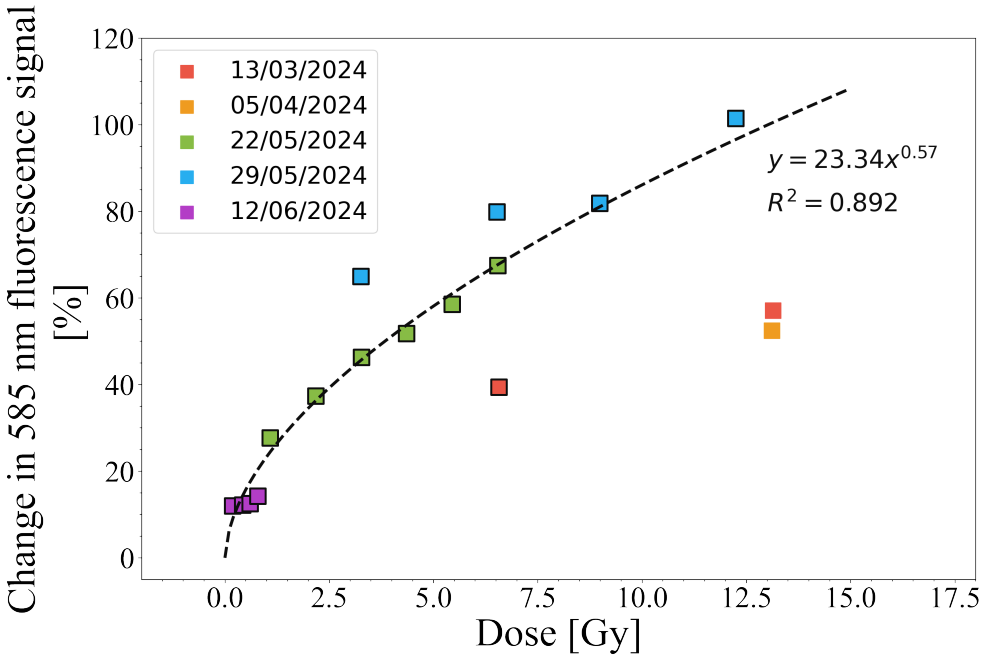

Figure 4.18: Increase in 585 nm fluorescence signal for gamma-irradiated samples at low doses, over a range of days at the CEA.

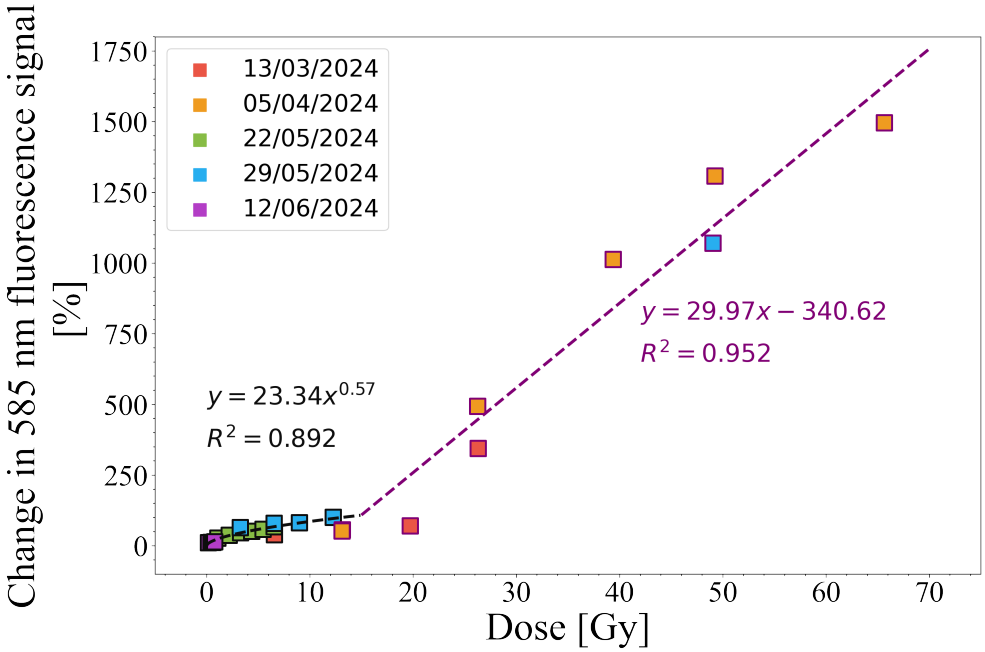

Figure 4.19: Increase in 585 nm fluorescence signal for gamma-irradiated samples at low-medium doses, over a range of days, at the CEA.

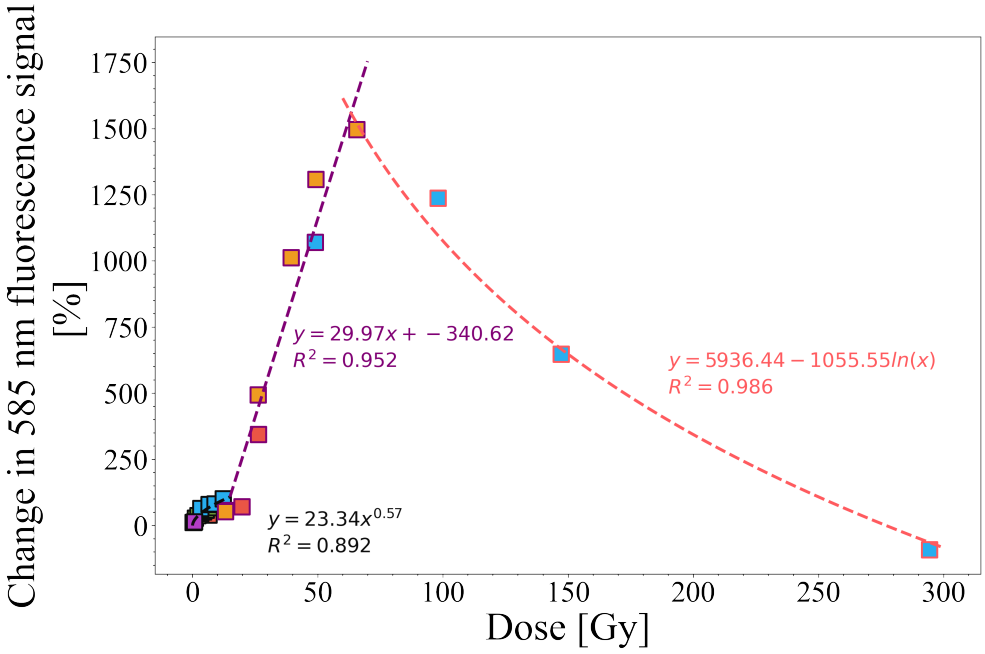

Figure 4.20: Increase in 585 nm fluorescence signal for gamma-irradiated samples at all dose values, over a range of days, at the CEA.

While these descriptions are more qualitative, one can also study the absorbance spectrum of the solution to obtain a clearer understanding of why the fluorescence might change non-linearly.

4.3.8 Absorbance measurements

To complement fluorescence spectrometry, absorbance measurements at the relevant wavelengths were also undertaken. These wavelengths were the excitation LED wavelength, 530 nm, and the resorufin fluorescence emission wavelength, 585 nm. By investigating the solution absorbance at these wavelengths, one can obtain a better understanding of why the fluorescence curves are non-linear. If the solution itself absorbs more or less LED light, it will directly affect the emitted fluorescence. Similarly, if the solution absorbs more or less of the emitted fluorescence, it will also influence the shape of the observed spectra.

The absorbance has two or three distinct regions that exhibit different behaviour. Figure 4.21 shows the change in absorbance of resorufin produced at low doses – up to

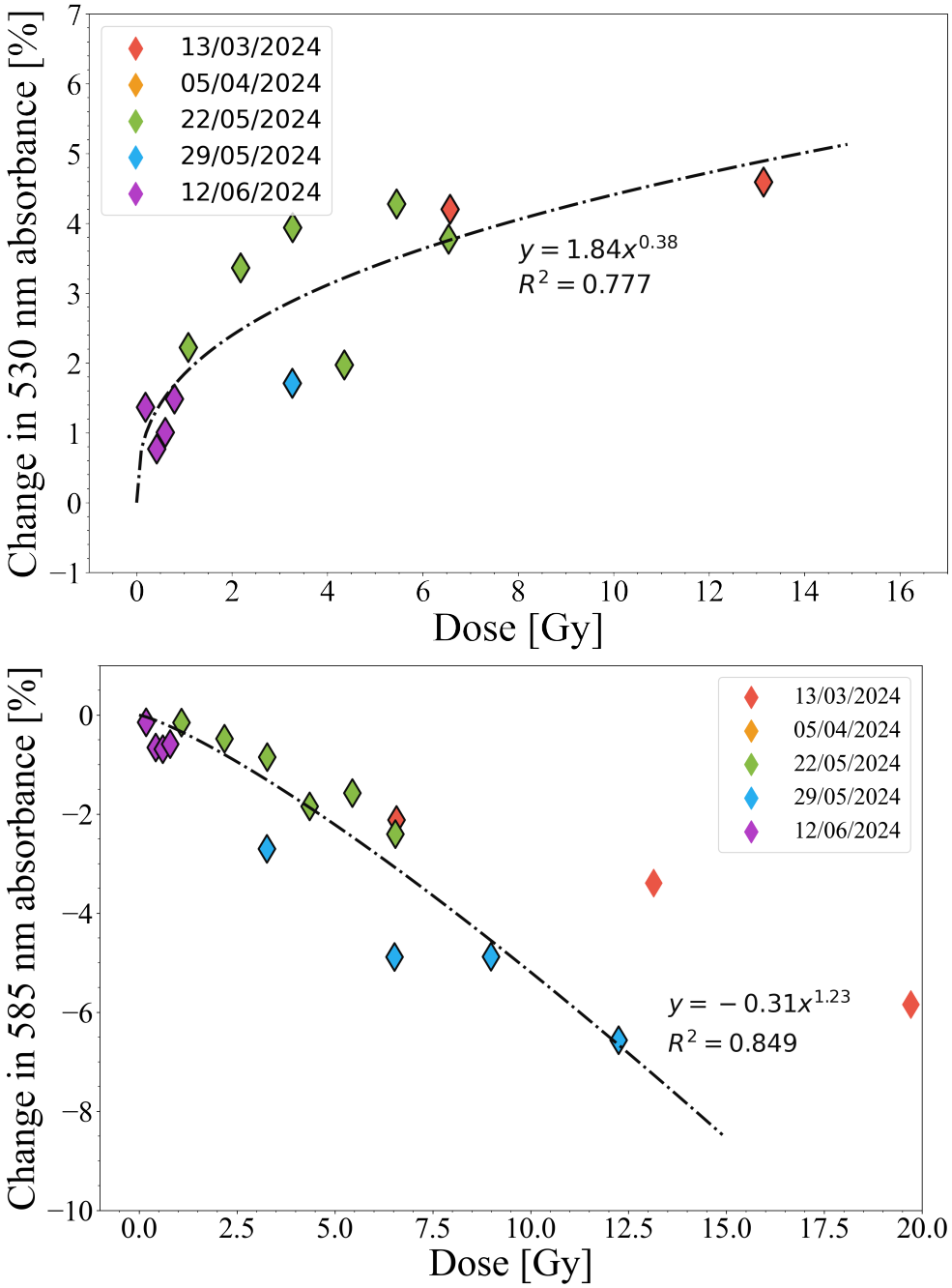

Figure 4.21: The change in absorbance at (top) the fluorescence excitation wavelength, 530 nm, and (bottom) the fluorescence emission wavelength, 585 nm, for doses < 12.5 Gy.

around 12.5 Gy, at the excitation wavelength (530 nm) and the emission wavelength (585 nm). The 530 nm absorbance increases as a power law, $y = 1.84x^{0.38}$, in this region, and the 585 nm absorbance decreases as a power law, $y = -0.31x^{1.23}$, both of

which correspond to an increase in fluorescence, shown in Figure 4.18.

However, an interesting change occurs beyond this dose region as shown in Figure 4.22, when the 530 nm absorbance increases linearly with a larger gradient, and the 585 nm absorbance decreases substantially, following a consistent logarithmic trend for all remaining doses. This may explain why the fluorescence emitted at 585 nm increases rapidly beyond 12.5 Gy. Here, the solution absorbs more of the excitation photons and fewer of the emission photons. The net effect is a rapid increase in observed fluorescence. When the dose increases beyond 65 Gy, the 530 nm absorbance reduces logarithmically as a function of dose – due to the reservoir of resazurin being depleted – and the 585 nm absorbance continues to decrease logarithmically as the solution becomes clear and the active molecules are depleted (reduced to hydroresorufin).

4.3.9 Emulation of the conversion of resazurin

Another test carried out was to emulate the dilution of a solution of resazurin thus reducing its concentration, and replacing the "lost" resazurin with resorufin. This emulated the 1:1 exchange of resazurin for resorufin

$$RNO + e^-_{aq} \longrightarrow RN^{\cdot}O^-$$

$$2RN^{\cdot}O^- + 2H^+ \longrightarrow RN + RNO + H_2O.$$

Two 500 mL solutions were prepared: resazurin mixed with buffered water, and resorufin mixed with buffered water, both with concentrations of 19.9 μM. 3 mL of the resazurin solution was removed and spectrally analysed, then returned to the solution. 50 mL of the resorufin solution was then added and the solution was stirred. This decreased the resazurin concentration by 1.81 μM, corresponding to the increase in resorufin concentration. This was repeated until the two molecules had equal concentrations. This entire process was then repeated starting with 500 mL of resorufin solution, and gradually replacing it with resazurin until the concentrations were equal.

Figure 4.23a shows the change in absorbance for these "manually converted" solutions. A 602 nm peak is clearly present in pure resazurin. It has an initial value of 0.79

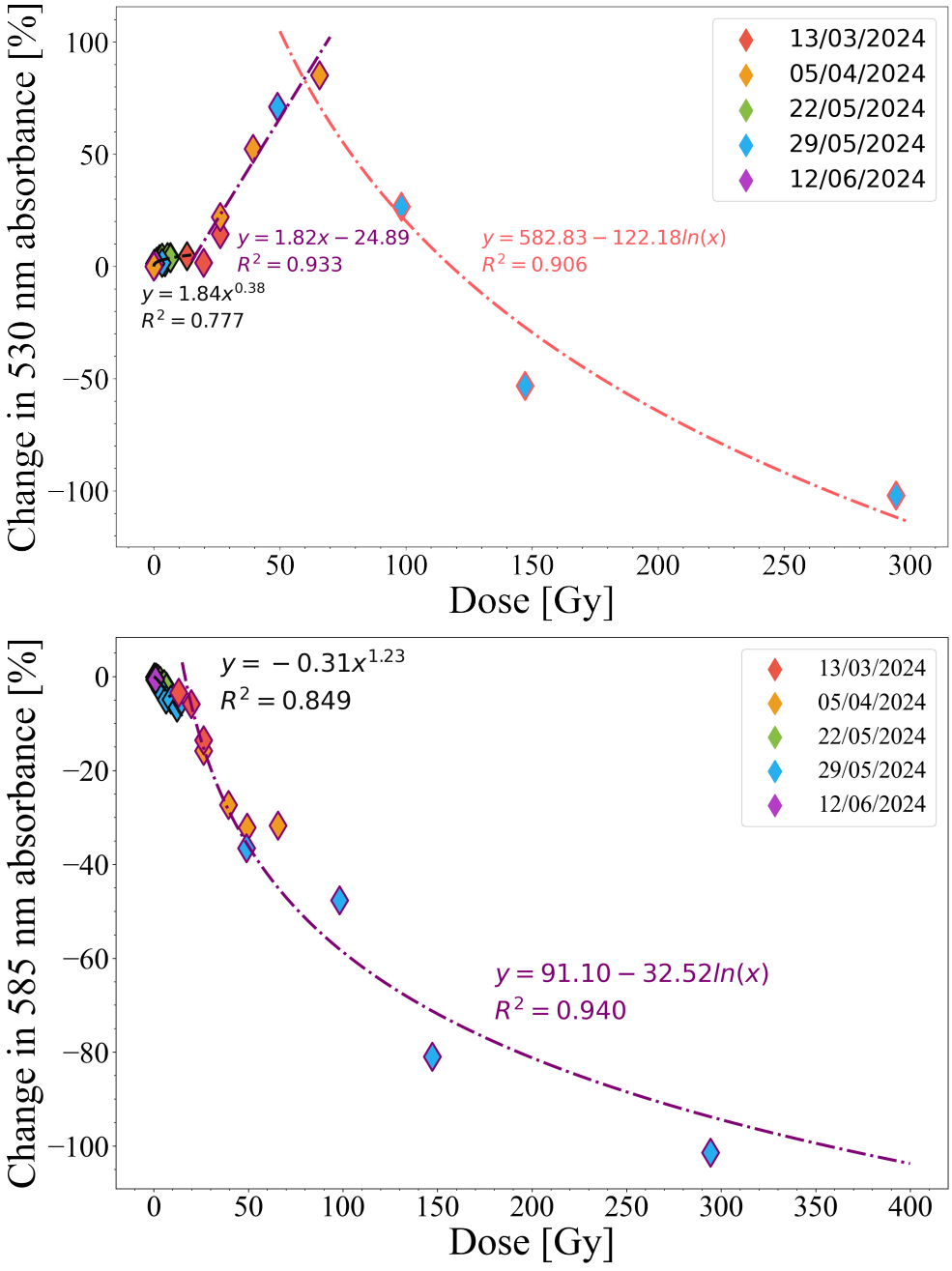

Figure 4.22: The change in absorbance at (top) the fluorescence excitation wavelength, 530 nm, and, (bottom) the fluorescence emission wavelength, 585 nm, for all doses.

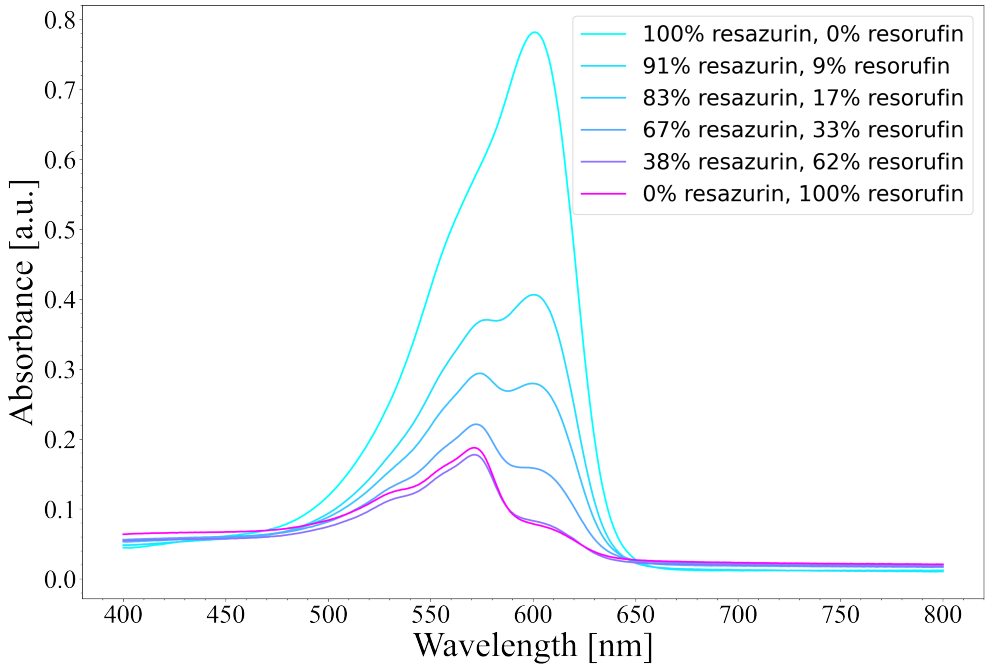

(a)

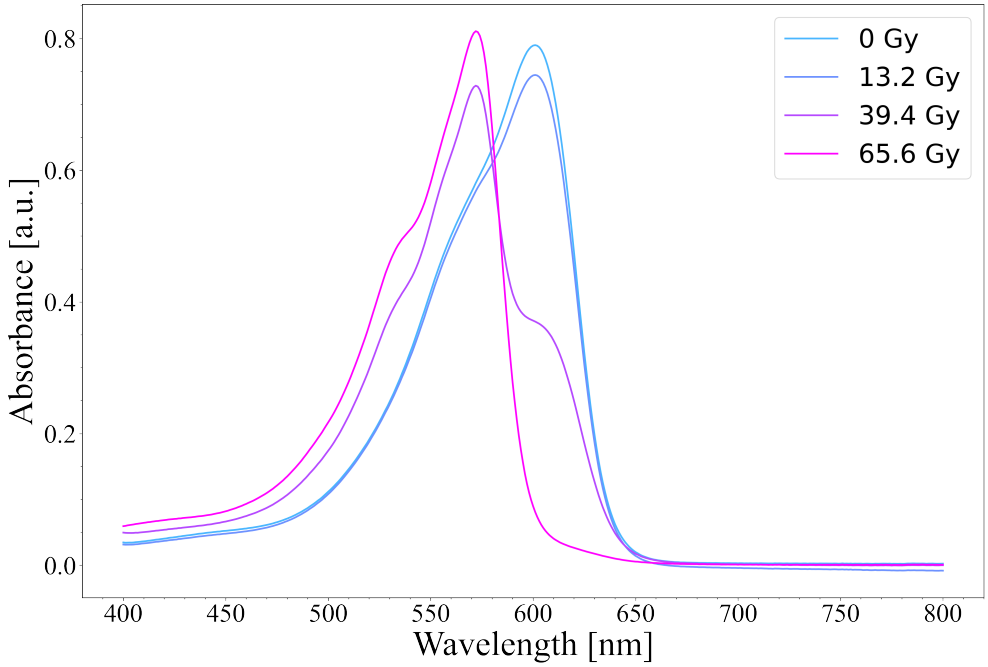

(b)

Figure 4.23: Absorbance spectra of (a) samples that have had the resazurin manually exchanged for resorufin, to emulate the reduction process, compared with (b) samples that have been irradiated with up to 65.6 Gy.

and decreases with the resazurin concentration. A secondary smaller peak appears at around 572 nm for the solution of pure resorufin, the absorbance of which is 0.19.

In contrast, another solution of the same concentration was irradiated with a range of doses up to 65.6 Gy (shown in Figure 4.23b). These spectra should be compared with the manually converted spectra. The initial peak at 602 nm is present, and has a value of 0.78, which decreases with dose as in 4.23a – supporting the hypothesis that this peak is caused by resazurin, which depletes as the solution is irradiated.

The second peak at 572 nm, however, is more prominent for irradiated solutions. Given the similarity of both initial spectra, it becomes evident that more processes are involved than simply a 1:1 conversion of resazurin to resorufin, the products of which absorb more in the 572 nm spectral region.

Considering the differential spectra shown in Figure 4.24, the mechanisms become clearer. When the solution is irradiated, there is an increase in the absorbance of 530 nm and 572 nm photons. This increase does not occur when the resazurin is converted to resorufin manually, and the cause of the increased absorbance at these wavelengths is not clear. However, it demonstrates that assuming that resorufin is the only product in an irradiated sample is over-simplistic. 530 nm is also the wavelength of the excitation LED used to induce fluorescence in the sample, and similar to that shown in Figure 4.22, it is likely that it leads to the sharp rise in the observed fluorescence beyond ≈12.5 Gy.

4.3.10 Dosimeter calibration curve

After numerous irradiations with gamma rays at the CEA, a final plot can be constructed to show what a calibration curve might look like for the resazurin dosimeter. Figure 4.25 shows the increase in 585 nm fluorescence intensity on the x-axis and dose on the y-axis.

A noticeable feature of the curve is the change in slope at ≈ 65 Gy, as the fluorescence decreases, due to the saturation of the solution. It would therefore be necessary, for gamma irradiation, to use doses below this value. As discussed in Chapter 5, this dose value is much lower for γ-ray irradiation than for the VHEE beams used at

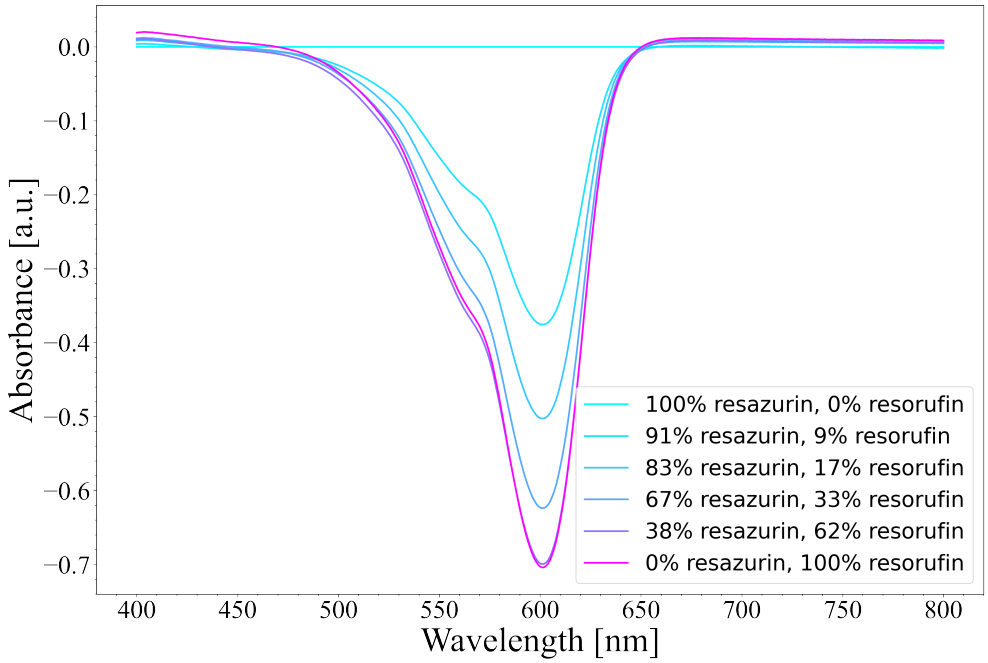

(a)

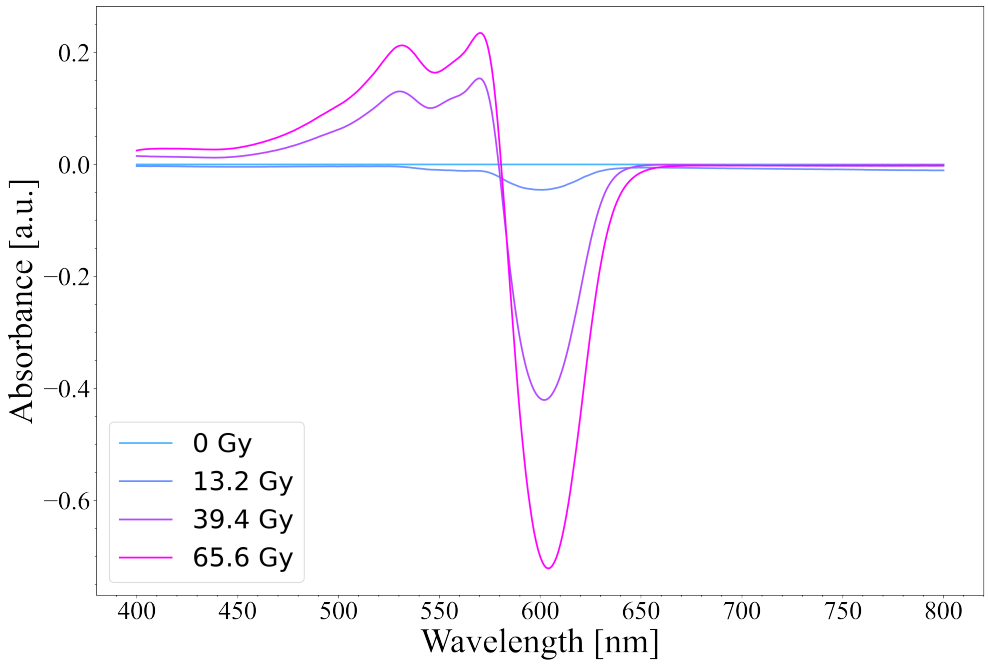

(b)

Figure 4.24: Differential absorbance spectra of (a) samples that have been irradiated with up to 65.6 Gy, and (b) samples that have had the resazurin manually exchanged for resorufin, emulating the reduction process.

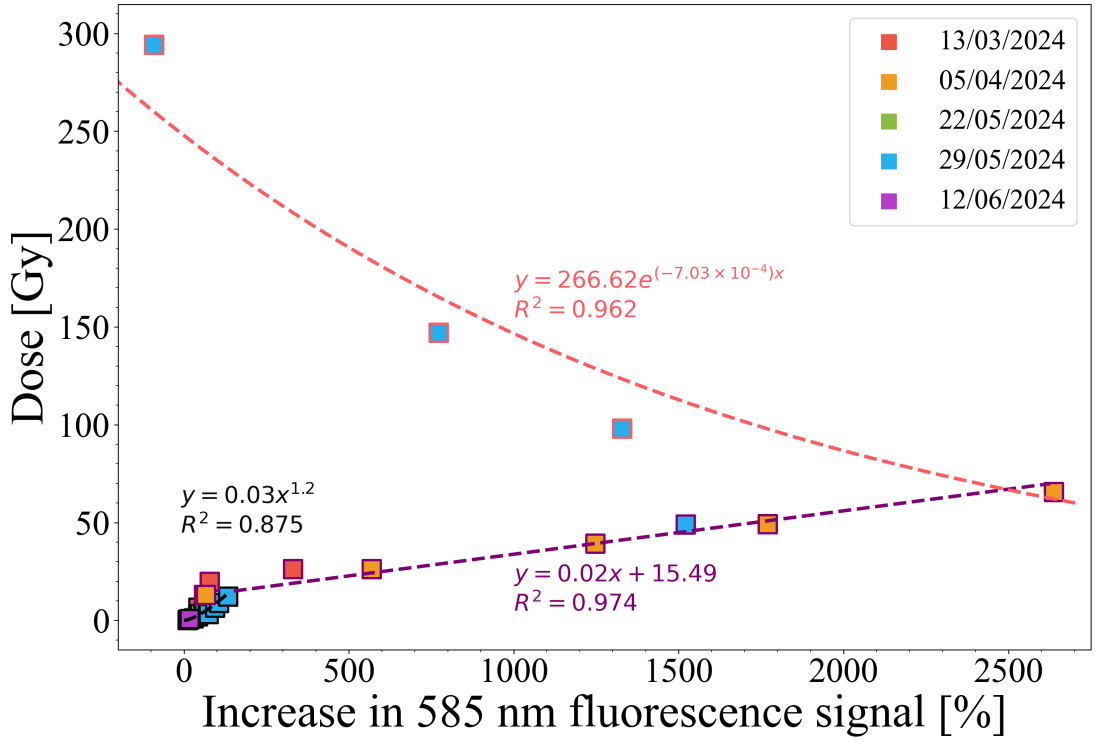

Figure 4.25: Calibration curve for the resazurin chemical dosimeter, irradiated with gamma rays. When using this dosimeter, it would be necessary to ensure that the dose delivered is below the 65 Gy dose saturation limit. This could be done during the calibration stage with another dosimetry method such as RCF, with later dose measurements being taken more quickly with the resazurin-based dosimeter.

CLEAR. The possible causes for this discrepancy are also discussed. While this 65 Gy dose limit may seem like a potential weakness, it is not necessarily the case. Typical radiotherapy treatments deliver $\approx$ 2 Gy per fraction, with hyper-fractionated radiotherapy delivering even less [144]. Therefore, for clinically relevant doses, the dosimeter would be very useful, given its speed, real-time use, accessibility and sensitivity – particularly at low doses.

4.4 Discussion

Following numerous tests at both SCAPA and the CEA, using X-rays and gamma rays, respectively, a deeper understanding of the resazurin-based dosimeter has been established. This, in turn, has led to a more robust procedure for optimising the dosimeter.

After calibration of the X-ray source at SCAPA, three aspects of the solution preparation were investigated: the time between preparation and irradiation, the duration of the de-aeration of the solution, and the age of the solution. The effect these had on the increase in fluorescence signal were compared, and are shown in Figures 4.3 – 4.5. The time delay between preparation and irradiation of the solution can significantly affect the observed increase in the fluorescence signal for a given dose – this suggests the solution should be irradiated as quickly as possible following the de-aeration process. The increase in fluorescence for a given dose (5.38 Gy) was found to strongly correlate with the de-aeration time, but may saturate after approximately five minutes. One may assume that bubbling for as long as possible maximises the SNR of the dosimeter, but when irradiating many samples, this would be extremely time-consuming, but could be decided by the user. The age of the solution also has an impact on the fluorescence signal change. It is therefore recommended to use freshly prepared solution where possible. This was done across all subsequent experiments. During the later experiments at the CEA (and then CLEAR), an improved bubbling procedure was employed, using two needles inserted into a sealed container (see Figure 4.8). This ensured that less air could re-enter the solution, therefore the effects of radical recombination became less significant. Another technique which could be employed is the use of micro-fluidics, which would ensure a constant flow of solution, keeping it fresh for as long as required. This would require careful planning and design.

During the experiments with γ-rays at the CEA, it was found that reducing the initial concentration of resazurin resulted in an increased fluorescence signal for a given dose (Figure 4.13). This was primarily due to the dosimeter sensitivity to oxygen in the solution, and the decreased absorbance of the 585 nm fluorescent photons. Our compact, low-cost method was compared to a dedicated table-top Fluorolog spectrometer, and the two were found to be in excellent agreement, even more so at higher doses (Figure 4.15), which implies that error at low doses is most likely due to an offset. Various physical aspects of the dosimeter set-up were investigated, including warming up of the excitation LED shown in Figure 4.16, where the collimating lens between the LED and the cuvette holder, the bending of the optical fibre transporting the emitted

fluorescence to the spectrometer, the filter between the cuvette and the fibre (Figure 4.17). These were found to have minor effects on the measured fluorescence signal individually, but when combined could diminish the signal by as much as 12.5 %. It is therefore advised that all physical components of the set-up be checked, and kept as consistent as possible while using the dosimeter. For example, the optical fibre could be secured in position to eliminate the risk of bending, and the positions of the optical filters and lenses could be checked regularly to maintain a high SNR.

Multiple irradiations of numerous samples were analysed to obtain a calibration curve for the dosimeter. Up to around 12.5 Gy, the fluorescence increased with dose, following a power law curve: $y = 23.3x^{0.57}$. This is may be due to impurities in the solution, in which case the solution should be pre-irradiated with a dose of at least 12.5 Gy, if doses in this range are to be accurately determined. The fluorescence was found to increase linearly between 12.5 Gy and 65 Gy, before decaying logarithmically beyond this. The decay was due to further reduction of the highly fluorescent resorufin, to the colourless and non-fluorescing hydroresorufin. However, this is only a hypothesis at this stage, and further investigation would need to be carried out to validate this.

Absorbance measurements at the excitation wavelength (530 nm) and emission wavelength (585 nm) of resorufin were measured to complement the fluorescence spectra measurements. The change in absorbance at the two wavelengths is believed to contribute to the sharp changes in the observed fluorescence.

A further experiment was conducted to emulate the conversion of resazurin to resorufin, but the results yielded a very different spectrum compared with that of an irradiated solution. This suggests that further chemical reactions occur during irradiation. These reactions could be producing molecules that affect the absorbance – and therefore the fluorescence spectra. In particular, the absorbance at the key wavelengths of 530 nm and 585 nm show a significant difference compared with the emulated conversion data. This is shown in Figure 4.23. To enable a better understanding, additional chemical processes that contribute to the non-linear response should be considered.

A final calibration curve was obtained, as shown in Figure 4.25. This curve should be used to determine the dose delivered. This is applicable for doses below 65 Gy,

which is not a significant hindrance, as most clinical radiotherapy fractions are kept below 2 Gy. In this dose range the dosimeter is very sensitive and should lead to a high level of accuracy.

Chapter 5

Further Dosimetry Studies at CLEAR

Further beam time was granted at CERN's CLEAR facility to test the resazurin chemical dosimeter. The aim of this additional experimental run was to apply what was learned about sample preparation, handling and behaviour to obtain more reliable measurements that demonstrate its potential as a viable real-time dosimeter for ultra-high dose rate VHEEs. The CLEAR beamline is described in Chapter 3.1. The dosimeter setup was placed 20.5 cm from the ICT, as shown in Figure 3.1. Prior to each run, the beam was aligned to a 9 mm diameter aperture placed on the beamline axis, using an alignment laser, and the beam's transverse size and energy was measured. The beam size varied slightly throughout the experiment to facilitate smaller and larger charges being delivered, and the energy was kept approximately constant, with an average energy of 200 MeV. The majority of samples were irradiated with 20 – 50 Gy, while other samples were irradiated with multiple kGy to quantify dosimeter saturation. Following the previous CLEAR experimental run, it was planned to stir the samples with magnetic mini stirrers to reduce the variability of the dosimeter response, and to study the effects of resorufin diffusion in the solution. However, the mini stirrers required were lost in transit so this could not be investigated, and no suitable alternatives were available. These stirrers were, however, tested at a later date, the results of which are presented in Chapter 5.4. The samples were not stirred during the gamma irradia-

tions at the CEA presented in the previous chapter, because the entire solution was irradiated, so it was therefore deemed unnecessary.

5.1 Methods

5.1.1 Dose-charge calibration

To know the absolute dose being deposited in the solution, the beam was first calibrated by irradiating Gafchromic film for a range of beam charges. This allowed accurate knowledge of the charge-dose ratio, which was used to determine the dose delivered based on the charge measured at the final integrating current transformer (ICT) in the beamline, and the beam area on the sample. Gafchromic HD-V2 film was irradiated with beams of charge up to $\approx$ 20 nC. The area of the beam was measured and used in calculations. As the dose delivered is equal to the energy per unit mass, the area of the irradiation beam determines the irradiated volume (assuming negligent beam divergence), and thus the mass. The following equation was used to determine the dose, D, of electron irradiation

$$D = 20.5 \times Q_1 \times \frac{A_0}{A_1}, \tag{5.1}$$

where Q_1 is the charge of the irradiation beam in nC, A_0 and A_1 are the areas of the calibration beam (1.43 mm^2) and the irradiation beam respectively, and the factor of 20.5 is determined from the calibration curve shown in Figure 5.1.

5.1.2 Dosimeter set-up

The dosimeter was positioned in the experimental area shown in Figure 3.1. For this experimental run, the excitation LED was moved so that it was perpendicular to the optical fibre collecting the emitted fluorescence. This reduces the average path length of photons collected by the optical fibre, reducing the effect of reabsorption of the emitted photons by the solution, which may alter the observed spectrum. This required a slight alteration of the set-up, as the LED could not be in the beam path, and neither could

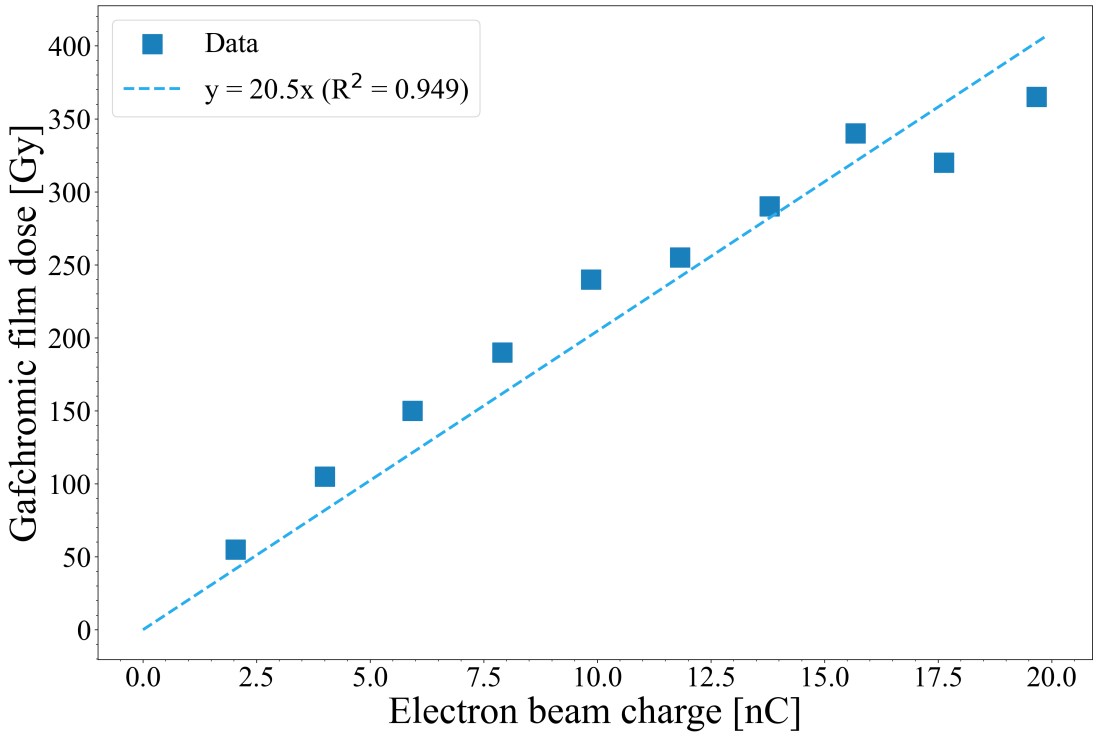

Figure 5.1: Dose-charge calibration curve for the CLEAR electron beam. The area of this particular beam was 1.43 mm^2. The fit equation $y = 20.5x$ was used to determine the doses of later irradiation from the measured charge, and the relative beam area, which is inversely proportional to dose and a function of volume.

the optical fibre. Therefore, the cuvette holder was placed on a lateral translation stage, as shown in Figure 5.2 to move the samples out of the beam path and into the path of the excitation LED where spectral measurements could be taken.

5.1.3 Resazurin solution preparation

The dosimeter solution was prepared by adding 5 mg of Sigma-Aldrich resazurin sodium salt to 1 L of a buffered water solution [125] to achieve a concentration of 19.9 μM, consistent with previous experiments. Previously at CEA experiments, tert-butyl alcohol was added to scavenge ·OH radicals. At CLEAR this was not available, so 0.584 mL of ethanol was added. This serves the same purpose but the volume must be appropriately adjusted to maintain the same concentration. Finally, the solution was stirred for at least 10 minutes. Once combined, the solution could be stored in the fridge for several weeks, but for this experiment a new solution was prepared each morning.

When required for irradiation, the solution was added to PMMA cuvettes that had been cleaned with ultra-pure water. 2 mL solution was added to each cuvette and sealed with a plastic cap. As before, the solution was de-aerated with neutral gas prior to irradiation; argon was used in this experiment ($>$ 99% purity). For each cuvette, two needles were pierced through the plastic cap: one for argon to enter and another for the gas to escape. The solution was bubbled at a constant flow rate for 60 seconds, before both needles were removed and the cap covered and sealed with electrical tape. As the volume of solution irradiated at CLEAR was 20% of the volume of solution irradiated at the CEA, the bubbling time at CLEAR was also 20% of that at the CEA. During the previous CLEAR experiment, the cuvette lid was not on during bubbling. The method used here emulates as close as possible the improved method used at the CEA, which glass vials and rubber stoppers, and increases the efficacy of the bubbling procedure to increase the scavenging potential of the resazurin. This leads to more reliable and consistent results.

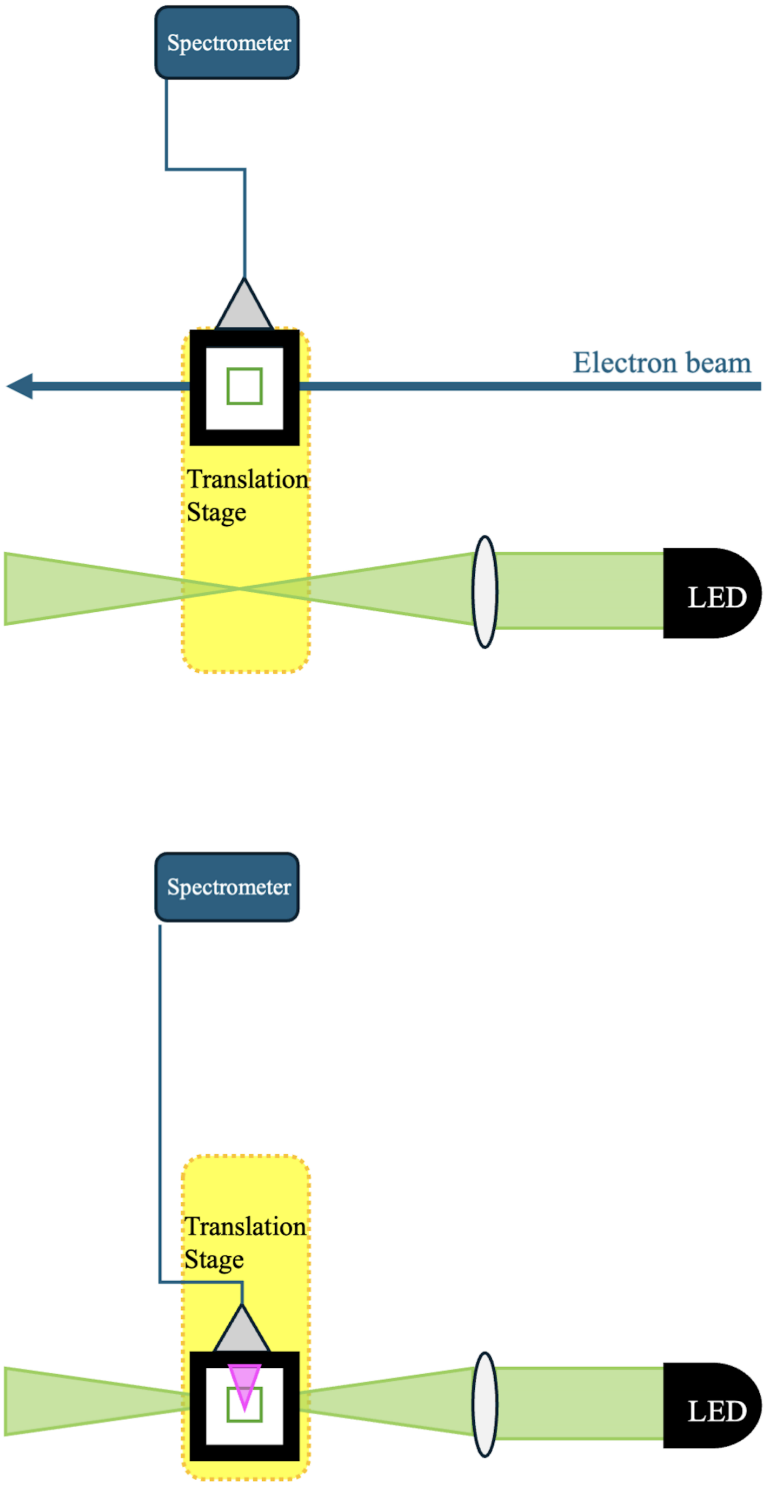

Figure 5.2: Dosimeter set up for the second experimental run at CLEAR. The repositioning of the LED required addition of a translation stage to move the samples into the beam path for irradiation (top), and into the path of the excitation LED for spectral analysis (bottom).

5.1.4 Irradiation of samples

The samples were stored in their holders to the side of the target area, and translated in and out of the target area using the CLEAR robotic arm after the beam was aligned and the desired parameters obtained. Samples were irradiated with the desired charge, then immediately moved into the LED path for spectral measurements. The time for the cuvettes to be translated from the beam axis to the LED axis was 24 seconds, in which time diffusion could occur and affect the observed spectrum. This was unavoidable, but samples were translated as quickly as possible after irradiation to minimise the impact. After a spectral reading was taken, the samples were moved back into the beam path for further irradiation, and this process was repeated until the desired accumulated charge – and therefore, dose – was reached. Irradiation of the samples took a few seconds (up to 1 minute for the kGy-level doses), and from 12 – 42 minutes for a sample to reach its maximum delivered dose. Due to diffusion of the resorufin molecules, a time difference could result in an inconsistent response of the dosimeter between samples. This is discussed further in Chapter 5.2.2.

5.1.5 Monte Carlo methods with FLUKA

FLUKA (FLUktuierende KAskade) [145–148] is a powerful program used in a wide range of areas including particle acceleration, radiation protection, particle physics and dosimetry. It uses Monte Carlo methods to simulate particle interactions and transport, which can complement experimental data or be studied on its own. Monte Carlo simulations typically treat a system as a series of probability density functions, then randomly samples this function many times and calculates the average over all these samples [149]. The larger the number of samples, the lower statistical uncertainty in the results. Many similar tools exist, but FLUKA was used during these studies.

FLUKA gives the user the ability to define all relevant parameters of the beam and the target, to estimate how it will respond to radiation under identical experiment conditions. In this work, FLUKA has been used to simulate the energy spectra of secondary electrons produced in water for the VHEE irradiations at CLEAR and the gamma irradiation at the CEA. These data are shown in Figure 5.10. FLUKA was

also used in Chapter 6.4 to compare the dose depth distribution and scattering of a collimated and focused VHEE beams through a phantom.

5.2 Fluorescence response to increasing dose

As in the previous experiments, fluorescence emitted from the irradiated samples was detected with an optical fibre and a FLAME UV-vis mini spectrometer. The spectra were saved and processed to extract the fluorescence intensity at 585 ±5 nm. The dose delivered for each shot to a sample was calculated from the calibrated electron beam charge (see Figure 5.1), and the fluorescence values were plotted against these doses to create a calibration curve for the solution, shown for each sample in Figure 5.3.

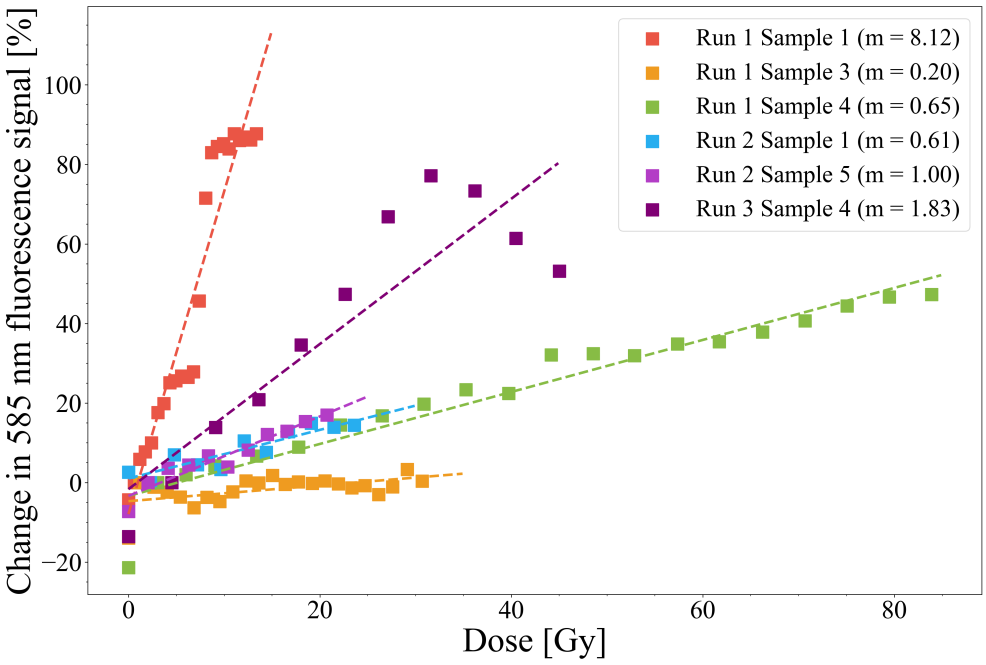

Figure 5.3: Variation of 585 nm fluorescence intensity of resorufin for a range of samples and various doses. The trends given by the slope m, are represented by dashed lines.

From Figure 5.3, we observe that the various samples irradiated do not respond in the same way, despite receiving similar doses per shot and total doses. Run 1 Sample 1 (red), for example, has a very steep gradient, whereas Run 1 Sample 3 (orange) has an almost flat response, despite being irradiated in the same run only 3.5 hours apart. This discrepancy between samples was not present in the data from gamma-irradiated

solutions, which responded to irradiation consistently. The solution preparation and handling procedure is identical, as is the read-out method, therefore it must assume the discrepancy is caused by the set-up, and the cause of it is rooted in the irradiation process itself.

A significant difference between the gamma-irradiated samples and these samples is the size of the source. The entire volume of the samples were irradiated uniformly with the gamma source, whereas these VHEE bunches have σ values of around 1 – 2 mm. Furthermore, the diffusion of resorufin through the solution is not instantaneous (it can take several minutes as discussed in coming section), and the solution was not stirred to promote homogeneity. Therefore, if the beam is not perfectly aligned with the excitation LED, some of the produced resorufin – the source of the induced fluorescence – may have not been excited by the LED and the fluorescence would not have been detected by the optical system. With this in mind, we decided to investigate the relative positions of the beams immediately before irradiation. We believe that the samples with flatter curves are further away from the LED axis than those with steeper gradients.

5.2.1 Relative positions of samples

Using the gradients of the calibration curves shown in Figure 5.3, a Python script was written to determine the optimal LED position, by determining the distance of each sample from the LED position. Each position trialled gave a distance from the LED axis for each sample. These were then plotted against the curve gradients, and fitted to a Gaussian curve - as this is the most appropriate relation, given the Gaussian profile of the beam. The LED position with the greatest R^2 value is the position plotted in Figure 5.4, and calculated positions are plotted with the respective gradients in Figure 5.5. The methods described were necessary to use post-experiment, because the true LED beam position during irradiation was difficult to measure directly due to the use of the robot arm.

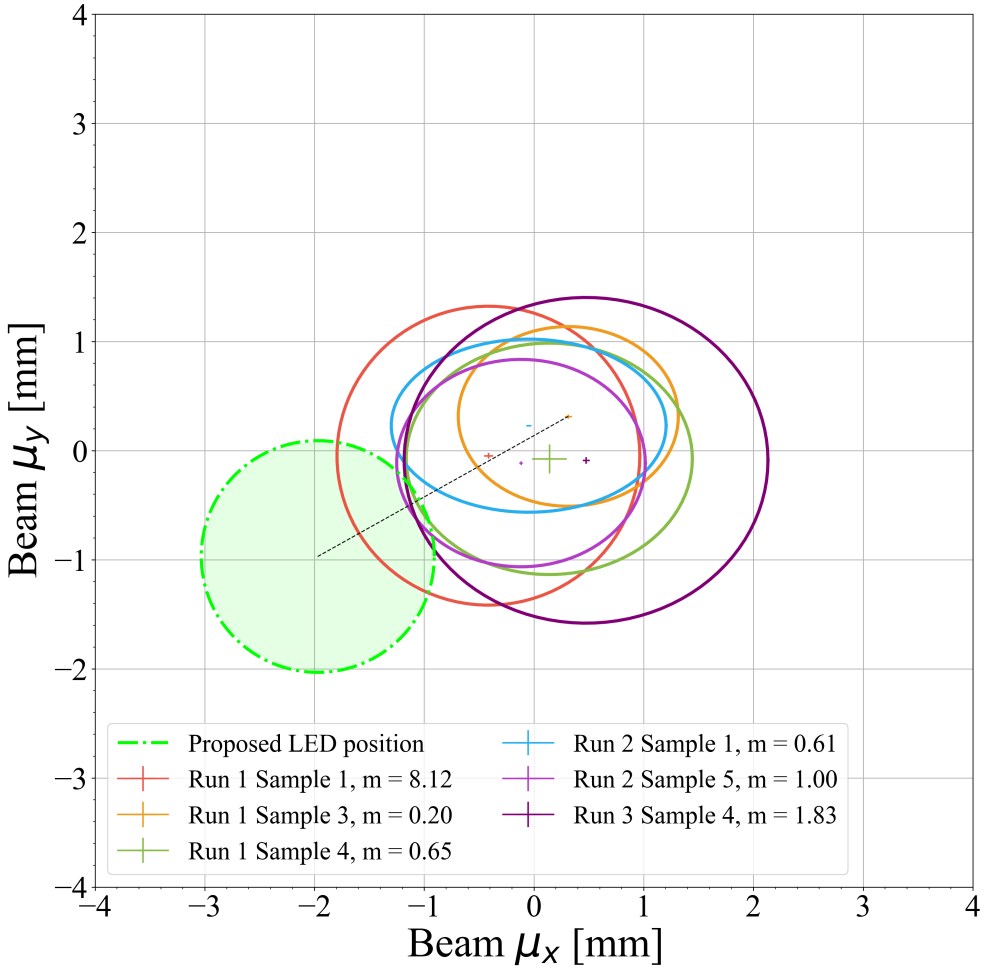

Figure 5.4: The approximate beam sizes for each sample (the σ value as measured by the beam diagnostic system) and suggested locations of the LED beams in relation to the electron beams, based on the gradients of the curves in Figure 5.3.

5.2.2 Diffusion time of resorufin

The diffusion equation taken from Atkins' Physical Chemistry (p. 778) [150], determines the time, t, for a molecule to diffuse a radial distance, x, and can be written as follows

$$t = \frac{x^2}{2D_{const}}, \tag{5.2}$$

where D_{const} is the diffusion constant of the molecule. The derivation of this equation can be found in Appendix A.1.

Diffusion constants of a range of molecules, taken from Atkins' Physical Chemistry

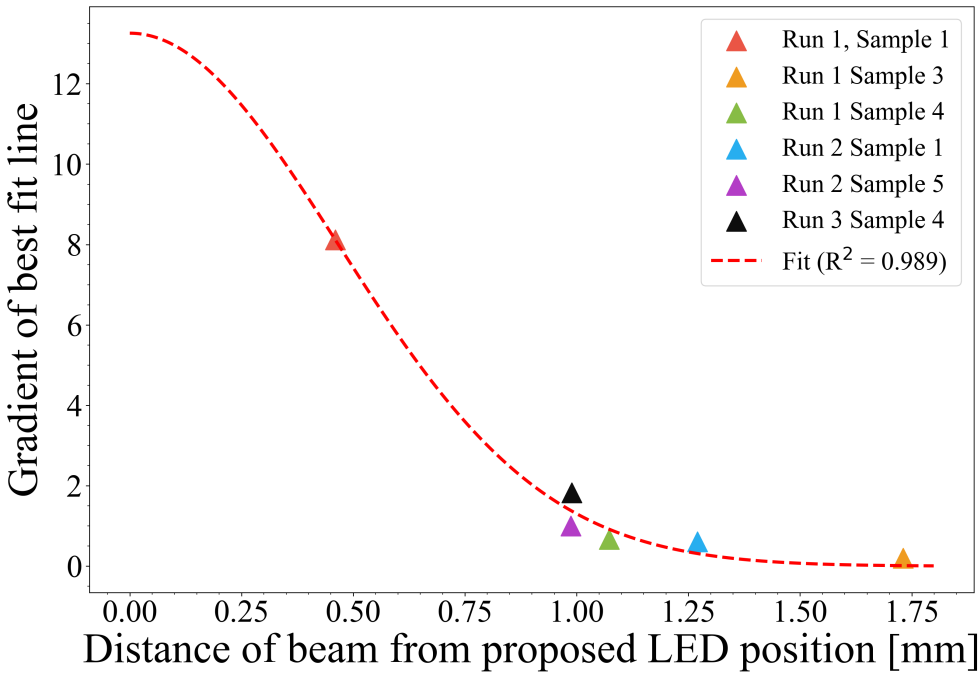

Figure 5.5: Computed fit for determining the most likely position of the excitation LED axis with for the range of samples. The fit used is Gaussian, using the gradients of the curves for each sample from Figure 5.3. This beam position was then used for determining the diffusion time for each sample in Equation 5.2 and Figure 5.6.

[150], and their respective molar masses, were used to calculate the diffusion constant of resorufin (further details in Appendix A.2), and this was calculated to be 6.31×10^{-6} cm^2/s. This diffusion coefficient was then used in Equation 5.2 to determine the time taken for resorufin to diffuse the relevant distances calculated previously.

From the spectrometer data, and the data saved by the CLEAR beam diagnostics, the precise time between sample irradiation and sample measurement could be calculated. The average over all deliveries for each sample was then taken, and compared with the theoretical time for resorufin to diffuse the distance calculated for each sample, and shown in Figure 5.6, and the exact values are shown in Table 5.1.

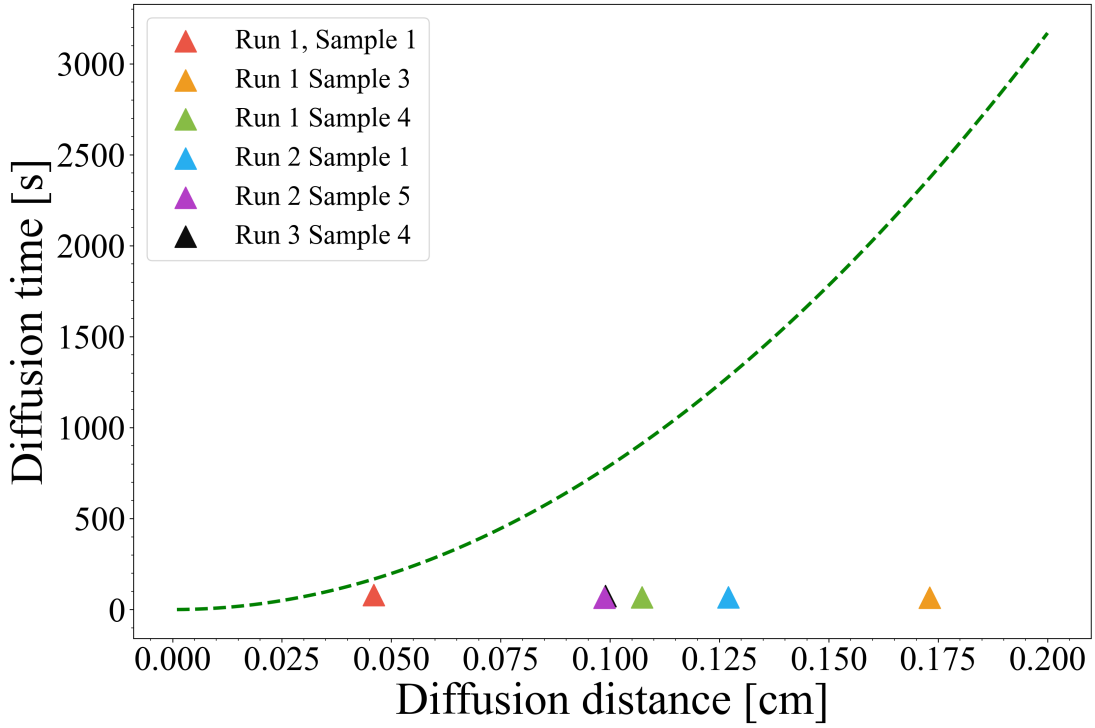

Figure 5.6: Diffusion time for resorufin in the solution. The dashed curve shows the distance diffused and the time needed to diffuse this distance. The points show the computed distances from the LED axis of the electrons beams for each sample, and their mean times between irradiation and analysis with the spectrometer.

As the data shows, the time between irradiation and taking spectral measurements was much less than the time resorufin would take to diffuse the proposed distance to the LED axis.

Finally, the difference in these times can be plotted alongside the gradients (taken

Sample	Proposed distance from LED axis [mm]	Diffusion time for proposed distance [s]	Mean time between irradiation and measurement [s]
Run 1 Sample 1	0.46	179	81
Run 1 Sample 3	1.7	2527	67
Run 1 Sample 4	1.07	971	69
Run 2 Sample 1	1.3	1362	68
Run 2 Sample 5	0.99	822	67
Run 3 Sample 4	0.99	826	76

Table 5.1: Each sample with the proposed distance from the LED axis, as computed and plotted in Figure 5.5, the time for resorufin to diffuse this distance (from Equation 5.2), and the mean time for each sample between irradiation and spectral analysis.

from Figure 5.3), to give a relationship dependent on both the measurement time after irradiation, and the predicted position of the electron beam with respect to the excitation LED axis. Figure 5.7 shows this relationship with a Gaussian fit. In other words, if the difference between the theoretical diffusion time and the irradiation-measurement time was zero, the increase in signal for a given dose would be at a maximum.

This suggests that the resorufin produced in the solution was unable to diffuse into the LED excitation volume and emit the fluorescence required to determine the dose. Having the solution stirred before a measurement is taken would greatly speed up the diffusion process to provide a more homogenous solution. This in turn would nullify the impact of the beam-LED misalignment.

Although the calculations performed above are based on a number of assumptions – such as the position of the LED and the Gaussian fits of the plots – we believe this is still a valuable tool that highlights the significance of diffusion of resorufin in this system. One could also look solely at Figure 5.4 without considering the proposed LED position, and compare the beam positions of the two samples with the most extreme gradients of the curves on Figure 5.3. For Run 1 Sample 1, the curve has the steepest gradient and the corresponding VHEE beam covers a significant volume of solution that the other beams do not. On the other hand, for Run 1 Sample 3, the beam occupies a smaller volume than the beam for any other samples. This simplistic, qualitative analysis highlights the influence of beam position on the detected fluorescence spectra

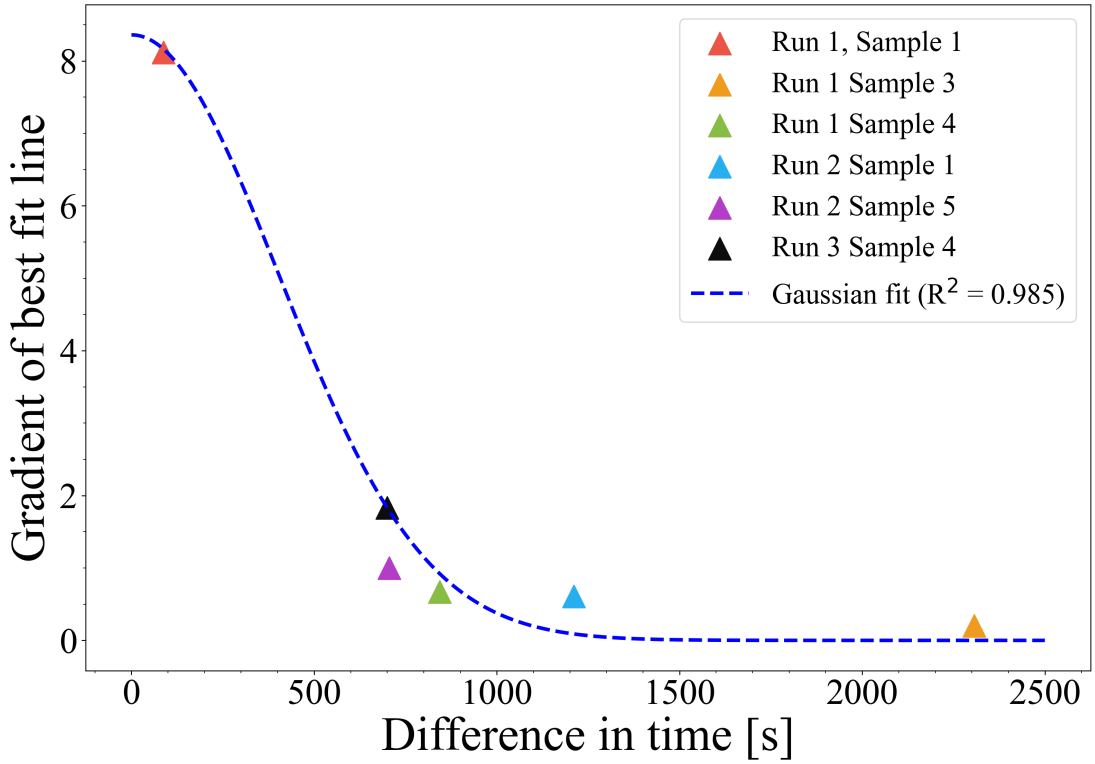

Figure 5.7: The gradient of the curve of each sample, plotted against the difference between the theoretical diffusion time and the mean time between irradiation and analysis for each sample (the two rightmost columns in Table 5.1).

for unstirred solution, however, could be more precise. It supports the conclusion that this is a promising explanation that should be verified experimentally. Following this suggestion, the response of the solution when stirred (so that the beam position and diffusion time are no longer relevant) is investigated in Chapter 5.4.

5.2.3 Retrospective application to our first CLEAR experiment

If we apply this technique to the data from the first CLEAR run, they don't follow a Gaussian trend as the data from the later experiment. This is shown in Figure 5.8. This suggests that although beam geometry and position is a very relevant aspect of the dosimeter response, the impact of the poor bubbling technique dominates. A less rigorous bubbling procedure, as used in the first CLEAR experiment, can result in more oxygen being present in the solution, and therefore larger variability sample to sample, as seen here.

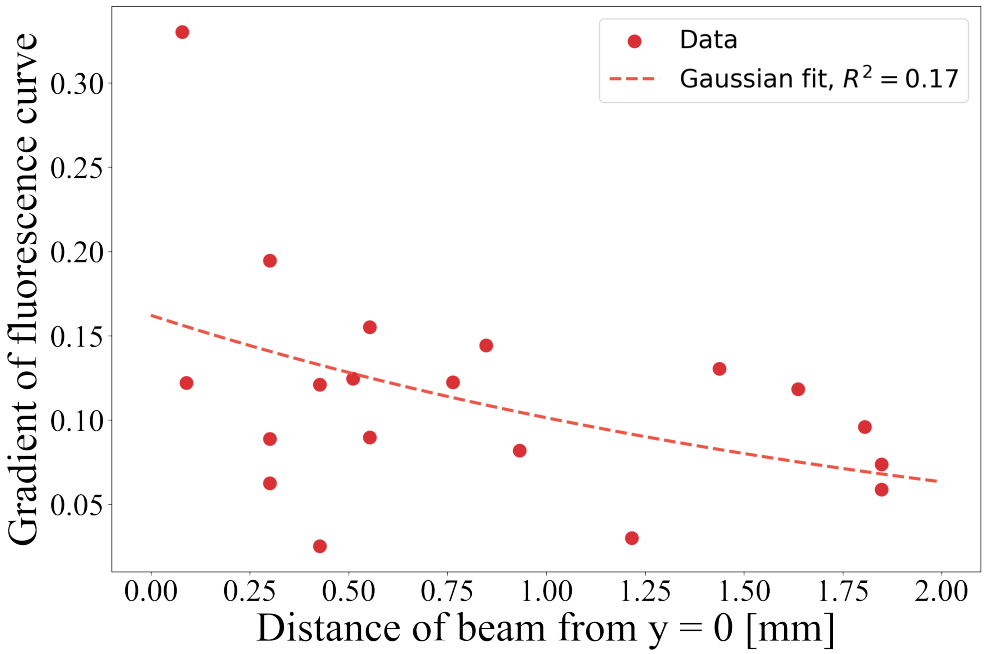

Figure 5.8: The distances from y = 0 (the excitation LED axis) of beams which irradiated samples during the first CLEAR experiment, and their respective fluorescence gradients. The data are plotted alongside a Gaussian fit, represented by the dashed line, which has an R^2 value of 0.17.

5.3 Dose saturation of the solution

The dosimeter was also irradiated with much higher doses to establish the upper dose limit, i.e. where the dose saturates, which is shown in Figure 5.9.

From Figure 5.9, it can be seen that there is no definitive upper dose limit that all samples tend to. However, three of the four samples appear to saturate at dose levels of 3,000 – 4,000 Gy, while the fourth sample saturates slightly lower, at around 2,000 Gy. It is difficult to say exactly why one sample appeared to saturate at a lower dose. The size of the increments could have been a factor. Run 1 Sample 4 was irradiated numerous times with lower doses, whereas for the other data in Figure 5.9, the first dose delivered was over 1000 times greater. This should be investigated further. If a pre-irradiation dose is required to remove contaminants, similar to that in Fricke solution [140, 141], our γ-ray studies at the CEA (see Chapter 4.3.7), suggest that this value for VHEE irradiation should also be determined.

The beam charge (and beam size) was regularly changed during the irradiation of

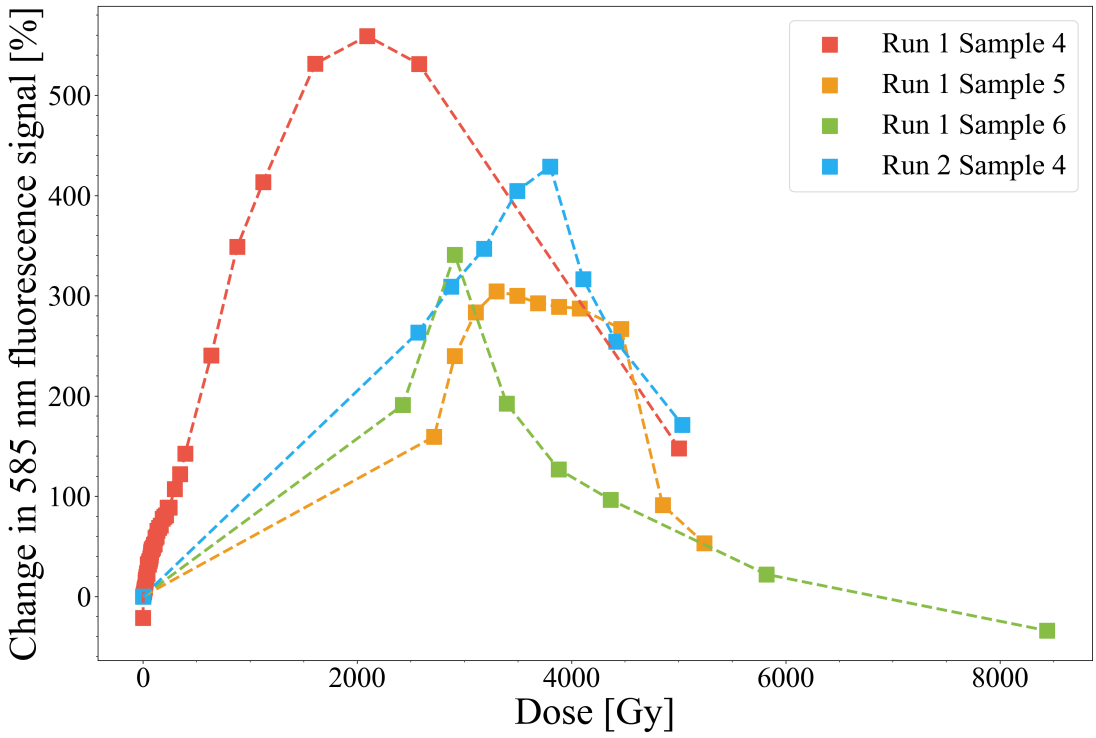

Figure 5.9: Fluorescence responses to high doses up to 8 kGy for a range of samples during the second CLEAR experimental run.

Run 1 Sample 4, whereas for the other three samples, the charges were more consistent. Another factor that may influence the overall increase in fluorescence is the time over which each sample was irradiated. Run 1 Sample 4 was irradiated for 1 hour and 50 minutes, whereas the other samples were irradiated for 30 minutes. This additional time would result in a greater diffusion of resorufin, possibly into the LED excitation volume, resulting in a larger increase in 585 nm fluorescence. The time difference here would correspond to a difference in diffusion length of around 1.3 mm (from Equation 5.2), which could be large enough have an effect.

The dose saturation data here raises a fundamental question: why can the dosimeter measure much higher doses with VHEEs than with gamma rays? The saturation dose differs by a factor of 30 – 60 between the modalities. One possible explanation could be due related to the difference in radiolytic yield of hydrated electrons for the two beams.

Hydrated electrons – the free radicals scavenged in the reduction of resazurin to resorufin – have been studied extensively for many decades, with researchers investigating how various factors such as LET, pH, and temperature affect their radiolytic yield [151, 152]. As radiation traverses a medium such as water or tissue, ionisation occurs along the particle tracks. For high-LET radiation, such as alpha particles and protons, the density of the ionisation events is greater than that of low-LET radiation, such as X-rays and gamma rays. As the beam energy is deposited along the tracks, clusters are formed, the size of which affects the level of DNA damage. A recent study has shown that there is a negative correlation between the cluster size and radiolytic yield of hydrated electrons [153]. Naturally, for a more concentrated beam, such as the VHEE beam used at CLEAR, the cluster size will increase. Not due to an increase in LET, but due to the ionisation events being physically closer together. Therefore, VHEE irradiation will likely yield fewer electrons available for resazurin to scavenge than gamma irradiation. However, this was only tested with electron energies up to 1 MeV, so work will be required to determine if this is definitely the case with VHEEs.

Another cause could be the difference in dose rates between the VHEE beam (10^9 Gy/s) and the gamma ray beam (0.06 Gy/s). While this was investigated in Chapter

3.4.1, the procedure is not yet robust, and insufficient data was collected to state with enough confidence that there is no dose rate effect. However, dose rate effects have been observed in other chemical-based fluorescent dosimeters e.g. terephthalate acid, trimesic acid, and coumarin-3-carboxylic acid (C3CA) [154]. These were compared by measuring the radiolytic yield of hydroxyl radicals for two different dose rates in the mGy/s range and the TGy/s range. It was found that the terephthalate and trimesic acid-based dosimeters did not vary significantly with dose rate (only up to 2%). Whereas the C3CA dosimeter changed by around 60%. This change in radiolytic yield was attributed to the effect of radiolytic oxygen depletion. Only low doses up to around 3 Gy were delivered in this study, but it could still be relevant to the resazurin solution. More work to investigate this should be carried out to determine if ours is truly dose rate independent.

Alternatively, the solution can also be compared with Fricke solution, which is already a reliable dosimetry method. In particular, its sensitivity to low energy secondary electrons produced in the solution during irradiation. It has been shown that they are the main contributors to changes in the ferric ion yield [155]. A similar effect could be present in the resazurin solution.

Figure 5.10 shows the results of simulations using FLUKA [156] to determine the energy spectra of secondary electrons in water for whole-solution gamma irradiation, and VHEE irradiation with a beam with the same size as used during the CLEAR experiment. The axis scales are identical for ease of comparison. The simulations show that there is a factor of 10–100 more low energy electrons (< 1 MeV) produced per unit dose during gamma irradiation, compared with VHEE irradiation. If the results of the previously mentioned study are also relevant to the mechanisms relevant to resazurin production, then the abundance of low energy electrons could result in a much more rapid saturation of our dosimeter – as observed in the CEA gamma ray experiments.

In summary, the resazurin dosimeter tended to saturate at a dose of $\approx 4,000$ Gy for VHEE irradiation, although one of the four datasets appeared to saturate at a much lower dose - $\approx 2,000$ Gy. The reason for this is not clear, but a likely explanation is the greater variation in the beam size during this run. It was also irradiated over a much

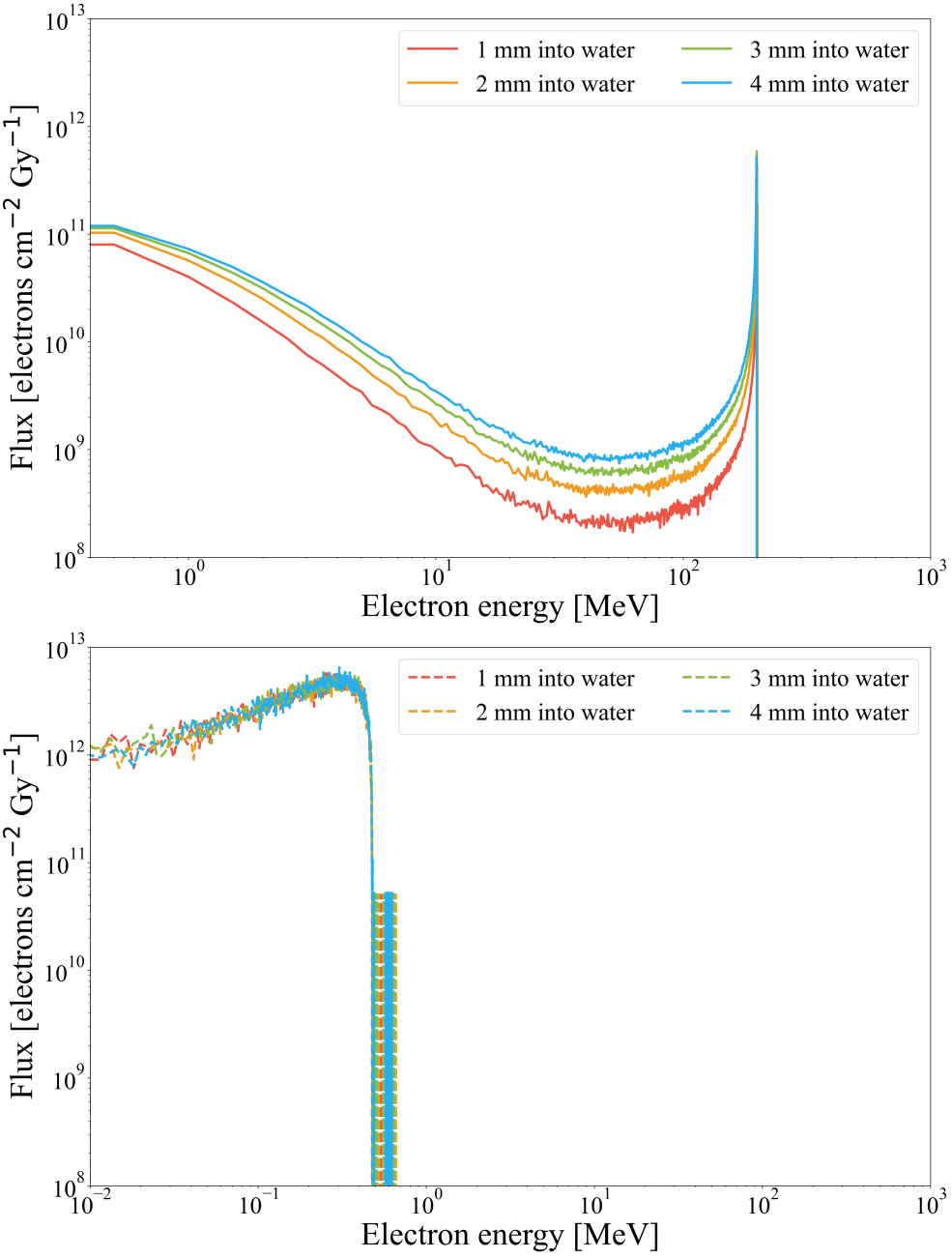

Figure 5.10: Secondary electron flux for VHEE irradiation (top) and gamma irradiation (bottom). Beams simulated were identical to those used in the experiment.

longer timescale (110 minutes compared to 30 minutes), which could have an impact on the amount of resorufin diffusing into the solution, beyond the excitation LED beam axis. Furthermore, the resazurin dosimeter was able to measure doses of up to $\approx 4,000$ Gy – compared to ≈ 65 Gy for γ-ray irradiation at the CEA – before the fluorescence from the resorufin began to decrease. This difference in dose saturation between the two beam modalities could be due to three possible causes:

- The more concentrated size of the VHEE beam could result in a decrease in radiolytic yield of hydrated electrons [153], resulting in fewer electrons available for scavenging – thus, less resorufin produced – per unit dose.
- The dose rate of the VHEE beam is much higher than that of the γ-beam – 10^9 Gy/s compared to 0.06 Gy/s respectively. Dose rate effects are present in other fluorescent dosimeters [154], but only at low doses. This effect could be present for greater doses in the resazurin solution.
- The yield of low energy secondary electrons for γ-irradiation is around 10-100 times greater than that of VHEE-irradiation, as shown in Figure 5.10. Secondary electrons have been shown to have an effect on the radiolytic yield of ferric ions in Fricke dosimetry [155], and a similar impact could be had on the yield resorufin in our solution.

These three areas should be investigated further to determine the true cause of this difference in saturation dose between the two modalities.

5.4 Magnetic stirring for accelerating diffusion

An additional CLEAR experiment was scheduled to test the magnetic mini-stirrers that we were unable to test previously. As the size of the VHEE beam at CLEAR is considerably smaller than the dimension of the solution, and the beam wasn't consistently aligned with the excitation LED, the diffusion of the produced resorufin through the solution would be an important factor (as outlined in Chapter 5.2). Tests were run to

quantify the impact of this and to demonstrate that by stirring the solution, one can produce more stable and reliable fluorescence signals.

A magnetic stirrer base was fitted in the cuvette holder previously used, that could be remotely switched on and off from the CLEAR control room. For each run, the preparation of samples was identical to the previous experiment, with the addition of cylindrical PMMA mini stirrers 5 mm in length and 2 mm in diameter. The PMMA coating prevented chemical interactions with the solution.

Before outlining these tests, it is worthwhile to show the time-dependent effect that diffusion has in an unstirred solution. Several samples were irradiated with identical VHEE bunches and were either stirred or unstirred. The spectrum was then continuously measured post-irradiation and the difference in spectra compared.

5.4.1 Unstirred vs. stirred solutions

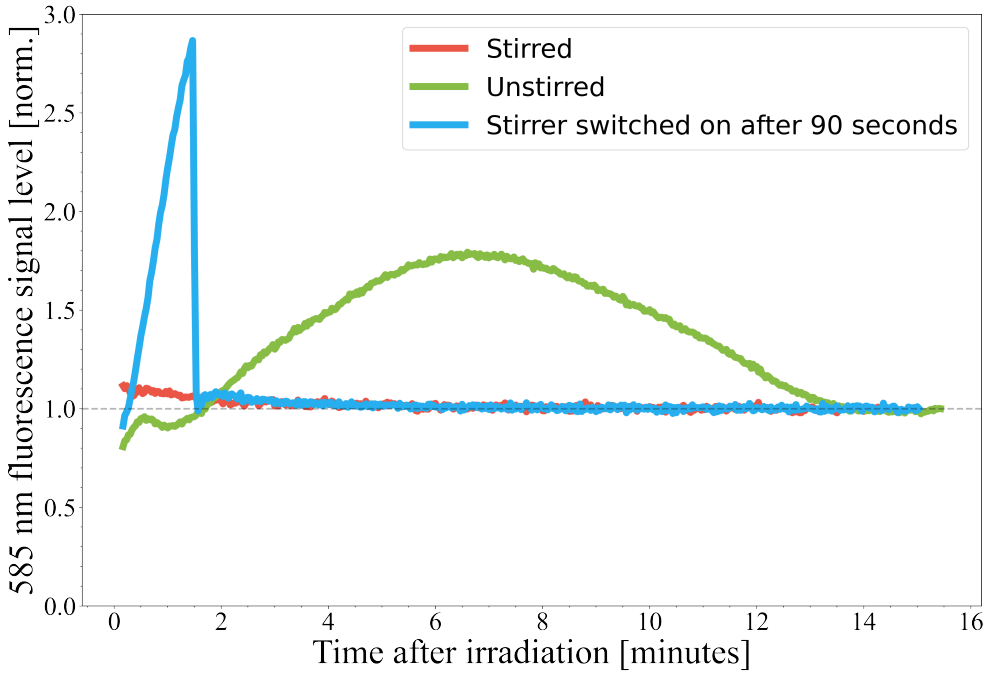

Figure 5.11: A solution stirred constantly (red), an unstirred solution (green), and a solution which was stirred after 90 seconds of spectral measurements (blue), all receiving around 8.5 kGy. The y-axis is normalised to the final value measured, as shown by the dashed line.

Figure 5.11 shows the 585 nm fluorescence signal level of three solutions that re-

ceived a single shot of around 8.5 kGy, normalised to the final value measured. The dose delivered was chosen to be high because the estimated dose delivered in the previous experiment was much higher than the actual dose delivered. This is due to the fact that the dose-charge calibration data used for previous experiments at CLEAR had changed slightly, and the divergence of the electron beam was greater than expected at the location of the cuvette. A new dose-charge calibration (see Figure 5.1) was performed after the experiment, thus the previously expected doses were not accurate. The dose saturation level was believed to be around 40 kGy before the dose-charge calibration was performed. The beam spot σ during this experiment was much smaller, around 0.7×0.6 mm^2. One sample was not stirred and left to diffuse naturally, another had a magnetic stirrer homogenising the solution throughout the entire process, and a third was initially unstirred, and after 90 seconds the stirrer was switched on. As can clearly be seen from the plot, the unstirred solution fluctuated significantly, increasing to a maximum (about 80% greater than the final value) after around six minutes. By 15 minutes post-irradiation, the signal had dropped again and appeared to stabilise. This is in contrast with the signal levels of the stirred solution, which rapidly reached a maximum, and a stable value was achieved after 5 minutes, varying by no more than 20% of this value. The third sample (blue line) initially increased similarly to the unstirred solution – albeit much more steeply. This steep curve is most likely due to the sensitivity of the beam position as discussed in Chapter 5.2, suggesting the beam was much closer to the excitation LED axis than it was for the unstirred solution, resulting in a much stronger initial fluorescence measured. Nonetheless, the signal stabilised within a few minutes after the stirrer was switched on. This suggests that stirring homogenised the solution, evenly distributing the resorufin. The resulting effect is that the signal strength is lower (but stable), as most of the fluorescent molecules are no longer in the path of excitation LED. The much sharper increase in this sample could be explained by the beam geometry once again, similar to the differing gradients in Figure 5.3. The beam diagnostics show that the beam position moved by around 0.22 mm between samples, which was sufficient to affect the measured fluorescence of an unstirred solution. By using larger, higher quality fluorescence collecting optics, one

may overcome this limitation and make the measurements less sensitive to diffusion effects.

5.4.2 Linearity and repeatability

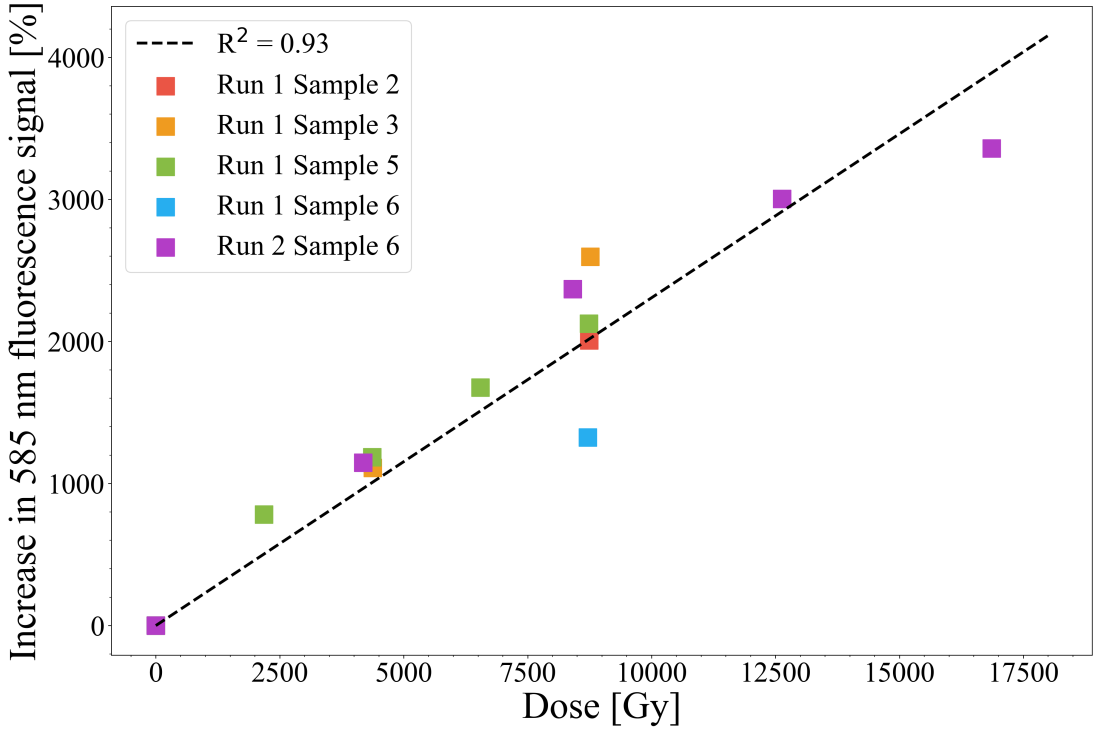

Figure 5.12: Increase in 585 nm fluorescence for samples from the second CLEAR run, which were stirred during irradiation and measurement. The fluorescence signal amplitude was measured after stirring for at least than 5 minutes.

Several further samples were irradiated with varying doses multiple times, and their dose linearity compared. In the previous CLEAR experimental run, with no stirrers, different samples exhibited different increases in fluorescent signal for similar dose ranges. This was attributed to the slow diffusion of resorufin through the solution, and the imperfect alignment of the electron beams with the LED axis. Whereas, with stirrers, there was a large improvement in repeatability of the dosimeter, as shown in Figure 5.12, which shows five separate samples increasing in fluorescence signal strength by the same amount per unit dose, following a linear trend with an R^2 value of 0.93.

Another difference noticed was the increased dose saturation level of the dosimeter

before saturation. This was tested in the previous experimental run without stirring, and the solution was found to saturate at around 2,000 - 4,000 Gy (see Figure 5.9). In contrast, doses of up to 12,500 Gy were reached with stirring before the dosimeter showed any signs of saturation. It appears that the dosimeter may saturate beyond this dose level, but limited beam time prevented further investigation to determine a definitive saturation point with stirring. This could be due to the inclusion of the stirring, which distributes the resazurin around the entire solution, replacing resazurin which has been reduced to resorufin in the LED excitation volume. The irradiated volume is very small compared with the total solution volume (around 5%), therefore without stirring, only a small fraction of the resazurin can be reduced to resorufin. On the other hand, stirring the solution may be equivalent to scanning the irradiation beam over the entire solution. Although this allows for more energy to be deposited in the solution, the total dose delivered – which is proportional to the irradiated volume – will remain the same. This effect should be investigated to determine the cause of the increase dose saturation of the dosimeter.

5.5 Discussion and comparison to gamma irradiation

Following the experimental run presented in Chapter 3, and the assessment of the methodology in Chapter 4, we expected that a second CLEAR run with a more effective de-aeration and altered geometry with stirrers would yield more consistent results.

Figure 5.3 shows the increase in 585 nm fluorescence for a range of samples with these changes implemented. The data yields far fewer null results than the previous CLEAR experiment, but the repeatability is still not ideal. This is likely due to the solution not being stirred following irradiation, as resorufin is not given sufficient time to diffuse through the solution into the path of the excitation LED (see Figures 5.4 – 5.7). Following the inclusion of stirrers in the solutions, the impact this had on the spectra of the solutions became evident, as shown in Figure 5.11. The increase in 585 nm fluorescence with respect to dose then became more repeatable, sample-to-sample, at high doses (Figure 5.12).

Unfortunately, we were unable to test the stirrers at the same doses shown in Figure

5.3, but given the variability in similarly high doses before the addition of the stirrers (see Figure 5.9), we are confident that at low doses the stirred solutions would be more consistent.

The dose saturation of the solution with VHEEs was measured to be between 2,000 and 4,000 Gy, which is much larger than the saturation dose established with gamma irradiation in Chapter 4, which was around 65 Gy. Several plausible hypotheses are outlined here, including a dose rate effect, the different density of ionisation tracks in the medium for the two beam modalities, and the abundance of low energy secondary electrons produced throughout the medium. If this dosimeter is to be fully understood and utilised in the clinic, these hypotheses should be carefully investigated and verified by dedicated physicists and chemists working together.

Strong evidence suggests that this may be a valuable tool for dosimetry, especially at FLASH dose rate levels. It provides an almost instantaneous on-line reading, is extremely compact and accessible for all researchers, and is also very sensitive at low doses used in radiotherapy.

One aspect not explored in our investigation is whether spatial information on the dose distribution can be measured, which would be a very useful clinical tool. However, we believe that this can be achieved by modifying the experimental set-up to include an array of dosimeters positioned in the beamline, which could give a measure of dose distribution in two or three dimensions. The resolution of this would be limited to the dimensions of the cuvettes used, but would be a worthwhile area to investigate, adding further value to the dosimeter. Micro-fluidics may help miniaturise the spatially resolving dosimeter.

Our dosimeter can be reliably used for VHEEs and gamma rays, with the potential of being used for X-rays and protons - providing they have sufficient energy to penetrate the cuvette wall. Good progress has been made with the dosimeter, but further work required to determine the full capabilities and scope of this dosimeter for clinical applications.

Chapter 6

Focused Very High Energy Electrons

6.1 Background

In addition to requiring precise dosimetry, UHDR radiotherapy needs an effective and efficient delivery method. Electrons – which are easier to produce and transport than protons and heavy ions – have a very limited penetration range in tissue at lower energies [157], therefore their application has usually been limited to treating superficial tumours [158]. In contrast, very high energy electrons (VHEEs), can penetrate much further into tissue. However, for collimated VHEEs there is a large spread of dose through the tissue due to scattering and the production of secondary electrons [159]. VHEEs focused with magnetic quadrupoles, on the other hand, can provide a much more pronounced depth dose distribution that allows for precise targeting of deep-seated tumours [160]. As seen in Figure 6.1, a focused VHEE beam delivers the smallest on-axis relative dose to healthy tissue surrounding a tumour compared with other modalities. Therefore, a tumour can be targeted more precisely, which can lead to improved efficacy of treatment.

During our CLEAR experimental run, in addition to testing our chemical dosimeter with a collimated VHEE, we also used magnetic quadrupoles to focus our beam into a water phantom. Gafchromic EBT3 film was used to measure the dose distribution and

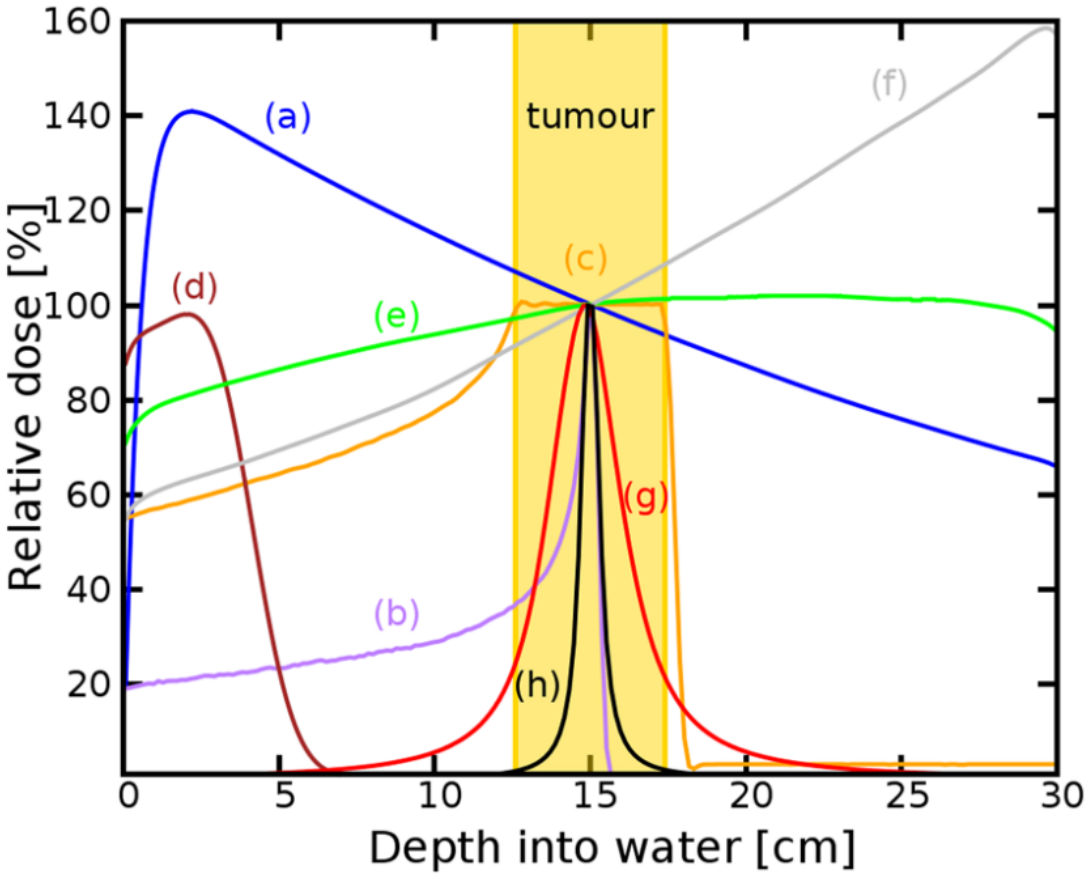

Figure 6.1: Relative depth dose distributions for a range of beam modalities: (a) 6 MV photons, (b) Bragg peak of 147 MeV protons, (c) spread-out Bragg peak, (d) collimated 10 MeV electrons, (e) collimated 200 MeV electrons, (f) collimated 2 GeV electrons, (g) 200 MeV electrons focused at 15 cm, (h) 2 GeV electrons focused at 15 cm [161]. Curves are normalised to the dose at the 15 cm focal point, apart from the 10 MeV electron beam, which is normalised to its peak dose.

Quadrupole	Current in quadrupole [A]
QFD 350	0.2
QFD 355	0.2
QFD 360	0
QFD 510	5
QFD 515	40
QFD 520	5
QFD 760	30
QFD 765	50
QFD 770	30
QFD 870	75
QFD 880	77

Table 6.1: The currents applied to the various focussing quadrupole magnets in the CLEAR beamline. All magnets have a nominal gradient of 11.2 T/m, an inner radius of 29 mm and an integrated gradient of 2.53 T/m.

scattering of the focused beam over 20 cm of the phantom.

Similar studies have been performed [160,162], where the distance between the final quadrupole and the phantom was 12 cm and 21.5 cm, respectively. In our experiment the final quadrupole was 130 cm from the phantom, which limited the focusing strength of our set-up. However, the work presented here demonstrates the first experimental measurements carried out with a VHEE beam focused in two-dimensions over this depth.

6.2 Methods

The CLEAR beamline is identical to that used in the first CLEAR experiment, which is shown in Figure 3.1. For VHEE focusing, the currents applied to the quadrupoles are listed in Table 6.1. These parameters were found to give the smallest focus in the short time available. As focusing the VHEEs inside the water phantom would have been a considerably lengthier process, we focused the beam at 150 cm from the final quadrupole, which coincided with a point 20 cm into the region where the phantom would be placed. The phantom was then placed using a vertical translation stage, which allowed observation of the benefits of focusing the beam, without being too time-consuming. All the focusing magnets in the beamline have a nominal gradient of

11.2 T/m, a inner radius of 29 mm and an integrated gradient of 2.53 T/m.

6.3 FLUKA simulations

Monte Carlo simulations were performed using FLUKA, which compared a collimated beam with a focused beam. The simulated collimated beam had the same dimensions as the beam delivered in the experiment, as measured by the Gafchromic film sheet closest to the phantom entrance. The simulated focused beam corresponded to an idealised version of our experimental set-up, with $\sigma = 10$ mm at the final focusing quadrupole. This was within the "good field radius" of the quadrupole which is 20 mm, therefore 95.4% of the simulated particles were enclosed within this region. This produced a beam with an f-number of $f/75$. The f-number quantifies the focusing strength of the beam configuration, with a lower f-number beam having a stronger focus. The f-number, N, is given by the equation,

$$N = f/D, \tag{6.1}$$

where f is the focal length of the set-up and D is the diameter of the beam at the final quadrupole. The beam was symmetrically focused to $\sigma = 0.3$ mm in air. The focus position of the simulation was set to match the focus position in air, as measured using a YAG screen scan before irradiation, which was 20 cm into the phantom volume, 150 cm from the final quadrupole. The beam was focused by defining the electron momentum coordinates the following equations:

$$\cos\phi_x = \frac{x - x_0}{\sqrt{(x-x_0)^2 + (y-y_0)^2 + (z-z_0)^2}}, \tag{6.2}$$

$$\cos\phi_y = \frac{y - y_0}{\sqrt{(x-x_0)^2 + (y-y_0)^2 + (z-z_0)^2}}, \tag{6.3}$$

$$\cos\phi_z = \sqrt{1 - \cos(\phi_x)^2 - \cos(\phi_y)^2}, \tag{6.4}$$

where x_0, y_0 and z_0 are the beam source coordinates, x, y and z are the beam focus co-ordinates, and ϕ_x, ϕ_y and ϕ_z are the angles between the beam propagation axis and

the direction of the particle momentum.

A $0.2 \times 0.2 \times 300$ mm^3 USRBIN scoring card was applied to determine the on-axis dose through the phantom. The resolution in the beam axis was 1.5 mm, and the resolution in the perpendicular axes was 0.1 mm. This could then be compared to the peak dose measured by the Gafchromic film.

20 more USRBIN scoring cards were used at 10 mm intervals along the z-axis of the water phantom in the simulation, with thicknesses the same as the Gafchromic film. The resolution in both planes perpendicular to the beam axis was 0.15 mm. The results of these gave the beam size as it traversed the phantom. These could then be directly compared with the beam size measurements obtained from the Gafchromic film scans.

6.4 Results

6.4.1 Dose depth measurements

A stack of 20 pieces of EBT3 Gafchromic film were evenly spaced by 10 mm inside a water phantom. After beam optimisation, the phantom was raised into the beam path and the films were inserted and irradiated. A single pulse of electrons was fired, with the charge chosen to correspond to approximately 50 Gy, and the mean electron energy was 204 MeV. After waiting at least 12 hours, the film was scanned using the same method as described in previous chapters, and the doses determined.

Figure 6.2 shows the normalised on-axis dose of three electron beams: our experimentally measured focused, a simulated ideal focused, and a simulated collimated beam. A collimated beam was not experimentally tested. The plot shows that by focusing the beam, the dose is more concentrated in the phantom. This is evident when comparing the two simulated beams, as the focused beam dose decreases at a greater rate than the collimated beam, and our experimental beam lies in-between these two regimes. The peak dose also extends further into the medium than for a collimated beam. Reducing the entrance and exit dose reduces the dose deposited in healthy tissue surrounding a tumour. While the difference is small with our experimental beam, an improved beam (as shown by the focused beam simulation) can increase the dose

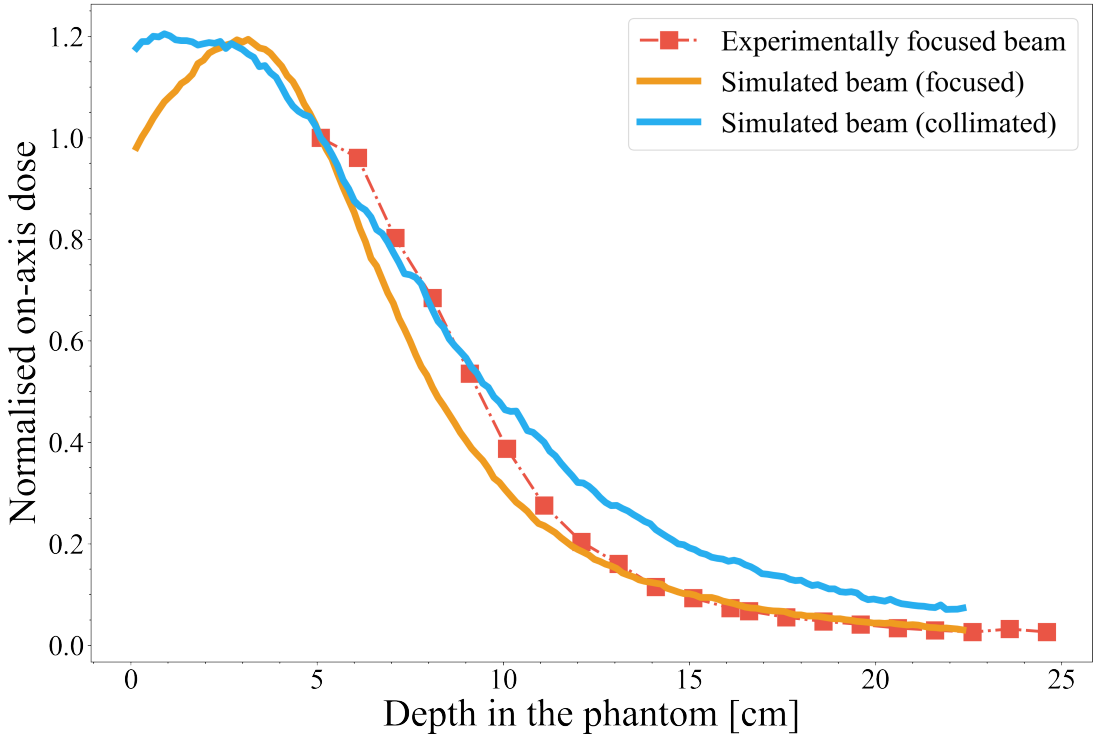

Figure 6.2: Relative on-axis dose through the phantom for the experimentally focused beam, an ideally focused beam simulated in FLUKA, and a collimated beam simulated in FLUKA. The dose values are normalised to the dose at the depth of the first Gafchromic film sheet.

concentration even further. Our experimental beam likely has a larger f-number than the simulation. Had the beam been optimised further, the f-number decreased, and the final focusing quadrupole been closer to the phantom, something more comparable with the simulated results could have been achieved. However, this was not possible in the time we had, and with the small quadrupole apertures. From a clinical perspective, focussing on a tumour close to the surface results in a lower dose, and therefore reduced toxicity to healthy tissue behind the tumour. Changing the depth of focus in the phantom allows for precise targeting of tumours, depending on how deep into tissue the tumours are found. The peak dose of the beam can be delivered deeper into the tissue by decreasing the f-number. It can also be achieved by moving the focus position deeper, but this leads to a spreading of the dose before and after the focus. Figure 6.3 shows this, as the f-number was varied for three different focus depths in the phantom. The beam diameter at the final focusing quadrupole was kept constant, with $\sigma = 10$ mm, as before.

Figure 6.4 shows a beam configuration in which the final focusing quadrupole is placed at the entrance of the phantom. The beam size at the quadrupole has also been increased to allow $\sigma = 20$ mm. This greatly decreases the f-number and leads to a more desirable dose distribution. Additionally, the focal spot size is decreased to $\sigma = 0.1$ mm. By doing this, a much more desirable dose profile can be achieved. However, the deeper into the phantom the beam is focused, the higher the f-number, and therefore the higher the relative entrance and exit doses to the patient. Simulations show that for higher energy electrons, 2 GeV, the entrance and exit doses are reduced further, as the scattering is reduced [135]. This simulation data highlights the potential of a focused VHEE system, as it allows more efficient targeting of deep seated tumours, for cases where conventional electron beam radiotherapy cannot reach.

6.4.2 Beam divergence

Using the scans of the Gafchromic film sheets, the FWHM of the beam through the phantom can also be measured. These values are plotted alongside the simulated data in Figure 6.5, which show the more rapid divergence of the focused beam as it enters

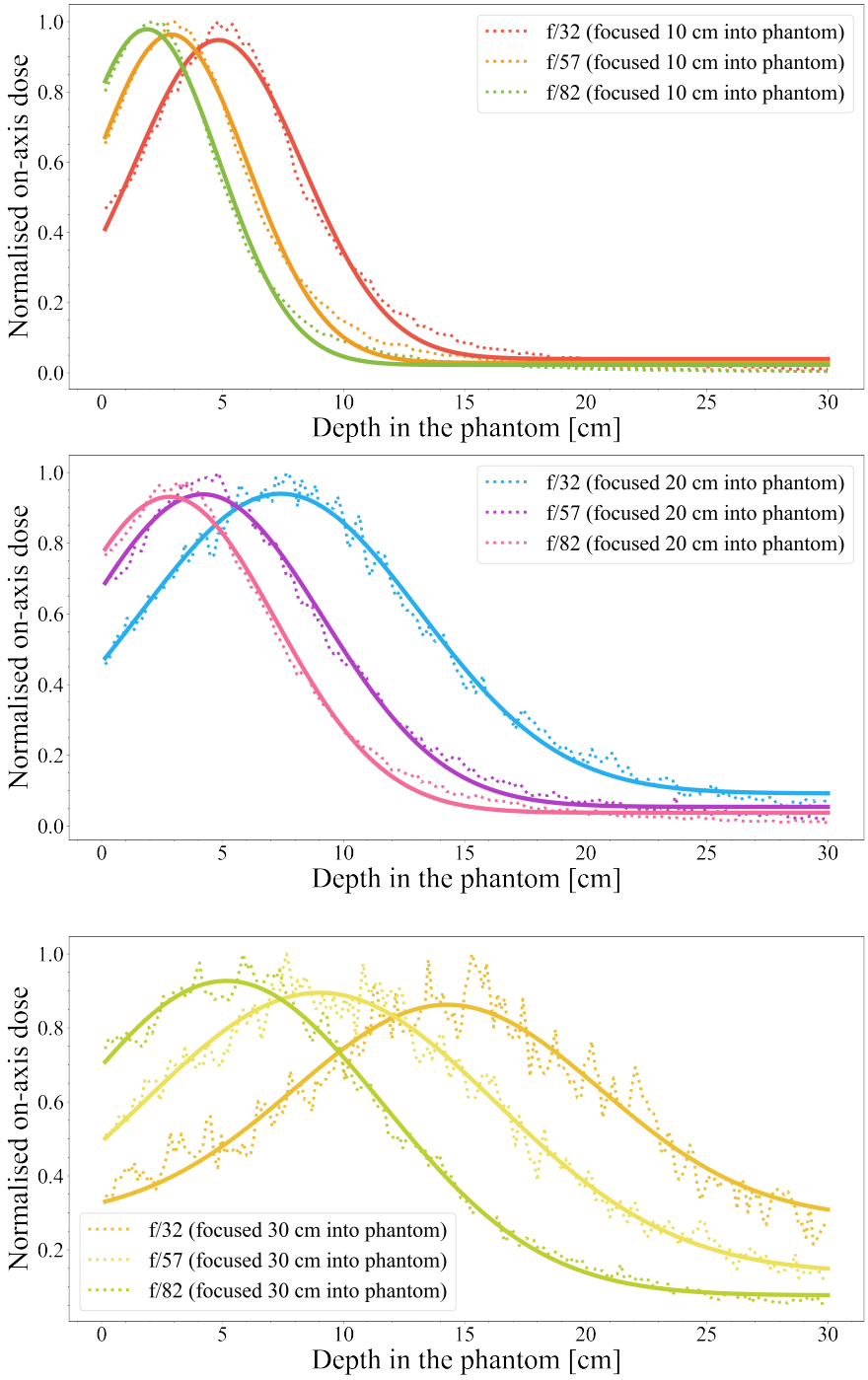

Figure 6.3: Raw data (dotted) from FLUKA simulations and Gaussian fits (solid) comparing different focus positions in the phantom with different f-numbers. The beam sizes at the final focusing quadrupole and the focus are identical, with $\sigma = 10$ mm.

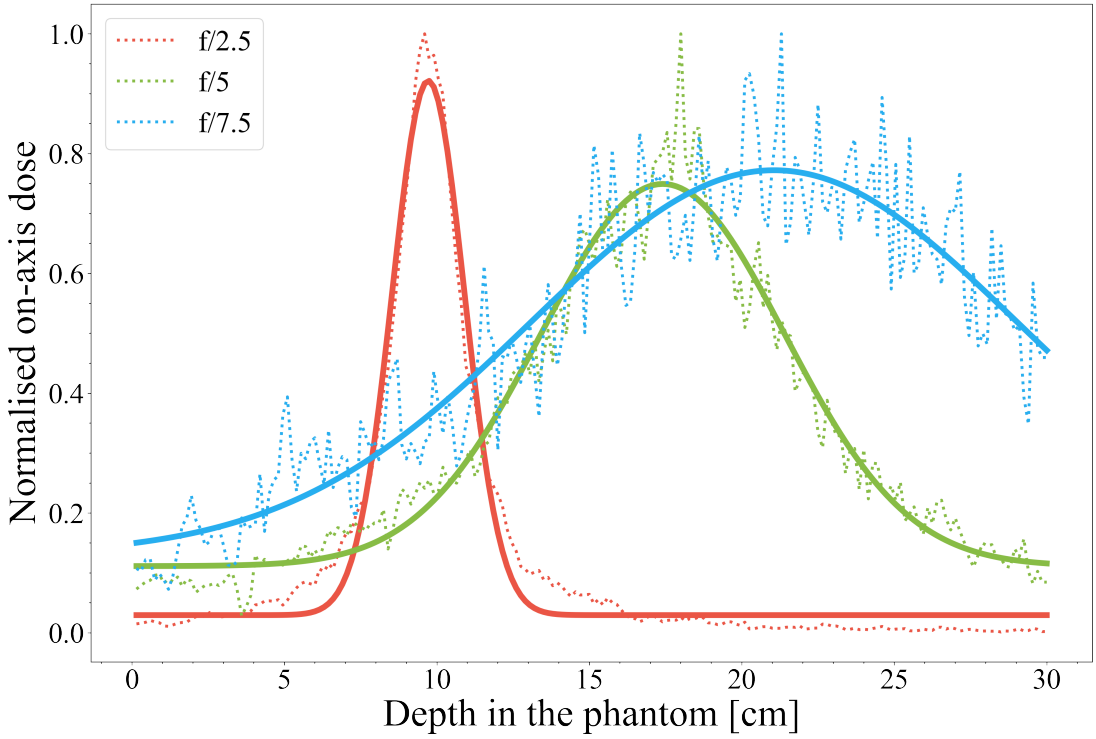

Figure 6.4: Results from FLUKA simulations of a beam focusing set-up where the final quad is at the phantom entrance. At the quad, the beam $\sigma = 20$ mm, and at the focus $\sigma = 0.1$ mm. The dotted lines are the raw simulation data and the solid curves are Gaussian fits.

the phantom. The simulated focused beam has a much tighter focus, and therefore more divergent beam through the phantom. It is this spreading out of the beam that results in a lower dose, as the electrons are distributed over a larger volume than if they were collimated.

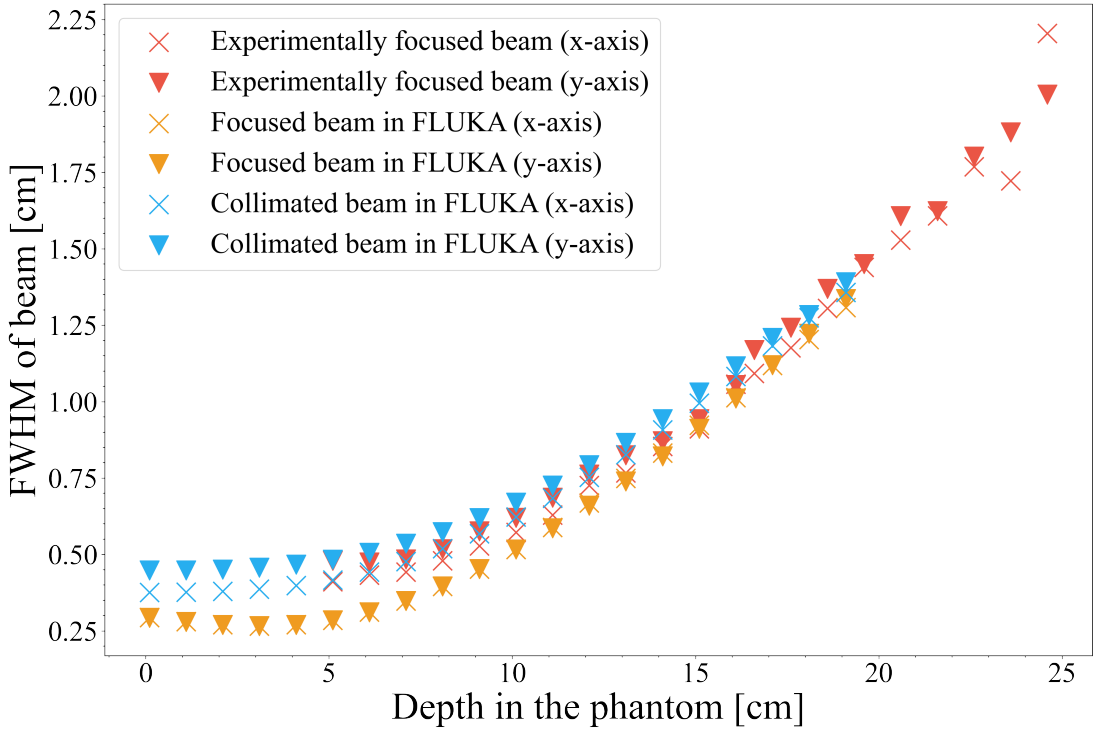

Figure 6.5: Divergence of our experimentally focused beam through the phantom at CLEAR, compared with a focused and collimated beams simulated using FLUKA.

6.5 Discussion

From the figures, there is a small but clear improvement in the dose concentration for a focused beam compared with a collimated beam for the parameters considered. However, this could be enhanced by optimisation, which would require more time. Since a collimated beam was not used in the experiment, this should be tested to verify the simulation data. The final focusing quadrupole in the beamline was much further from the phantom than in previous, similar experiments [160,162], which had distances (from the centre of the magnet to the edge of the phantom) of 32.8 cm and 22 cm, respectively,

compared with 143.5 cm in our experiment. Since the diameter of the beamline is fixed, this shorter distance allowed for much smaller f-numbers, and therefore much tighter foci and a more concentrated dose depth distributions. Additionally, as CLEAR is a shared user facility, components in the beam line are left in place from previous experiments, as was the case in our run, where components that could contribute to beam loss were still present. While this didn't have a large effect on our dosimeter study, they became more significant when the beam was expanded in order to focus it. This made achieving a more convergent beam more difficult. Again, with a fully dedicated experiment, our study here could be greatly improved, and dose distributions more similar to those shown in Figures 6.3 & 6.4 could be achieved.

Focused VHEEs have a greater potential to achieve FLASH doses, especially if they are produced by laser wakefield accelerators that produce ultra-short bunches. By combining the FLASH regime with the flexibility offered by this focusing system, a broad array of radiotherapy opportunities could become available, which are currently not possible using collimated, linac-produced VHEEs.

Chapter 7

Detection of 511 keV photons from the decay of oxygen-15

This chapter outlines our first findings arising from a collaboration with the University of the West of Scotland (UWS), which were performed in parallel to the second CLEAR experiment presented in Chapters 5 & 6. Dosimetry based on the detection of 511 keV photons emitted following the decay of oxygen-15 (^{15}O) is investigated as a rudimentary PET scanner, that can be used as a non-invasive real-time dosimeter. Initial data are presented and the scope for future experiments outlined.

7.1 Background & theory

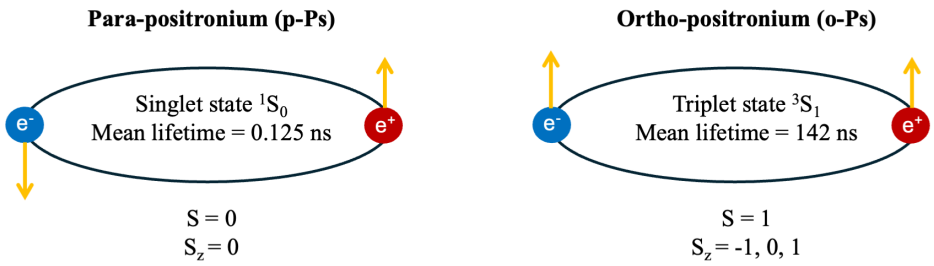

Figure 7.1: The two states of positronium, with different spin orientations and mean lifetimes differing by a factor of ≈ 1000.

As VHEEs pass through tissue, or water, the resulting bremsstrahlung radiation produces a continuous spectrum of X-ray photons, the maximum energy of which corresponds to the kinetic energy of the incident electrons. This spectrum can be approximately modelled with a $1/E_\gamma$ function, where E_γ is the photon energy. These can create radioactive isotopes by γ photon-induced reactions. These can include oxygen-15 and carbon-11, two relatively short-lived isotopes that decay into stable elements while emitting a positron. The positron then annihilates with electrons to produce a pair of 511 keV photons emitted in opposite directions, and around 60% of the positrons annihilate directly. The remainder annihilate via the production of positronium: an exotic, hydrogen-like atom with a positron replacing the proton nucleus [163]. The positronium atom can exist in two states, shown in Figure 7.1: a singlet state, known as para-positronium with antiparallel positron and electron spins (p-Ps; S = 0, S_z = 0), and a triplet state, known as ortho-positronium, with parallel positron and electron spins (o-Ps; S = 1, S_z = 1, 0, -1). These two states have significantly different mean lifetimes: 0.125 ns for p-Ps and 142 ns for o-Ps. The lifetime for p-Ps is relatively stable as it undergoes self-annihilation. O-Ps, on the other hand, cannot undergo self-annihilation because of its non-zero spin quantum number, S, which is conserved. However, it can annihilate with nearby electrons and decay via the emission of three photons, the energy of which add up to $2m_ec^2$ = 1.022 MeV. Its lifetime, therefore, is very sensitive to its environment, and in particular oxygen content. A higher oxygen content results in a shorter lifetime because the interaction with its surrounding environment flips one of the spin states to create p-Ps [164], which then decays rapidly.

Numerous studies have investigated the difference in lifetime for clinical applications. For example, one study successfully identified differences in the partial pressure of oxygen (pO_2) in ^{22}Na solutions, which mimic the conditions seen in tumour hypoxia [165]. Using a time-of-flight PET scanner, it was found that the o-Ps lifetime decreased linearly with the partial concentration of dissolved oxygen, which was varied between 0 and 160 mmHg. For context, tumour tissue has an average pO_2 value of 10.27 mmHg, with prostate and pancreatic cancers being as low as 3 mmHg [166]. Healthy tissue has an average of 45.8 mmHg while the concentration of oxygen in air

at atmospheric pressure is 160 mmHg. Another team developing the Jagiellonian PET (J-PET) system [167], showed that it can identify two 511 keV annihilation photons similar to that in conventional PET scanners, but also a prompt γ-photon emitted by some radioactive isotopes. The detection of this prompt γ- ray provides information on the positronium lifetime, and thus the tissue local environment. The team applied their method to in-vivo images of a patient with a glioblastoma brain tumour, and found that the positronium lifetime was shorter in the tumour than in the healthy brain tissue. Thus they believe that this method could be used to diagnose disease in-vivo.

The method described here aims to achieve a similar goal, and provide information on a target's environment during irradiation, giving the additional benefit of a non-invasive imaging modality to electron radiotherapy. By measuring the lifetime of the positronium it is hoped to directly probe the oxygen content, which is lower in tumours than in healthy tissue, allowing a method of distinguishing between the two during beam delivery. In a scenario where a patient returns for multiple dose deliveries over a period of time, this would allow monitoring of the tumour, thus improving the efficacy of treatment.

7.2 Experimental set-up and method

The experimental set-up, as shown in Figure 7.2, is identical to that presented in Chapter 5, with the addition of a T25 water phantom that can hold up to 70 mL placed directly behind the cuvette holder, and two $LaBr_3$ detectors are used to detect and count 511 keV photons emitted from the water. PET scanners comprise an array of detectors that surround the patient, implying that our method detects only a very small fraction of emitted photons.

The detectors were intended to be connected to a multi-channel analyser for data collection, but this arrived at CERN damaged at the start of the experimental run. Delays in finding a replacement resulted in acquiring less data than anticipated, limiting the scope of the experiment. Nevertheless, measurements were made for two doses of VHEEs: 2.5 kGy and 5 kGy. Photon counts were saved and visualised using a Tektronix MSO64B Mixed Signal Oscilloscope (10 GHz bandwidth, 50 GS/s sample

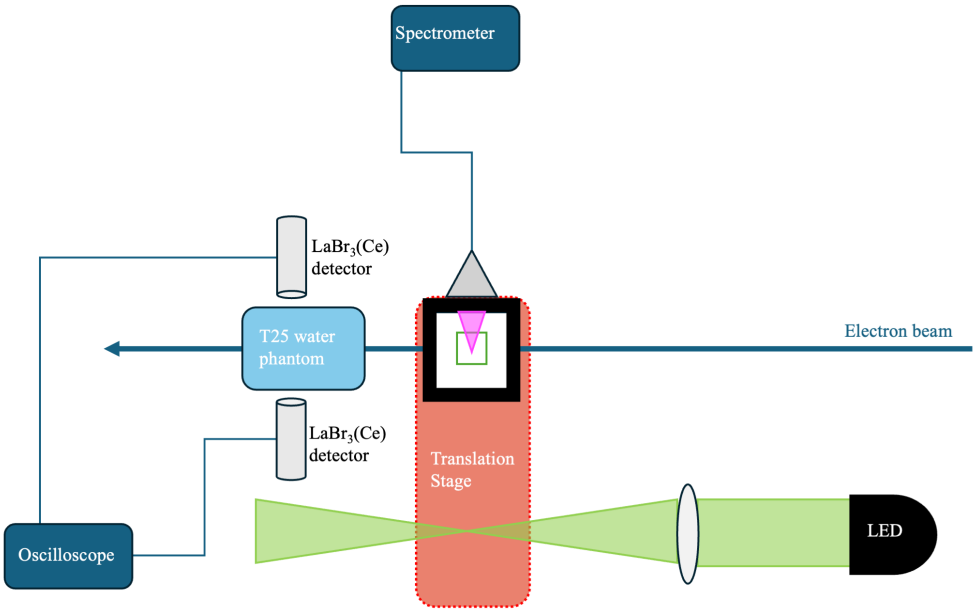

Figure 7.2: Experimental set-up for the detection of 511 keV photons. It was attached to the end of the beamline during our dosimetry experiment, without the two interfering. $LaBr_3$ detectors measure the counts and this is visualised and saved through the oscilloscope.

rate). The trigger rates were recorded every 30 seconds, taken in parallel with the chemical dosimeter analysis. This enabled the decay of the oxygen-15 and carbon-11 to be conveniently measured over the same period as that of the chemical dosimeter that diffusion occurred.

7.3 Results

Measurements were made for several electron beam deliveries at two doses (2.5 kGy and 5 kGy), and the 511 keV photon counts are shown in Figure 7.3, which clearly shows its high level of reproducibility. The data are plotted alongside two-component exponential fits with the following equation

$$f(t) = N_0 e^{-\lambda_0 t} + N_1 e^{-\lambda_1 t}, \tag{7.1}$$

where N_0 and N_1 are the counts (in kHz) of the two radioactive components at time, $t = 0$, and λ_0 and λ_1 with the respective element decay constants. These are be used

to calculate the half-life of each element, $t_{1/2}$, given by:

$$t_{1/2} = \frac{ln(2)}{\lambda}. \tag{7.2}$$

Table 7.1 shows the fit parameters for the two curves. Using Equation 7.2, the λ_0 values for 2,500 Gy and 5,000 Gy give half-lives of 114±12 seconds and 119±10 seconds, respectively. These correspond to ^{15}O, which has a half-life of 122 seconds [168].

Similarly, the two λ_1 values for 2,500 Gy and 5,000 Gy give half-lives of 24 ± 4 minutes and 23 ± 3 minutes, respectively. These correspond to carbon-11, which has a half-life of 20 minutes [169].

The source of carbon-11 is most likely due to the interaction of electrons with the PMMA of the phantom walls containing the water. Importantly, the signal count of ^{15}O (N_0) scales approximately linearly with dose, increasing by $91.5 \pm 8.8\%$ when the dose is doubled. This suggests that simply by measuring the photon count from this decay, one can determine the dose deposited in a patient by VHEEs. If this technique were to be combined with an array of detectors, such as in PET imaging, it could also provide information on the location of the dose deposition.

	2,500 Gy shot	5,000 Gy shot
N_0	46.48 (±2.05)	89.05 (±3.88)
N_1	33.66 (±3.09)	49.46 (±3.25)
λ_0[s^{-1}]	6.1 (±0.73)×10^{-3}	5.83 (±0.54)×10^{-3}
λ_1 [s^{-1}]	4.9 (±1.12)×10^{-4}	5.0(±0.64) × 10^{-4}

Table 7.1: Calculated fit parameters for the curves plotted in Figure 7.3. N_0 and λ_0 correspond to the contribution from oxygen-15, while N_1 and λ_1 are from carbon-11.

In addition to the photon counts, the pulse heights were measured, and their frequencies are plotted in Figure 7.4. The pulse height is proportional to the photon energy, and the resulting spectrum is consistent with the detection of 511 keV γ-rays, showing two peaks. Access to calibration sources during the experiment was not possible, therefore the conversion to energy could not be performed. However, the peak at 0.39 is most likely due to the 511 keV γ-rays emitted by positron-electron annihilation.

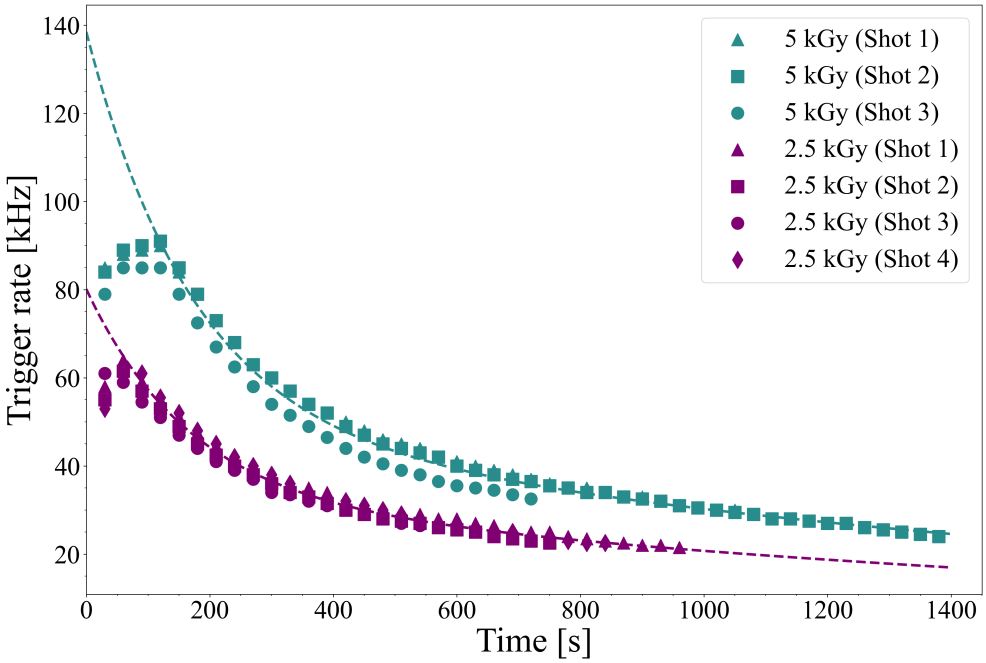

Figure 7.3: Oscilloscope signal from 511 keV photons emitted from the water phantom following several high dose deliveries. Radioactive oxygen-15 is produced during irradiation. This decays into nitrogen-15 and emits a positron, which quickly annihilates with a nearby electron, producing the 511 keV photons detected.

7.4 Discussion and future outlook

Despite only collecting data for two doses, the results are very promising. Figure 7.4 shows the dose linearity for photon count of the oxygen-15 component, and both curves show excellent reproducibility. This is a valuable first step towards using this technique for real-time dosimetry, which could be of great interest for radiotherapy. However, more research is required to fully understand its capabilities. A future experiment at CLEAR is planned for later this year, to repeat the experiment with dedicated electronics, and a wider range of clinically useful doses. Additionally, by varying the oxygen concentration of the T25 phantom, it is hoped to mimic the environment of healthy tissue and hypoxic (less oxygenated) tumour tissue and study the lifetime of o-Ps. This will enable determination of the local environment based on the o-Ps lifetime and allow the distribution of oxygen content to be determined.

It is hoped that the technique will allow for the study of hypoxic tumours and cells, which have low oxygen content and are more radioresistant than healthy tissue. VHEEs,

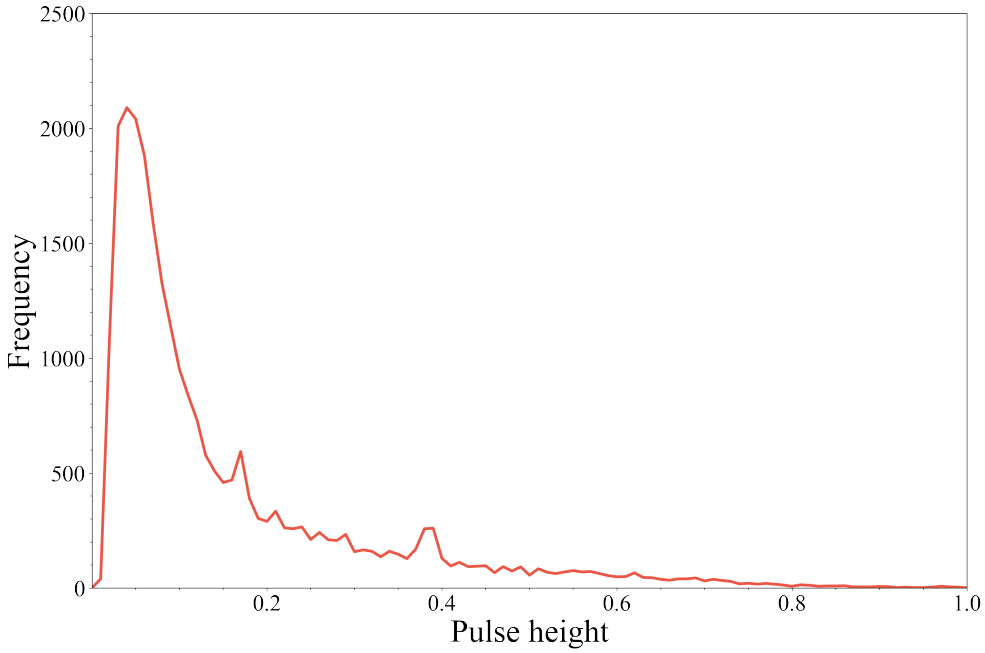

Figure 7.4: $LaBr_3(Ce)$ energy spectrum, consistent with detection of 511 keV γ-rays [data provided by Kellieanna Byrne (University of the West of Scotland)].

in particular, can deliver high doses at ultra high doses rates, and therefore capable of inducing FLASH effects, the cause of which is still not yet fully understood. If the cause of the FLASH effect is due to oxygen content, as some have speculated [170,171], it would be a valuable investigative tool providing a real-time, non-invasive oxygen sensitive imaging modality for use with VHEEs.

Chapter 8

Discussion and Outlook

8.1 Discussion and conclusions

It is clear from the literature that FLASH has potential to create a paradigm shift in cancer treatment. Numerous studies have shown that for doses delivered at ultra-high dose rates (UHDRs), healthy tissue is spared by ionising radiation, while tumour tissue is damaged, increasing the survival rate for cancer [27–33]. The International Committee on Radiation Units and Measurements (ICRU) requires a dose to measured with an accuracy less than 7% [41]. Conventional dosimeters, including ionisation chambers – the gold standard for clinical dosimetry measurements [42] – experience significant complications with UHDR radiation, which prevents such accuracy from being achieved [43–45]. Alternative dosimetry methods, such as radiochromic film (RCF), alanine and calorimeters are available, but are hindered by fundamental limitations, making them less effective and efficient:

- RCF has a high spatial resolution in two dimensions, is easy to use and has been shown to be independent of dose rate for FLASH electrons [50], but requires a post-irradiation pause of at least 12 hours [42, 48, 49].

- Alanine uses electron paramagnetic resonance to determine the concentration of radicals produced in the material under irradiation. It can withstand very high doses, and is dose rate-independent with doses below 5 kGy [53], but the signal-to-noise ratio decreases at low doses. It also requires specialised readout equipment

which is time-consuming. Additionally, its small size and shape makes it difficult to determine beam profile information.

- Calorimeters directly measure the increase in temperature in the material due to irradiation. They are typically made of water or graphite [42]. Although simple in theory and independent of the dose rate, they require careful temperature control and very precise instruments to accurately measure temperatures with μK-resolution. Translating them into the clinic for routine use is technically very challenging [54].

With the aim of providing a low-cost, compact and easy to use dosimetry method, capable of delivering real-time dose measurements, we have investigated in depth a novel chemical-based fluorescence dosimeter. It uses the weakly fluorescent dye resazurin [117–120], which reduces to the highly fluorescent pink molecule, resorufin, under irradiation. This method was tested using X-rays alongside a Fricke dosimeter, using γ-rays from a Cs-137 radioactive source at the Commissariat à l'Énergie Atomique et aux Énergies Alternatives (CEA), and with very high energy electrons (VHEEs) of $\sim$200 MeV produced at CERN's CLEAR linear accelerator facility, and calibrated using RCF. In addition to its direct response to dose for these irradiation modalities, the preparation and handling procedures were thoroughly scrutinised to provide a rigorous framework for future studies using this chemical dosimeter.

After an initial experimental run at CLEAR, it was found that for UHDR VHEEs, the resazurin chemical dosimeter fluorescence increased linearly with doses up to 500 Gy. It was found that the repeatability of the experiment was not satisfactory, which was found to be due to misalignment of the small VHEE beam ($\sigma = 1 - 1.5$ mm) and the volume of the solution irradiated by the excitation LED. This was the most significant limiting factor of the experimental set-up, and we believe that by stirring the solution, it can be homogenised, resulting in more repeatable measurements. Another conclusion of the study was that the bubbling method used to purge the solution of oxygen was not effective, but by sealing the solution during the procedure it would yield a greater scavenging capacity of the solution, and thus more accurate results.

The aim post-experiment was to investigate these issues further, and obtain a more robust methodology for future experiments.

Studies at SCAPA were performed on various physical aspects of the chemical solution. These included the age of the solution, the time spent bubbling (de-aerating), and the time between preparation and irradiation. These parameters were varied and the solutions irradiated with identical doses (5.38 Gy) of X-rays. All three were found to impact the change in fluorescence signal strength for a given dose. It was concluded that for optimum results using this dosimeter, the solution should be freshly made, and irradiated as quickly as possible after preparation to prevent contamination, and it should be bubbled for as long as possible (subject to time available for a given experiment).

Studies were then undertaken at the CEA using γ-rays from a Cs-137 source. The irradiated solutions were analysed using two methods of fluorescence spectroscopy: a compact spectrometer connected to our experimental set-up, and a table-top spectrometer belonging to the LIDYL group at the CEA, and the two were found to be in excellent agreement. The initial concentration of resazurin was changed from 19.9 μM (the concentration used in all other experiments) to 17.91 μM, and this decrease of 10% was found to increase the amount of fluorescence produced for a given dose. Absorption spectroscopy data showed that this was due to the decreased absorption of the 585 nm fluorescent photons. The set-up of the dosimeter was tested, and various components modified or moved while measuring spectra. Individually, these had a minor effect on the data, but in combination could reduce the measured signal by as much as 12.5%. Ensuring that the dosimeter area is set-up consistently and minimising movement of attached components results in the greatest signal-to-noise ratio.

Multiple samples of resazurin solution were irradiated over a several month period to obtain a calibration curve. It was found that the solution should be pre-irradiated with a dose of 12.5 Gy. Beyond this value the fluorescence increases linearly with dose, until 65 Gy where the fluorescence decays as the resorufin is reduced to hydroresorufin. Absorption measurements performed in parallel with fluorescence spectroscopy found that the absorption at the resorufin excitation and emission wavelengths (530 nm and

585 nm, respectively) contributed to the dosimeter response.

By manually emulating the conversion of resazurin for resorufin, it was concluded that the assumption of a one-to-one molecular conversion is over-simplistic, because there are several competing chemical processes. These mechanisms should be investigated further to fully understand the dosimeter solution. Nonetheless, the solution could be used for γ-ray irradiation (over the entire solution) up to 65 Gy, and is very sensitive at low doses. This would be very useful for clinical radiotherapy fractions that are typically below 2 Gy.

Following the first CLEAR experiment (see Chapter 3), it was evident that the procedure for using our dosimeter had to be improved. The results were not very repeatable, and this issue was exacerbated when a small beam was used. However, at higher doses the dosimeter was more reliable. Given the variability of the beam position with respect to the cuvettes and the sensitivity of the chemicals to oxygen content, we believed the primary reasons for the inconsistent data was due to the geometry of the system, and the use of an inefficient de-aeration method. For the second CLEAR experiment the excitation LED axis was rotated 90° to be parallel to the VHEE beam axis and perpendicular to the optical fibre opening which transports the fluorescence to the spectrometer. This change reduced the amount of reabsorption of the 585 nm photons by the solution, giving more accurate spectral readings. The bubbling procedure was also improved from the previous run, improving the scavenging capacity of the resazurin. The results following these changes yielded far fewer null results than the first CLEAR experiment, and greater consistency from sample-to-sample. However, the overall repeatability was not yet ideal. This is believed to be primarily due to the lack of stirring in the solutions (stirring was intended during this experimental run but the stirring apparatus was lost in transit and no suitable replacements were available). Simulations were run to compare the approximate distances of the VHEE beam through each sample, and estimate the time required for the produced resorufin to diffuse this distance. In all samples this time was much greater than the time between irradiation and spectral analysis. The dose saturation level was found to be between 2,000 Gy and 4,000 Gy, a factor of around 30 – 60 times greater than that for the γ-ray studies.

Three explanations for this are proposed: a dose-rate effect, the different densities of ionisation tracks in the medium for the two modalities, and the increased abundance of low energy secondary electrons produced during VHEE irradiation. These areas should be investigated further to confirm the source of this large difference in saturation dose. A third experimental run at CLEAR was scheduled to test the stirrers lost in the previous run, and when tested, the increase in fluorescence became much more repeatable at high doses. Because the stirrers were not tested at low doses, irradiation with VHEEs should be repeated with stirrers at low doses, and at greater doses to determine the saturation dose with this set-up.

The data obtained supports the assertion that the chemical dosimeter can be a viable, real-time option for FLASH studies. Its strengths and weakness are listed along side those of other widely-used dosimeters in Table 8.1.

A further experiment conducted during the second CLEAR run was to investigate magnetically focusing the VHEE beam with quadrupoles to concentrate the dose in a small volume. Our study was the first to achieve focusing in two dimensions at a depth of 20 cm into a water phantom. The experimental on-axis dose through the phantom was measured with radiochromic film and compared with FLUKA simulations. By focusing the VHEEs in the phantom, the dose deposited is more concentrated in a region a few cm from the phantom entrance. This reduces both entrance and exit doses when compared with a collimated beam. As the focusing procedure is very time-consuming, a further study would be beneficial to optimise the focusing. The final focusing quadrupole could also be positioned closer to the phantom entrance, which would allow a tighter focus and thus better dose concentration. The ability to focus VHEEs – even very simply as we have shown here – allows users to increase the efficacy of VHEE radiotherapy, and target tumours deeper into a patient than possible with a collimated electron beam.

In addition to our dosimetry study at CLEAR, a collaborative study with UWS was conducted in parallel to detect 511 keV photons emitted following the decay of ^{15}O. Our results demonstrate that with a simple set up at the end of the VHEE beamline,

one can detect these emitted photons accurately and reliably, and the photon count scales linearly with the dose delivered. This very simple technique could be employed to study hypoxic tumours and provide a non-invasive, oxygen-sensitive imaging method which could help further elucidate the underlying mechanisms at play during FLASH radiotherapy.

8.2 Future outlook

There is still a great deal to learn about the resazurin chemical dosimeter and the underlying mechanisms. The cause of the vastly different saturation doses of γ-ray and VHEE irradiation is still unknown, although three potential explanations have been proposed. These should be explored alongside other irradiation modalities such as X-rays and protons to determine the limits of the dosimeter. Ideally, a dosimeter should be useable for all radiotherapy modalities, and if its response varies between modalities it should be well understood, predictable and repeatable. Additionally, the chemical processes occurring in the solution during irradiation should be elucidated. We have demonstrated that it is not simply a one-to-one conversion of a resazurin molecule for a resorufin molecule at the expense of one oxygen atom. These additional, unknown chemical reactions significantly affect the absorption spectrum of the solution, and therefore have an impact on the fluorescence, which is the means to determine the dose. This uncertainty should be well known if this dosimeter is to be more widely used. The 585 nm fluorescence emitted by the resorufin in the solution has been shown to increase linearly with dose when the solution is stirred. However, we have established that for VHEEs, the dosimeter can measure doses up to at least 12.5 kGy. The upper and lower limits of this linearity has not been determined, therefore the true dynamic range of this dosimeter should be studied further.

A dedicated experiment for a VHEE beam focused in both the x and y-axes would be extremely useful to fully demonstrate the benefits of concentrating the dose and increasing the penetration depth for radiotherapy. Focused VHEEs are able to achieve FLASH dose rates, and are much easier to produce and guide than protons, and, unlike photons, they don't require any optical components to be in the beam path. By

improving the focusing parameters, this would open the door to more effective UHDR radiotherapy and future FLASH studies.

Furthermore, a dedicated experimental run for the 511 keV photon detection will take place by the end of 2025, and this will be a valuable step towards having a non-invasive imaging modality that can be performed in parallel with beam delivery. This imaging technique will be sensitive to oxygen concentration and we believe that it will be a useful tool for distinguishing between healthy tissue, and hypoxic tumour tissue. By monitoring the oxygen content during UHDR irradiation, it will give a better understanding of the causes of the FLASH effect.

Dosimeter	Advantages	Disadvantages
Resazurin solution	Real-time dose readouts Large dynamic range with VHEE Inexpensive Sensitive at low doses Could be absolute	Sensitive to contaminants Mechanisms not fully understood Requires careful preparation
Fricke solution	Absolute dosimeter Could provide spatial dose information	Not real-time Time-consuming Not simple to use Sensitive to low dose rates
Radiochromic film	High spatial resolution High dynamic range Dose-rate independent Tissue-equivalent material Inexpensive Minimally perturbative for electrons, photons and protons	Not real-time Under-response with high-LET radiation Reference dosimeter
Alanine	Dose rate independent Very large dynamic range Dose rate independent Absolute dosimeter	Requires specialised readout equipment Low spatial resolution Low SNR at low doses Temperature and humidity sensitive
Calorimeter	Real-time Absolute	Requires precise instrumentation No spatial dose information Bulky Correction factors
Ionisation chamber	Real-time Precise Absolute	Significant errors at UHDRs Bulky High voltage

Table 8.1: The main advantages and disadvantages of commonly used dosimetry methods compared with our resazurin-based fluorescence dosimeter.

Appendix A

Diffusion of resorufin in water

A.1 Derivation of diffusion equation

When considering a slab of diffusing particles of depth, dx, and face area, A, the number of particles, N, at some position, x, will be:

$$N = cAN_A dx, \tag{A.1}$$

where c is the molar concentration of the particle an N_A is Avogadro's constant.

Dividing this by the total number of particles, N_0, yields the probability, P, that any of these diffusing particles are in the slab:

$$P = \frac{cAN_A dx}{N_0}. \tag{A.2}$$

If the particle is in the slab, it will have travelled some distance, x, from the origin, therefore, the mean distance travelled, $\langle x \rangle$ by all diffusing particles is the sum of each distance, weighted by the probability of its occurrence, P, giving:

$$\langle x \rangle = \int_0^\infty x \frac{cAN_A}{N_0} dx. \tag{A.3}$$

However, since the particles travel in all radial directions (both positive and negative), taking the mean distance would result in a value of zero. Therefore, the root

mean square must be taken:

$$\langle x^2 \rangle^{1/2} = \sqrt{\int_0^\infty x^2 \frac{cAN_A}{N_0} dx} = \sqrt{\frac{cAN_A}{N_0} \int_0^\infty x^2 dx}, \tag{A.4}$$

The concentration, c, is a function of position, x, and time, t, and can be written:

$$c(x,t) = \frac{n_0}{A(\pi D_{rate} t)^{1/2}} e^{-x^2/4D_{rate}t}, \tag{A.5}$$

where n_0 is the total amount of particles (in moles) and D_{rate} is the diffusion coefficient. This means Equation A.4 can be rewritten as:

$$\langle x^2 \rangle^{1/2} = \sqrt{\frac{n_0 AN_A}{A(\pi D_{rate} t)^{1/2} N_0} \int_0^\infty x^2 e^{-x^2/4D_{rate}t}} = \sqrt{\frac{1}{(\pi D_{rate} t)^{1/2}} \left[2\pi^{1/2} (D_{rate} t)^{3/2}\right]}, \tag{A.6}$$

since $N_0 = n_0 N_A$. This then simplifies, rewriting $\langle x^2 \rangle^{1/2}$ as the diffusion length, x, to give the equation

$$x = \sqrt{2D_{rate} t}, \tag{A.7}$$

or

$$t = \frac{x^2}{2D_{rate}}, \tag{A.8}$$

as used in Chapter 5.2.2.

A.2 Determining the diffusion coefficient of resorufin

To determine the diffusion coefficient of resorufin, values for other molecules were taken from Atkins' Physical Chemistry [150] and plotted against their molecular weights. These values are shown in Table A.1 and plotted in Figure A.1. The figure shows a fit following the power law equation: $D_{rate} = 1.6 \times 10^{-4} M^{-0.726}$, where D_{rate} is the diffusion coefficient and M is the molecular weight. Using this equation, the diffusion coefficient for resorufin ($C_{12}H_7NO_3$, M = 213.19 g/mol) comes out to be 6.31×10^{-6} cm^2/s.

Molecule	Molecular weight, M [g/mol]	Diffusion coefficient, D_{rate} [cm^2/s]
Glycine ($C_2H_5NO_2$)	75.07	1.06×10^{-5}
Dextrose ($C_6H_{12}O_6$)	180.2	6.73×10^{-6}
Sucrose ($C_{12}H_{22}O_{11}$)	342.3	5.22×10^{-6}
Water (H_2O)	18.02	2.26×10^{-5}
Methanol (CH_3OH)	32.04	1.58×10^{-5}
Ethanol (C_2H_5OH)	46.07	1.24×10^{-5}

Table A.1: Molecular weights and diffusion coefficients for a range of molecules taken from Atkins [150], used to estimate the diffusion coefficient of resorufin ($C_{12}H_7NO_3$, M = 213.19 g/mol)

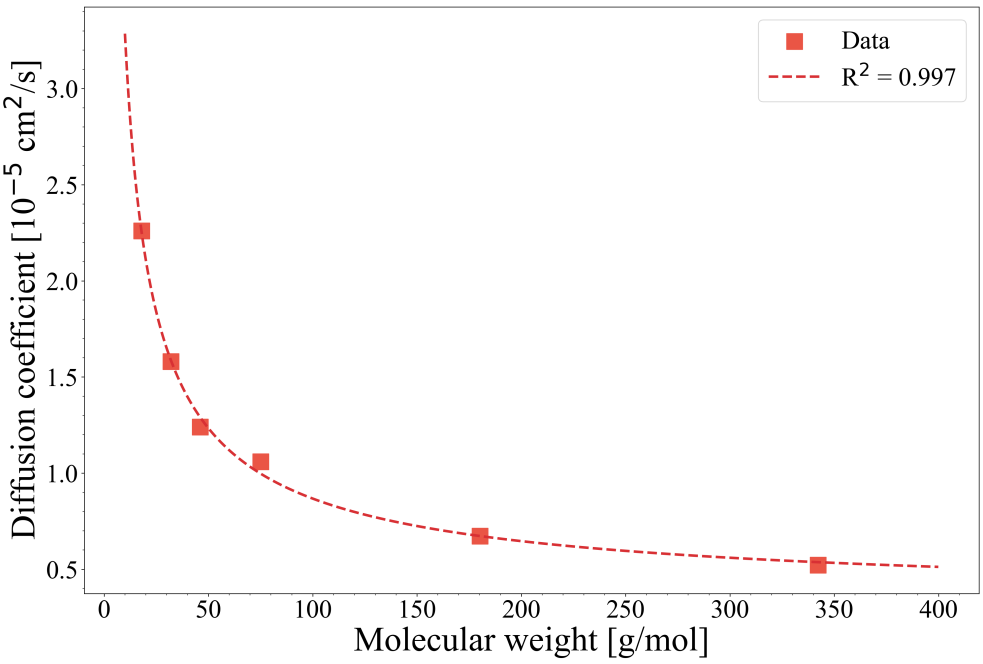

Figure A.1: Data from Table A.1 fitted to a power law: $y = 1.6 \times 10^{-4} x^{-0.726}$. Using this fit the diffusion coefficient of resorufin is 6.31×10^{-6} cm^2/s.

Bibliography

[1] Henderson B, Dougherty T, Schwartz S, et al. Historical perspective. Photodynamic Therapy: Basic Principles and Clinical Applications BW Henderson, TJ Dougherty(eds) Marcel Decker: New York. 1992:1-15.

[2] De Moulin D. A short history of breast cancer. Springer Science & Business Media; 1983.

[3] Kevles B. Naked to the bone: Medical imaging in the twentieth century. Rutgers University Press; 1997.

[4] van Zuylen J. The microscopes of Antoni van Leeuwenhoek. Journal of microscopy. 1981;121(3):309-28.

[5] Simpson JY. On a new anaesthetic agent, more efficient than sulphuric ether. The Lancet. 1847;50(1264):549-50.

[6] Lister J. On the antiseptic principle in the practice of surgery. British medical journal. 1867;2(351):246.

[7] Pasteur L. On the germ theory. Science. 1881;(62):420-2.

[8] Röntgen W. Über eine neue Art von Strahlen. Sitzungsberichte der Würzburger Physik-Medic-Gesellschaft. 1895;137:132-41.

[9] Curie P. Sur une nouvelle substance fortement radioactive, contenue dans la pechblende. Comptes rendus de 1'Academie des Sciences, Paris. 1898;127:1215-7.

[10] Regaud C, Ferroux R. Discordance of X-ray effects, on the one hand in the testicle, through the skin, on the other hand in the fractionation of the dose. Compt Rend Soc Biol. 1927;97:431-4.

[11] Clarke R, Valentin J. A history of the international commission on radiological protection. Health physics. 2005;88(5):407-22.

[12] Thwaites DI, Tuohy JB. Back to the future: the history and development of the clinical linear accelerator. Physics in medicine & biology. 2006;51(13):R343.

[13] Tobias C, Lawrence J, Born J, McCombs R, Roberts J, Anger H, et al. Pituitary irradiation with high-energy proton beams a preliminary report. Cancer research. 1958;18(2):121-34.

[14] Ronga MG, Cavallone M, Patriarca A, Leite AM, Loap P, Favaudon V, et al. Back to the future: very high-energy electrons (VHEEs) and their potential application in radiation therapy. Cancers. 2021;13(19):4942.

[15] Gizzi LA, Andreassi MG. Ready for translational research. Nature Physics. 2022;18(3):237-8.

[16] Hall EJ. Cancer caused by x-rays—a random event? The lancet oncology. 2007;8(5):369-70.

[17] Barcellos-Hoff MH, Park C, Wright EG. Radiation and the microenvironment–tumorigenesis and therapy. Nature Reviews Cancer. 2005;5(11):867-75.

[18] Liermann J, Shinoto M, Syed M, Debus J, Herfarth K, Naumann P. Carbon ion radiotherapy in pancreatic cancer: a review of clinical data. Radiotherapy and Oncology. 2020;147:145-50.

[19] Leibel S, Phillips T. Textbook of Radiation Oncology; 2005.

[20] Gotoh E, Durante M. Chromosome condensation outside of mitosis: mechanisms and new tools. Journal of cellular physiology. 2006;209(2):297-304.

[21] Natarajan AT. Chromosome aberrations: past, present and future. Mutation Research/Fundamental and Molecular Mechanisms of Mutagenesis. 2002;504(1-2):3-16.

[22] Hughes JR, Parsons JL. FLASH radiotherapy: Current knowledge and future insights using proton-beam therapy. International journal of molecular sciences. 2020;21(18):6492.

[23] Brown A, Suit H. The centenary of the discovery of the Bragg peak. Radiotherapy and Oncology. 2004;73(3):265-8.

[24] Hornsey S, Bewley D. Hypoxia in mouse intestine induced by electron irradiation at high dose-rates. International Journal of Radiation Biology and Related Studies in Physics, Chemistry and Medicine. 1971;19(5):479-83.

[25] Field S, Bewley D. Effects of dose-rate on the radiation response of rat skin. International Journal of Radiation Biology and Related Studies in Physics, Chemistry and Medicine. 1974;26(3):259-67.

[26] Hendry JH, Moore JV, Hodgson B, Keene J. The constant low oxygen concentration in all the target cells for mouse tail radionecrosis. Radiation research. 1982;92(1):172-81.

[27] Favaudon V, Caplier L, Monceau V, Pouzoulet F, Sayarath M, Fouillade C, et al. Ultrahigh dose-rate FLASH irradiation increases the differential response between normal and tumor tissue in mice. Science translational medicine. 2014;6(245):245ra93-3.

[28] Loo BW, Schuler E, Lartey FM, Rafat M, King GJ, Trovati S, et al. (P003) delivery of ultra-rapid flash radiation therapy and demonstration of normal tissue sparing after abdominal irradiation of mice. International Journal of Radiation Oncology* Biology* Physics. 2017;98(2):E16.

[29] Montay-Gruel P, Petersson K, Jaccard M, Boivin G, Germond JF, Petit B, et al. Irradiation in a flash: Unique sparing of memory in mice after whole

brain irradiation with dose rates above 100 Gy/s. Radiotherapy and Oncology. 2017;124(3):365-9.

[30] Levy K, Natarajan S, Wang J, Chow S, Eggold J, Loo P, et al. FLASH irradiation enhances the therapeutic index of abdominal radiotherapy in mice. bioRxiv. 2019.

[31] Vozenin MC, De Fornel P, Petersson K, Favaudon V, Jaccard M, Germond JF, et al. The advantage of FLASH radiotherapy confirmed in mini-pig and cat-cancer patients. Clinical Cancer Research. 2019;25(1):35-42.

[32] Montay-Gruel P, Acharya MM, Petersson K, Alikhani L, Yakkala C, Allen BD, et al. Long-term neurocognitive benefits of FLASH radiotherapy driven by reduced reactive oxygen species. Proceedings of the National Academy of Sciences. 2019;116(22):10943-51.

[33] Bourhis J, Sozzi WJ, Jorge PG, Gaide O, Bailat C, Duclos F, et al. Treatment of a first patient with FLASH-radiotherapy. Radiotherapy and oncology. 2019;139:18-22.

[34] Jin JY, Gu A, Wang W, Oleinick NL, Machtay M, (Spring) Kong FM. Ultra-high dose rate effect on circulating immune cells: A potential mechanism for FLASH effect? Radiotherapy and Oncology. 2020;149:55-62.

[35] Pardoll DM. The blockade of immune checkpoints in cancer immunotherapy. Nature Reviews Cancer. 2012;12(4):252-64.

[36] Lee Y, Auh SL, Wang Y, Burnette B, Wang Y, Meng Y, et al. Therapeutic effects of ablative radiation on local tumor require CD8+ T cells: changing strategies for cancer treatment. Blood. 2009;114(3):589-95.

[37] Antonia SJ, Villegas A, Daniel D, Vicente D, Murakami S, Hui R, et al. Durvalumab after chemoradiotherapy in stage III non–small-cell lung cancer. New England Journal of Medicine. 2017;377(20):1919-29.

[38] Wirsdörfer F, Jendrossek V. The role of lymphocytes in radiotherapy-induced adverse late effects in the lung. Frontiers in immunology. 2016;7:591.

[39] Kong FMS, Wang S. Nondosimetric Risk Factors for Radiation-Induced Lung Toxicity. Seminars in Radiation Oncology. 2015;25(2):100-9. Non-Small Cell Lung Cancer. Available from: https://www.sciencedirect.com/science/article/pii/S1053429614001192.

[40] Stenmark MH, Cai XW, Shedden K, Hayman JA, Yuan S, Ritter T, et al. Combining physical and biologic parameters to predict radiation-induced lung toxicity in patients with non-small-cell lung cancer treated with definitive radiation therapy. International Journal of Radiation Oncology* Biology* Physics. 2012;84(2):e217-22.

[41] ICRU. Determination of absorbed dose in a patient irradiated by beams of X or gamma rays in radiotherapy procedures ICRU report 24; 1987.

[42] Darafsheh A. Radiation therapy dosimetry: a practical handbook. CRC Press; 2021.

[43] McManus M, Romano F, Lee N, Farabolini W, Gilardi A, Royle G, et al. The challenge of ionisation chamber dosimetry in ultra-short pulsed high dose-rate Very High Energy Electron beams. Scientific reports. 2020;10(1):9089.

[44] Bourgouin A, Schüller A, Hackel T, Kranzer R, Poppinga D, Kapsch RP, et al. Calorimeter for real-time dosimetry of pulsed ultra-high dose rate electron beams. Frontiers in Physics. 2020;8:567340.

[45] Kranzer R, Poppinga D, Weidner J, Schüller A, Hackel T, Looe HK, et al. Ion collection efficiency of ionization chambers in ultra-high dose-per-pulse electron beams. Medical physics. 2021;48(2):819-30.

[46] Petersson K, Jaccard M, Germond JF, Buchillier T, Bochud F, Bourhis J, et al. High dose-per-pulse electron beam dosimetry—A model to correct for the ion recombination in the Advanced Markus ionization chamber. Medical physics. 2017;44(3):1157-67.

[47] Di Martino F, Del Sarto D, Bisogni MG, Capaccioli S, Galante F, Gasperini A, et al. A new solution for UHDP and UHDR (Flash) measurements: Theory and conceptual design of ALLS chamber. Physica Medica. 2022;102:9-18.

[48] León-Marroquín EY, Mulrow D, Darafsheh A, Khan R. Response characterization of EBT-XD radiochromic films in megavoltage photon and electron beams. Medical physics. 2019;46(9):4246-56.

[49] León-Marroquín EY, Mulrow DJ, Khan R, Darafsheh A. Spectral analysis of the EBT3 radiochromic films for clinical photon and electron beams. Medical physics. 2019;46(2):973-82.

[50] Patriarca A, Fouillade C, Auger M, Martin F, Pouzoulet F, Nauraye C, et al. Experimental set-up for FLASH proton irradiation of small animals using a clinical system. International Journal of Radiation Oncology* Biology* Physics. 2018;102(3):619-26.

[51] Darafsheh A, León-Marroquín EY, Mulrow DJ, Baradaran-Ghahfarokhi M, Zhao T, Khan R. On the spectral characterization of radiochromic films irradiated with clinical proton beams. Physics in Medicine & Biology. 2019;64(13):135016.

[52] Darafsheh A, Zhao T, Khan R. Spectroscopic analysis of EBT-XD radiochromic films irradiated with proton and photon therapy beams. Phys Med Biol. 2020;65(20):205002.

[53] Organization IS, International A. Standard Practice for Use of an Alanine-EPR Dosimetry System.. ASTM International, ISO and West Conshohocken (US: PA) Geneva, Switzerland; 2013.

[54] Seuntjens J, Duane S. Photon absorbed dose standards. Metrologia. 2009;46(2):S39.

[55] Romano F, Bailat C, Jorge PG, Lerch MLF, Darafsheh A. Ultra-high dose rate dosimetry: challenges and opportunities for FLASH radiation therapy. Medical physics. 2022;49(7):4912-32.

[56] Giguère C, Hart A, Bateman J, Korysko P, Farabolini W, LeChasseur Y, et al. Real-time Plastic Scintillation Dosimetry of Ultra-High Dose Rate Very High Energy Electrons (VHEE) at CERN CLEAR Facility. In: Journal of Physics: Conference Series. vol. 2799. IOP Publishing; 2024. p. 012016.

[57] Bjegovic K, Sun L, Pandey P, Grilj V, Ballesteros-Zebadua P, Paisley R, et al. 4D in vivo dosimetry for a FLASH electron beam using radiation-induced acoustic imaging. Physics in Medicine & Biology. 2024;69(11):115053.

[58] Marinelli M, Felici G, Galante F, Gasparini A, Giuliano L, Heinrich S, et al. Design, realization, and characterization of a novel diamond detector prototype for FLASH radiotherapy dosimetry. Medical Physics. 2022;49(3):1902-10.

[59] Aad G, Abajyan T, Abbott B, Abdallah J, Khalek SA, Abdelalim AA, et al. Observation of a new particle in the search for the Standard Model Higgs boson with the ATLAS detector at the LHC. Physics Letters B. 2012;716(1):1-29.

[60] Abbott BP, Abbott R, Abbott T, Abernathy M, Acernese F, Ackley K, et al. Observation of gravitational waves from a binary black hole merger. Physical review letters. 2016;116(6):061102.

[61] Planck M. On the law of distribution of energy in the normal spectrum. Annalen der physik. 1901;4(553):1.

[62] Einstein A. Does the inertia of a body depend upon its energy-content. Ann Phys. 1905;18:639-41.

[63] Wille K. The Physics of Particle Accelerators: An Introduction. Clarendon Press; 2000.

[64] Wangler TP. RF Linear Accelerators. John Wiley & Sons; 2008.

[65] Jaffray D, Battista J, Fenster A, Munro P. X-ray sources of medical linear accelerators: focal and extra-focal radiation. Medical physics. 1993;20(5):1417-27.

[66] Hogstrom KR, Almond PR. Review of electron beam therapy physics. Physics in Medicine & Biology. 2006;51(13):R455.

[67] Levin W, Kooy H, Loeffler J, DeLaney T. Proton beam therapy. British journal of Cancer. 2005;93(8):849-54.

[68] Robin Wang PNG. Plasma Acceleration The compact accelerators of the future; 2025. Accessed: 2025-02-03. https://groups.physics.ox.ac.uk/norreys/ResearchWakefield.html.

[69] Tajima T, Dawson JM. Laser electron accelerator. Physical Review Letters. 1979;43(4):267.

[70] Akhiezer AI, Polovin R. Theory of wave motion of an electron plasma. Soviet Phys JETP. 1956;3.

[71] Dawson JM. Nonlinear electron oscillations in a cold plasma. Physical review. 1959;113(2):383.

[72] Strickland D, Mourou G. Compression of amplified chirped optical pulses. Optics communications. 1985;56(3):219-21.

[73] Maine P, Strickland D, Bado P, Pessot M, Mourou G. Generation of ultrahigh peak power pulses by chirped pulse amplification. IEEE Journal of Quantum electronics. 1988;24(2):398-403.

[74] Ferray M, Lompré L, Gobert O, L'huillier A, Mainfray G, Manus C, et al. Multi-terawatt picosecond Nd-glass laser system at 1053 nm. Optics communications. 1990;75(3-4):278-82.

[75] Perry MD, Mourou G. Terawatt to petawatt subpicosecond lasers. Science. 1994;264(5161):917-24.

[76] Gorbunov L, Kirsanov V. Excitation of plasma waves by an electromagnetic wave packet. Sov Phys JETP. 1987;66(2):290-4.

[77] Sprangle P, Joyce G, Esarey E, Ting A. Laser wakefield acceleration and relativstic optical guiding. In: AIP Conference Proceedings. vol. 175. American Institute of Physics; 1988. p. 231-9.

[78] Hamster H, Sullivan A, Gordon S, White W, Falcone R. Subpicosecond, electromagnetic pulses from intense laser-plasma interaction. Physical review letters. 1993;71(17):2725.

[79] Mangles SP, Murphy C, Najmudin Z, Thomas AGR, Collier J, Dangor AE, et al. Monoenergetic beams of relativistic electrons from intense laser–plasma interactions. Nature. 2004;431(7008):535-8.

[80] Geddes C, Toth C, Van Tilborg J, Esarey E, Schroeder C, Bruhwiler D, et al. High-quality electron beams from a laser wakefield accelerator using plasma-channel guiding. Nature. 2004;431(7008):538-41.

[81] Faure J, Rechatin C, Norlin A, Lifschitz A, Glinec Y, Malka V. Controlled injection and acceleration of electrons in plasma wakefields by colliding laser pulses. Nature. 2006;444(7120):737-9.

[82] Hafz NA, Jeong TM, Choi IW, Lee SK, Pae KH, Kulagin VV, et al. Stable generation of GeV-class electron beams from self-guided laser–plasma channels. Nature Photonics. 2008;2(9):571-7.

[83] Clayton CE, Ralph J, Albert F, Fonseca R, Glenzer S, Joshi C, et al. Self-guided laser wakefield acceleration beyond 1 GeV using ionization-induced injection. Physical review letters. 2010;105(10):105003.

[84] Lu H, Liu M, Wang W, Wang C, Liu J, Deng A, et al. Laser wakefield acceleration of electron beams beyond 1 GeV from an ablative capillary discharge waveguide. Applied Physics Letters. 2011;99(9):091502.

[85] Kim HT, Pae KH, Cha HJ, Kim IJ, Yu TJ, Sung JH, et al. Enhancement of electron energy to the multi-GeV regime by a dual-stage laser-wakefield accelerator pumped by petawatt laser pulses. Physical review letters. 2013;111(16):165002.

[86] Leemans W, Gonsalves A, Mao HS, Nakamura K, Benedetti C, Schroeder C, et al. Multi-GeV electron beams from capillary-discharge-guided subpetawatt laser pulses in the self-trapping regime. Physical review letters. 2014;113(24):245002.

[87] Kim HT, Pathak V, Pae KH, Lifschitz A, Sylla F, Shin JH, et al. Stable multi-GeV electron accelerator driven by waveform-controlled PW laser pulses. Scientific reports. 2017;7(1):1-8.

[88] Gonsalves A, Nakamura K, Daniels J, Benedetti C, Pieronek C, De Raadt T, et al. Petawatt laser guiding and electron beam acceleration to 8 GeV in a laser-heated capillary discharge waveguide. Physical review letters. 2019;122(8):084801.

[89] Boyd T, Boyd T, Sanderson J. The Physics of Plasmas. Cambridge University Press; 2003.

[90] Albert F, Thomas AG. Applications of laser wakefield accelerator-based light sources. Plasma Physics and Controlled Fusion. 2016;58(10):103001.

[91] Manahan GG. Studies of transverse properties of relativistic electrons from laser wakefield accelerator. University of Strathclyde; 2013.

[92] Esarey E, Schroeder C, Leemans W. Physics of laser-driven plasma-based electron accelerators. Reviews of modern physics. 2009;81(3):1229.

[93] Umstadter D, Kim J, Dodd E. Laser injection of ultrashort electron pulses into wakefield plasma waves. Physical review letters. 1996;76(12):2073.

[94] Esarey E, Hubbard R, Leemans W, Ting A, Sprangle P. Electron injection into plasma wakefields by colliding laser pulses. Physical Review Letters. 1997;79(14):2682.

[95] Chen M, Sheng ZM, Ma YY, Zhang J. Electron injection and trapping in a laser wakefield by field ionization to high-charge states of gases. Journal of applied physics. 2006;99(5).

[96] Pak A, Marsh K, Martins S, Lu W, Mori W, Joshi C. Injection and trapping of tunnel-ionized electrons into laser-produced wakes. Physical review letters. 2010;104(2):025003.

[97] McGuffey C, Thomas A, Schumaker W, Matsuoka T, Chvykov V, Dollar F, et al. Ionization induced trapping in a laser wakefield accelerator. Physical review letters. 2010;104(2):025004.

[98] Hosokai T, Kinoshita K, Zhidkov A, Maekawa A, Yamazaki A, Uesaka M. Effect of External Static Magnetic Field on the Emittance and Total Charge¡? format?¿ of Electron Beams Generated by Laser-Wakefield Acceleration. Physical review letters. 2006;97(7):075004.

[99] Froula D, Divol L, Davis P, Palastro J, Michel P, Leurent V, et al. Magnetically controlled plasma waveguide for laser wakefield acceleration. Plasma Physics and Controlled Fusion. 2009;51(2):024009.

[100] Vieira J, Martins J, Pathak V, Fonseca R, Mori W, Silva L. Magnetically assisted self-injection and radiation generation for plasma-based acceleration. Plasma Physics and Controlled Fusion. 2012;54(12):124044.

[101] Malka V. Plasma wake accelerators: introduction and historical overview. arXiv preprint arXiv:170509584. 2017.

[102] Faure J, Glinec Y, Pukhov A, Kiselev S, Gordienko S, Lefebvre E, et al. A laser–plasma accelerator producing monoenergetic electron beams. Nature. 2004;431(7008):541-4.

[103] Sprangle P, Esarey E, Ting A, Joyce G. Laser wakefield acceleration and relativistic optical guiding. In: AIP Conference Proceedings. vol. 193. American Institute of Physics; 1989. p. 376-87.

[104] Esarey E, Pilloff M. Trapping and acceleration in nonlinear plasma waves. Physics of Plasmas. 1995;2(5):1432-6.

[105] Thomas A, Mangles S, Najmudin Z, Kaluza M, Murphy C, Krushelnick K. Measurements of wave-breaking radiation from a laser-wakefield accelerator. Physical review letters. 2007;98(5):054802.

[106] Esarey E, Schroeder C, Leemans W, Hafizi B. Laser-induced electron trapping in plasma-based accelerators. Physics of Plasmas. 1999;6(5):2262-8.

[107] Fubiani G, Esarey E, Schroeder C, Leemans W. Beat wave injection of electrons into plasma waves using two interfering laser pulses. Physical Review E. 2004;70(1):016402.

[108] Geddes C, Nakamura K, Plateau G, Toth C, Cormier-Michel E, Esarey E, et al. Plasma-density-gradient injection of low absolute-momentum-spread electron bunches. Physical review letters. 2008;100(21):215004.

[109] Tooley M, Ersfeld B, Yoffe S, Noble A, Brunetti E, Sheng Z, et al. Towards attosecond high-energy electron bunches: Controlling self-injection in laser-wakefield accelerators through plasma-density modulation. Physical review letters. 2017;119(4):044801.

[110] Islam M, Brunetti E, Shanks R, Ersfeld B, Issac R, Cipiccia S, et al. Near-threshold electron injection in the laser–plasma wakefield accelerator leading to femtosecond bunches. New Journal of Physics. 2015;17(9):093033.

[111] Chen M, Esarey E, Schroeder C, Geddes C, Leemans W. Theory of ionization-induced trapping in laser-plasma accelerators. Physics of Plasmas. 2012;19(3).

[112] Thaury C, Guillaume E, Lifschitz A, Ta Phuoc K, Hansson M, Grittani G, et al. Shock assisted ionization injection in laser-plasma accelerators. Scientific reports. 2015;5(1):16310.

[113] Fricke H, Morse S. The chemical action of roentgen rays on dilute ferrosulphate solutions as a measure of dose. Am J Roentgenol Radium Therapy Nucl Med. 1927;18:430-2.

[114] Fricke H, Morse S. XIII. The action of X-rays on ferrous sulphate solutions. The London, Edinburgh, and Dublin Philosophical Magazine and Journal of Science. 1929;7(41):129-41.

[115] Shortt KR. Fundamentals of Fricke Dosimetry. DOSGEL 2001. 2001;2001(2nd):10.

[116] deAlmeida CE, Ochoa R, Lima MCd, David MG, Pires EJ, Peixoto JG, et al. A feasibility study of Fricke dosimetry as an absorbed dose to water standard for 192Ir HDR sources. PloS one. 2014;9(12):e115155.

[117] Pesch K, Simmert U. Combined assays for lactose and galactose by enzymatic reactions. Kieler Milchw Forsch. 1929;8:551.

[118] Anoopkumar-Dukie S, Carey J, Conere T, O'sullivan E, Van Pelt F, Allshire A. Resazurin assay of radiation response in cultured cells. The British journal of radiology. 2005;78(934):945-7.

[119] Hudman DA, Sargentini NJ. Resazurin-based assay for screening bacteria for radiation sensitivity. Springerplus. 2013;2(1):1-6.

[120] Nahas SA, Davies R, Fike F, Nakamura K, Du L, Kayali R, et al. Comprehensive profiling of radiosensitive human cell lines with DNA damage response assays identifies the neutral comet assay as a potential surrogate for clonogenic survival. Radiation research. 2012;177(2):176-86.

[121] Balcerzyk A, Baldacchino G. Implementation of laser induced fluorescence in a pulse radiolysis experiment–a new way to analyze resazurin-like reduction mechanisms. Analyst. 2014;139(7):1707-12.

[122] Chang R. Physical chemistry for the biosciences. University Science Books; 2005.

[123] Schmitt DM, O'Dee DM, Cowan BN, Birch JWM, Mazzella LK, Nau GJ, et al. The use of resazurin as a novel antimicrobial agent against Francisella tularensis. Frontiers in cellular and infection microbiology. 2013;3:93.

[124] Sjobak K, Adli E, Bergamaschi M, Burger S, Corsini R, Curcio A, et al. Status of the CLEAR electron beam user facility at CERN. Proc IPAC'19. 2019:983-6.

[125] AAT Bioquest I. Phosphate Buffer (pH 5.8 to 7.4) Preparation and Recipe; 2024. Accessed: 2024-12-12. https://www.aatbio.com/resources/buffer-preparations-and-recipes/phosphate-buffer-ph-5-8-to-7-4.

[126] Ashland™. GAFCHROMIC™ DOSIMETRY MEDIA, TYPE EBT-3;. Accessed: 2024-11-11. http://www.gafchromic.com/documents/EBT3_Specifications.pdf.

[127] Ashland™. GAFCHROMIC™ DOSIMETRY MEDIA, TYPE HD-V2;. Accessed: 2024-11-11. http://www.gafchromic.com/documents/gafchromic-hdv2.pdf.

[128] Izewska J, Rajan G. Radiation dosimeters. Radiation oncology physics: a handbook for teachers and students. 2005:71-99.

[129] Kumar D, Pradhan A, Chauhan V. Utilizing GAFCHROMIC EBT3 film for precise skin dosimetry in head and neck cancer patients. Journal of Radioanalytical and Nuclear Chemistry. 2024:1-10.

[130] Borca VC, Pasquino M, Russo G, Grosso P, Cante D, Sciacero P, et al. Dosimetric characterization and use of GAFCHROMIC EBT3 film for IMRT dose verification. Journal of applied clinical medical physics. 2013;14(2):158-71.

[131] Lambert JH. Photometria sive de mensura et gradibus luminis, colorum et umbrae. Sumptibus viduae Eberhardi Klett, typis Christophori Petri Detleffsen; 1760.

[132] Jaccard M, Durán MT, Petersson K, Germond JF, Liger P, Vozenin MC, et al. High dose-per-pulse electron beam dosimetry: commissioning of the Oriatron eRT6 prototype linear accelerator for preclinical use. Medical physics. 2018;45(2):863-74.

[133] Ashland™. GAFCHROMIC™ DOSIMETRY MEDIA, TYPE EBT-XD;. Accessed: 2024-11-11. http://www.gafchromic.com/documents/EBTXD_Specifications_Final.pdf.

[134] Barrett GB. The Coefficient of Determination: Understanding r squared and R squared. Mathematics Teacher. 2000;93(3):230-4.

[135] Kokurewicz KZ. Investigation of focused Very High Energy Electrons (VHEEs) as a new radiotherapy method [Doctoral Dissertation]. University of Strathclyde; 2020.

[136] Massillon-JL G, Muñoz-Molina ID, Díaz-Aguirre P. Optimum absorbed dose versus energy response of gafchromic EBT2 and EBT3 films exposed to 20–160 kV x-rays and 60Co gamma. Biomedical Physics & Engineering Express. 2016;2(4):045005.

[137] Delacroix D, P Guerre J, Leblanc P, Hickman C. Radionuclide and radiation protection data handbook 2002. Radiation protection dosimetry. 2002;98(1):1-168.

[138] Theratronics B. Gammacell® 1000 Elite / 3000 Elan Superior Performance and Unparalleled Dose Uniformity;. Available from: `http://www.theratronics.ca/PDFs/BT_MBTS_8005_GC1000E_3000E_5brochure_05132021.pdf`.

[139] Xing W, Yin M, Lv Q, Hu Y, Liu C, Zhang J. Oxygen solubility, diffusion coefficient, and solution viscosity. In: Rotating electrode methods and oxygen reduction electrocatalysts. Elsevier; 2014. p. 1-31.

[140] Klassen N, Shortt K, Seuntjens J, Ross C. Fricke dosimetry: the difference between g (fe3+) for 60co-rays and high-energy x-rays. Physics in Medicine & Biology. 1999;44(7):1609.

[141] Davies J, Law J. Practical aspects of ferrous sulphate dosimetry. Physics in Medicine & Biology. 1963;8(1):91.

[142] O'brien J, Wilson I, Orton T, Pognan F. Investigation of the Alamar Blue (resazurin) fluorescent dye for the assessment of mammalian cell cytotoxicity. European journal of biochemistry. 2000;267(17):5421-6.

[143] Uzarski JS, DiVito MD, Wertheim JA, Miller WM. Essential design considerations for the resazurin reduction assay to noninvasively quantify cell expansion within perfused extracellular matrix scaffolds. Biomaterials. 2017;129:163-75.

[144] Gao L, Zhang A. Low-dose radiotherapy effects the progression of anti-tumor response. Translational Oncology. 2023;35:101710.

[145] CERN. The official CERN FLUKA website; 2025. Accessed: 2025-07-22. `https://fluka.cern`.

[146] Battistoni G, Boehlen T, Cerutti F, Chin PW, Esposito LS, Fasso A, et al. Overview of the FLUKA code. Annals of Nuclear Energy. 2015;82:10-8.

[147] Battistoni G, Bauer J, Boehlen TT, Cerutti F, Chin MP, Dos Santos Augusto R, et al. The FLUKA code: an accurate simulation tool for particle therapy. Frontiers in oncology. 2016;6:116.

[148] Ahdida C, Bozzato D, Calzolari D, Cerutti F, Charitonidis N, Cimmino A, et al. New capabilities of the FLUKA multi-purpose code. Frontiers in Physics. 2022;9:788253.

[149] Harrison RL. Introduction to monte carlo simulation. In: AIP conference proceedings. vol. 1204; 2010. p. 17.

[150] Atkins P, De Paula J. Atkins' physical chemistry. Oxford university press; 2002.

[151] Hart E, Fielden E. Procedures in Radiation Dosimetry: Liquid Chemical Systems. The Hydrated Electron Dosimeter. 1970.

[152] Shin WG, Ramos-Mendez J, Faddegon B, Tran H, Villagrasa C, Perrot Y, et al. Evaluation of the influence of physical and chemical parameters on water radiolysis simulations under MeV electron irradiation using Geant4-DNA. Journal of Applied Physics. 2019;126(11).

[153] Bui A, Bekerat H, Childress L, Sankey J, Seuntjens J, Enger SA. Effects of incoming particle energy and cluster size on the G-value of hydrated electrons. Physica Medica. 2023;107:102540.

[154] Precek M, Kubelik P, Vysin L, Schmidhammer U, Larbre JP, Demarque A, et al. Dose rate effects in fluorescence chemical dosimeters exposed to picosecond electron pulses: An accurate measurement of low doses at high dose rates. Radiation Research. 2022;197(2):131-48.

[155] Hill M, Smith F. Is the response of the Fricke dosimeter constant for high energy electrons and photons? Radiation Physics and Chemistry. 1996;47(4):637-47.

[156] Vlachoudis V. flair for FLUKA. tech. rep., CERN; 2006.

[157] Podgorsak EB, et al. Review of radiation oncology physics: a handbook for teachers and students. Vienna, Austria: IAE Agency. 2003;19:133.

[158] Diamantopoulos S, Platoni K, Dilvoi M, Nazos I, Geropantas K, Maravelis G, et al. Clinical implementation of total skin electron beam (TSEB) therapy: a review of the relevant literature. Physica Medica. 2011;27(2):62-8.

[159] Whitmore L, Mackay RI, Van Herk M, Jones J, Jones R. Focused VHEE (very high energy electron) beams and dose delivery for radiotherapy applications. Scientific Reports. 2021;11(1):14013.

[160] Kokurewicz K, Brunetti E, Curcio A, Gamba D, Garolfi L, Gilardi A, et al. An experimental study of focused very high energy electron beams for radiotherapy. Communications Physics. 2021;4(1):33.

[161] Kokurewicz K, Brunetti E, Welsh G, Wiggins S, Boyd M, Sorensen A, et al. Focused very high-energy electron beams as a novel radiotherapy modality for producing high-dose volumetric elements. Scientific Reports. 2019;9(1):10837.

[162] Whitmore L, Mackay R, van Herk M, Korysko P, Farabolini W, Malyzhenkov A, et al. CERN-based experiments and Monte-Carlo studies on focused dose delivery with very high energy electron (VHEE) beams for radiotherapy applications. Scientific Reports. 2024;14(1):11120.

[163] Harpen MD. Positronium: Review of symmetry, conserved quantities and decay for the radiological physicist. Medical Physics. 2004;31(1):57-61.

[164] Shibuya K, Saito H, Nishikido F, Takahashi M, Yamaya T. Oxygen sensing ability of positronium atom for tumor hypoxia imaging. Communications Physics. 2020;3(1):173.

[165] Takyu S, Nishikido F, Tashima H, Akamatsu G, Matsumoto Ki, Takahashi M, et al. Positronium lifetime measurement using a clinical PET system for tumor hypoxia identification. Nuclear Instruments and Methods in Physics Research Section A: Accelerators, Spectrometers, Detectors and Associated Equipment. 2024;1065:169514.

[166] McKeown SR. Defining normoxia, physoxia and hypoxia in tumours—implications for treatment response. The British journal of radiology. 2014;87(1035):20130676.

[167] Moskal P, Baran J, Bass S, Choiński J, Chug N, Curceanu C, et al. Positronium image of the human brain in vivo. Science Advances. 2024;10(37):eadp2840.

[168] Azuelos G, Kitching J, Ramavataram K. Half-lives and branching ratios of some t= 1 2 nuclei. Physical Review C. 1977;15(5):1847.

[169] Kelley J, Kwan E, Purcell J, Sheu C, Weller H. Energy levels of light nuclei A= 11. Nuclear Physics A. 2012;880:88-195.

[170] Adrian G, Konradsson E, Lempart M, Bäck S, Ceberg C, Petersson K. The FLASH effect depends on oxygen concentration. The British journal of radiology. 2020;93(1106):20190702.

[171] Favaudon V, Labarbe R, Limoli CL. Model studies of the role of oxygen in the FLASH effect. Medical physics. 2022;49(3):2068-81.